SLAC-PUB-900
May 1971
(TH) and (EXP)

VAN HOVE ANALYSIS OF THE REACTIONS

$$\pi^- p \to \pi^- \pi^- \pi^+ p$$

and

$$\pi^+ p \to \pi^+ \pi^+ \pi^- p \text{ at 16 GeV/c.}*$$

J. Ballam, G. B. Chadwick, Z. G. T. Guiragossián,†
W. B. Johnson, D. W. G. S. Leith and K. Moriyasu

Stanford Linear Accelerator Center
Stanford University; Stanford, California 94305

(Submitted to Phys. Rev.)

*Work supported by the U. S. Atomic Energy Commission.

†Present Address: High Energy Physics Laboratory, Stanford University, Stanford, Calif.

ABSTRACT

Data from the reactions $\pi^- p \rightarrow \pi^- \pi^- \pi^+ p$ and $\pi^+ p \rightarrow \pi^+ \pi^+ \pi^- p$ have been obtained at 16 GeV/c in approximately equal samples from the BNL 80-inch hydrogen bubble chamber. We have studied both reactions for resonance production and compared our results with predictions of the one-pion-exchange model (OPEM) calculated by Wolf.

The four-body longitudinal phase space (LPS) plot suggested by Van Hove was used to analyze the data from both reactions. The events were separated according to distinct regions of the LPS plot in order to study the following classes of quasi-two-body final states: (1) diffractively produced three pion states, (2) diffractively produced $\pi\pi p$ states, (3) double resonance production such as $\rho^0 \Delta^{++}$, (4) single resonance production such as $\pi^- \pi^- \Delta^{++}$. The Van Hove analysis provided a much cleaner separation of resonances from background effects than the usual techniques. We observe production of the A_1 and A_2 mesons as well as the N*(1470) and N*(1700) isobars in the $\pi^+ \pi^- p$ system for both reactions. There is strong formation of the doubly-resonant states $\rho^0 \Delta^{++}$ and $f^0 \Delta^{++}$ and the general features of the non-diffractive events are all in good agreement with one-pion exchange.

Detailed comparisons between the data and the OPEM in each LPS plot region show that Van Hove analysis provides a sensitive test for the OPE model.

INTRODUCTION

The data presented here are derived from two experiments performed in the Brookhaven National Laboratory 80-inch HBC. In the first of these experiments the r.f. separated beam[1] was used in an unseparated mode to bring a beam of 16 GeV/c negative pions into the bubble chamber for an exposure of 60,000 photographs. This particular unseparated mode allowed quite good momentum resolution of $\sim\pm 0.3\%$. The contamination of K^- and $\bar{p}$ in the beam is estimated to be less than 1%. Comparison of the total $\pi^- p$ cross section measured in the bubble chamber with cross sections from counter experiments[2] indicate that the muon contamination is less than 5%.

In the second experiment a 16 GeV/c π^+ beam was brought into the bubble chamber using the r.f. beam in the separating mode for an exposure of 50,000 pictures. The momentum resolution of the resulting beam is $\sim\pm 1\%$. Careful monitoring of the beam during the exposure assured a clean separation of pions from protons, a fact which was later corroborated by comparing the total $\pi^+ p$ cross section measured in the chamber with values obtained from counter experiments. Assuming no muons in the beam we find the proton contamination to be less than 2% with 90% confidence from such a comparison.

The scanning and measuring of both experiments were accomplished using almost identical procedures, equipment, and personnel. All topologies were recorded in the scan and subsequently all four-prong events were measured. These measurements were reconstructed in space using TVGP and attempts at kinematical fitting were done using SQUAW. All successful fits were then checked for ionization consistency. The resulting samples of data contain 1995 events constraining to

$$\pi^- p \rightarrow p\pi^+\pi^-\pi^- \quad (1)$$

and 2050 events to

$$\pi^+ p \rightarrow p\pi^-\pi^+\pi^+ . \quad (2)$$

A few thousand frames of each exposure were triple scanned in a very carefully defined fiducial volume and beam particles passing through this volume were counted. The resulting topological cross sections (normalized to the data of reference 2 are listed in Table I. From an estimate of the fraction of the four-prong topology which constrains to reactions (1) and (2) we obtain reaction cross sections:

$$\sigma(\pi^- p \rightarrow p\pi^+\pi^-\pi^-) = 1.08 \pm 0.15 \text{ mb}$$

$$\sigma(\pi^+ p \rightarrow p\pi^-\pi^+\pi^+) = 1.32 \pm 0.15 \text{ mb.}$$

Figure 1 shows these reaction cross sections for data at other momenta.[3,4] The smooth curve indicates the OPE contribution as calculated by Wolf.[5]

In this calculation the vertex functions use the Benecke-Durr parametrization which has one free parameter, the radius R, for each vertex. Of the 19 radial parameters used in the calculation only 3 were inferred using the 16 GeV/c $\pi^- p$ data along with other data at 4 and 11 GeV/c. The predictions of this model, shown in every subsequent figure, are therefore not a fit to these data. The calculation gives an absolute cross section which we have compared with the data using our millibarn equivalent.

For the $\pi^- p$ data, the gentle decrease in cross section with increasing momentum above 8 GeV/c is in good agreement with the OPE contribution--a surprising result, as Wolf notes, since one might expect vector meson exchange to contribute strongly at high momentum. In the $\pi^+ p$ case, the cross section falls more rapidly above 8 GeV/c. At 16 GeV/c the OPE contribution accounts for more than 90% of the observed cross sections for both reactions. In later

sections we shall see that agreement between these data and the OPE contribution explains the details of these final states to a remarkable degree.

As noted in studies at other momenta,[3, 4] these four-body final states are dominated by quasi-two-body and three-body production. A measure of this dominance is the fact that about 90% of the events (90% for $\pi^+ p$, 89% for the $\pi^- p$ case) have at least one mass combination within $\pm \Gamma$, the resonance width, of the ρ^0, f^0, Δ^{++}, Δ^0 or A_2^+ region (defined here as $1.0 \leq m\,(3\pi) \leq 1.4$ GeV). At 16 GeV/c these quasi-two- and three-body processes have highly peripheral characteristics: in the overall barycentric frame, a resonant set of particles is produced sharply forward or backward with respect to the incident beam. Van Hove [6] has suggested a simple method, exploiting this fact, for separating these processes from one another. We will use this method in Section II to present a detailed analysis. Section I surveys the salient features of the data with more conventional methods and compares them with the OPE contribution.

I. COMPARISON OF THE DATA WITH OPE CONTRIBUTION

In this section we will examine the two and three particle mass spectra in an order which roughly parallels the Van Hove analysis of the next section.

A. Three Pion Spectra

In Figures 2a and b we see the three-pion spectra for reactions (1) and (2) respectively. These uncut data clearly show a strong enhancement between 1.0 and 1.4 GeV, long known in the literature as the A-meson region.[7] In the $\pi^- p$ data of Figure 2a and less so in the $\pi^+ p$ data of Figure 2b there is a suggestion that two resonant peaks occur, an A_1 state at a mass of ~1100 MeV and an A_2 state at a mass of ~1300 MeV.

In Figures 3a and b the same spectra are shown for those events having at least one $\pi^+\pi^-$ combination in the ρ region and excluding data where any πp combination is in the $\Delta(1236)$:

$$0.66 \leq m(\pi^+\pi^-) \leq 0.90 \text{ GeV}$$

and

$$m(p\pi^+) > 1.36 \text{ GeV}.$$

Cutting the data in this fashion tends to remove events preferentially at high masses, thus emphasizing the "A region" enhancements. At these high momenta the $\Delta(1236)$ is well separated from the A meson region and is excluded here more for historical reasons than necessity.

Although the π^+p data appear less well resolved, it is interesting to note that the cross sections for events in the A region ($m(\pi\pi\pi) < 1.4$ GeV) compare extremely well. In the uncut spectra the cross sections are 350 ± 50 μb and 350 ± 45 μb respectively for π^-p and π^+p. In the cut spectra (., noΔ) the values are 270 ± 40 and 255 ± 35 respectively.

Figure 4 shows the three pion spectra for events haveing a $\pi^+\pi^-$ invariant mass associated with the f^o ($1.1 \leq m(\pi^+\pi^-) \leq 1.4$ GeV). Once again events with a πp combination in the Δ have been excluded. A broad enhancement occurs near the A_3 region. Whereas the OPE contributions in Figure 3 fall well below the data in the region 1.0 GeV to 1.4 GeV, the OPE curve follows the data rather well in Figure 4 for the full range of mass values. Within the limited statistics, these data show no convincing evidence of a πf^o resonant state and agree rather well with OPE prediction.

B. Spectra for $p\pi^+\pi^-$

Mass plots of the $p\pi^+\pi^-$ system are shown in Figures 5a and b. Both

spectra show a large accumulation of data at high mass values which demonstrates the peripheral nature of these final states and comes about when fast pions from the upper vertex (see Fig. 11c) are combined with a low momentum proton from the lower vertex. The OPE contribution agrees rather well with this high mass peaking, whereas at low masses it falls below the data. In the low mass spectra there appear to be two peaks at mass values of $\sim$1.45 and 1.72 GeV respectively. Such enhancements have been noted in several experiments[9] though there seems to be some disagreement concerning their decay properties and their association with known πp resonances. In the following section we will indicate a preference of these data for $\Delta\pi$ decay modes.

The cross sections for low mass states (< 1.9 GeV) agree within statistics for our two experiments: 180 ± 25 μb for $\pi^- p$ and 220 ± 30 for $\pi^+ p$. The peaks appear narrower and more distinct in the $\pi^+ p$ data; however, this difference between the two samples is easily attributable to poor statistics.

In Figure 6 we see these same spectra after imposing a momentum transfer cut $t(p, p\pi^+\pi^-) < 0.25$ $(GeV/c)^2$. Most of the data at low masses survive this cut while the high mass accumulation is greatly reduced. This change of scale displays the 1.45 and 1.72 peaks in a more prominent way and gives credence to the peripheral formation of these states.

With the exception of these two peaks, the OPE contribution represents these spectra quite well.

C. The $\pi^+\pi^-$ System

Figures 7a and b show mass spectra for the $\pi^+\pi^-$ system. The ρ^0 and f^0 signals are quite strong and there is a shoulder near 1.68 GeV suggestive of the g^0. The OPE curve falls somewhat below the data in the ρ^0 region and for

masses below the ρ^0. This, of course, is a reflection of the strong A-meson enhancement in these data: "A" decay directly feeds the ρ^0 signal and the kinematics of A decay forces the other $\pi^+\pi^-$ combination to be at masses below or near the ρ^0 mass.

In contrast to this situation, the f^0 signal falls a little below the OPE estimate in the π^-p data and directly on the OPE curve for π^+p. This is consistent with the earlier observation that the πf^0 enhancements in these data have a "Deck-like" appearance and were well explained by OPE.

Figure 8 shows the spectra recoiling against $\Delta^0(1236)$ in the π^-p experiment and $\Delta^{++}(1236)$ in the π^+p case. In the first instance there are weak ρ^0 and f^0 signals which agree roughly with the OPE prediction though the data are systematically higher. In the π^+p data there are, of course, very strong $\Delta^{++}\rho^0$ and $\Delta^{++}f^0$ signals which agree remarkably well with the OPE prediction. In addition, there appears to be a discernable amount of $\Delta^{++}g^0$ production which exceeds the OPE estimate by roughly a factor of two.

D. The $p\pi^+_-$ Systems

Figures 9a and b give the mass distributions of $p\pi^+$ for reactions (1) and (2). The data show a very strong $\Delta^{++}(1236)$ signal and in general agree rather well with the OPE contribution except in the region of the $\Delta(1920)$ which appears, if at all, very weakly in these data. However, the low mass $p\pi\pi$ structure, noted earlier, will populate the Δ^{++} region of the mass spectrum due to kinematical constraints, in addition to the possible $\Delta\pi$ decay mode of these objects. Therefore, one expects a slight abundance of Δ^{++} over the OPE prediction. This appears to be the case for reaction (2) but to a lesser extent for the π^-p data, reaction (1).

The $p\pi^-$ spectra, depicted in Figures 10a and b, agree rather poorly with the OPE prediction. As Wolf has noted, this is not surprising considering the complexity of I = 1/2 resonances. One notes, as usual, a fair agreement at high masses where these complexities are lacking and fair agreement around the N*(1688). The worst disagreement occurs for the Δ^0(1236). Some of this can be attributed to the $p\pi^+\pi^-$ enhancements, in particular the one near 1.45 GeV where all $p\pi^-$ masses are kinematically restricted to the Δ(1236) region. These kinematical effects tend to broaden the Δ^0 peak as observed in the data especially for reaction (2).

In conclusion, one finds good agreement between the OPE contribution and these data in most of their general mass spectra. Differences, whey they occur, can usually be attributed to direct resonance production not included in the OPE calculation or to their reflections in other spectra.

II. VAN HOVE ANALYSIS

In order to study the production details of the various resonant states in reactions (1) and (2), we have used a technique suggested by Van Hove[6] and analyzed our data in terms of the center-of-mass (c.m.) longitudinal mementa of the final state particles. As Van Hove points out, the transverse momenta of all outgoing particles are experimentally known to be limited to small values (~ 200-400 MeV/c) so that the particles can be essentially characterized by their direction of motion, either forward or backward, in the center of mass. When a group of particles form a low mass resonance, they must be moving in the same c.m. direction with small relative momenta. This implies that resonance production can also be characterized by the c.m. direction alone of the resonating particles and thus suggests a simple technique for separating the

experimental data into contributions from distinct resonant final states. More precisely, the smallness of the transverse momenta constrains both the invariant mass and four-momentum transfer of a system of particles to simultaneously reach their minimum values only in the region of the longitudinal phase space (LPS) where all particles of the system are moving in the same c.m. direction.

The properties of the four-particle LPS have been discussed in detail by Van Hove and others[10, 11]. For our analysis, we use only the physical longitudinal momenta to separate the data from reactions (1) and (2) into distinct LPS regions which are defined by taking one, two, or three of the final state particles moving forward in the c.m. with the remaining particles moving backward. Geometrically, this is equivalent to selecting the events according to one of the faces of the cuboctahedron (Fig. 11a) which defines the boundary of the four-particle LPS. This can also be illustrated by projecting the LPS onto a two-dimensional plot, shown in Figure 11b, where the coordinates θ, ϕ are the polar and azimuthal angles related to the (x, y, z) axes defined in Figure 11a. The LPS regions are then the numbered areas in the θ-ϕ plot which can be associated with the square and triangular faces of the cuboctahedron. The boundary curves between each LPS region correspond to vanishing longitudinal momentum for one of the outgoing particles so that, on one side of the boundary, the particle is moving forward in the c.m., while on the other side it is moving backward.

We can associate a quasi-two-body reaction with each LPS region as shown in Figure 11c where the particles from the upper vertex are considered as moving forward in the c.m. and the particles from the lower vertex as moving backward. These exchange diagrams are motivated by our comparisons with the OPE model in the previous section. The diagrams for regions 3 and 4 are

the two OPE diagrams calculated by Wolf. The remaining diagrams represent production of three-particle states.

Each of the two- or three-body resonances discussed in the previous section can be associated with one or more of the LPS regions. The diffractively-produced resonances such as the $A_1(1080)$ meson and N*(1470) isobar are expected to occur in regions 1 and 2, respectively, with very small momentum transfer. The final states $\rho^o\Delta$ and $f^o\Delta$ should appear in region 3 and only πp isobar production is expected in region 4. Region 5, which would require some form of "double charge-exchange", should be empty. We note that N* production can also occur in region 2 as a subsystem of the $\pi^+\pi^-p$ state just as the ρ^o appears with the A_1 meson in region 1. Production of ρ^o or f^o is also allowed in region 2, but as we shall see later, they are suppressed by kinematics.

Before presenting the detailed features of each LPS region, we consider the inherent limitations of the selection procedure. It is clear that complete separation of reactions into different regions can only be accomplished at infinitely high energy. At any finite energy, there is some upper limit on the mass of a resonant system that will determine if the resonance will be assigned to the correct region. An estimate of the mass range "acceptance" of each region can be obtained by calculating the invariant mass and associated four-momentum transfer of various two- and three-particle systems on the boundary of the LPS plot. The details of the calculation are given in references (6) and (11) so we will only show the results here. For fixed values of the transverse momenta, $|P_T(\pi)| = 0.4$ GeV/c and $|P_T(p)| = 0.3$ GeV/c, Figure 12 shows the most relevant masses and four-momentum transfers for a polar-angle θ value of 2 radians which passes through LPS regions 2, 3, 4 and 5. Only one

of the two possible mass combinations is given in each case. We see that the mass and momentum transfer of the $p\pi^+\pi^-$ system exhibit pronounced minima in region 2 as expected, and that the upper limit on the mass acceptance is approximately 2 GeV, which is sufficient for the N* isobars at 1470 MeV and 1700 MeV. Similarly, the $\pi^+\pi^-$ mass limit is about 1.4 GeV at the region 3 boundary (ϕ = 5 radians), which will pass the ρ^o meson but may affect the f^o and higher mass resonances. These limitations are essentially determined by the incident beam energy and the kinematics so that the usefulness of the LPS selection clearly will depend on the particular application.

We have seen in the previous section that the OPE model provides a good description of the general features of reactions (1) and (2). In the following discussion we shall compare the OPE predictions with the experimental data in each LPS region and show that this provides a more sensitive test of the theoretical model. We first compare the OPE model with the longitudinal and transverse momenta of the outgoing particles in Figures 13 and 14. We see that the data are very well described by the theoretical curves in all cases. It is particularly interesting that the OPE model naturally predicts almost identical distributions of the transverse momentum for all particles. The correlations between the individual longitudinal momenta can also be studied by using the $\theta - \phi$ projection of the LPS. Figures 15 and 16 show the $\theta - \phi$ plots for reactions (1) and (2), respectively, along with the separate projections on the θ and ϕ axes. The plots can be easily interpreted by referring to the previous exchange diagrams in Figure 11c associated with the appropriate LPS regions in Figure 11b. The boundary curves are defined so that a pion is moving forward (backward) in the c.m. if the event is plotted above (below) the corresponding curve. For example, an event in region 1 is above all of the boundary

curves; thus all three pions are moving forward in the c.m. as would be expected for an A_1 or A_2 resonance. The strong peaking in the plot at the points where the boundary curves intersect results from the non-uniformity of the phase space in the $\theta - \phi$ variables[6] and from the very peripheral behavior of the data as seen in the θ projection. We see that the OPE curves agree very well with the θ and ϕ projections of the plot. Also, the almost complete absence of events in region 5 is in agreement with our association of an LPS region with a particular exchange diagram. Further detailed comparisons could be made between the OPE model and the LPS variables; however, we will defer these to a later section when we discuss each of the LPS regions separately.

In Table II we compare the experimental cross sections for the events in each LPS region with the corresponding absolute OPE predictions for our two reactions. In regions 3 and 4, which we expect to be dominated by one-pion exchange, the agreement is good except in region 4 of the $\pi^- p$ data where the OPE value is too high. In regions 1 and 2 we observe that the experimental cross sections are all systematically greater than the OPE values. This can be attributed to the presence of the diffractively-produced three-particle resonances which can only occur in regions 1 and 2.

In the following sections we consider each of the LPS regions in turn and present the results of our analysis for the various final states.

A. Region 1

Region 1 consists of those events with all three pions moving forward in the c.m. system. The three-pion mass distributions for reactions (1) and (2), shown in Figures 17 and 18, indicate that nearly all of the high-mass events

have been removed by the LPS selection. The enhancement in the A-meson region (1.0-1.4 GeV) is essentially unchanged and contains all of the A_1 and A_2 meson signals observed in the uncut data. A large broad background still persists in the A-meson region after the data selection, but it is very well described by the OPE contribution. This background is just the well-known "Deck effect" as shown in Figure 19a which is contained implicitly in the OPE model. We note here that unlike the usual Deck effect calculations which attempt to explain only the A- meson enhancement, the OPE background in region 1 is a necessary part of the one-pion exchange process which attempts to describe everything except the three-particle resonances.

The LPS selection of region 1 events also removes all of the strong isobars in the $p\pi^+$, $p\pi^-$, and $p\pi^+\pi^-$ systems.

The $\pi^+\pi^-$ mass spectra are shown in Figure 20 where both mass combinations have been plotted for each event. The absolute OPE predictions describe the distributions very well except in the region of the ρ^0 where the theoretical curves are too low. This is consistent with the presence of the A_1 and A_2 mesons which are known to be $\pi\rho$ resonances.

In Figures 21 and 22 the differential cross sections for region 1 are shown for the total three-pion data and for the events with at least one ρ^0. We have used the variable $t' = |t-t_{min}|$ where t is the squared four-momentum transfer from the target to the recoil proton and t_{min} is the minimum kinematic value of t. We see that the OPE curve describes the data well for t' greater than 0.1 and has a slope of approximately 7 $(GeV/c)^{-2}$. At smaller values of t', there is an excess of events which is mostly associated with the A-meson region. This suggests that the slope for diffractive resonance production is different from that of the OPE or Deck-type background. We have measured the slope in

the A_1 region (1.0 - 1.16 Gev) and find the values 11.6 ± 1.1 $(GeV/c)^{-2}$ and 10.4 ± 1.3 $(GeV/c)^{-2}$ for reactions (1) and (2), respectively. Both values are consistent with $\pi^- p$ and $\pi^+ p$ elastic scattering data at 16 Gev/c. There are indications of similar effects in the A_1 region in $\pi^+ p$ data at 8 GeV/c[13] and in the Q(1300 MeV) region in $K^+ p$ data at 13 GeV/c[14].

To further study the above effect in the t' distribution, we have selected the data for t' less than and greater than 0.08 $(GeV/c)^2$. The corresponding three-pion mass spectra are shown in Figure 23 where we have combined the $\pi^- p$ and $\pi^+ p$ data to increase the statistics. We note the dramatic difference between the two t' regions. For $t' > 0.08$ $(GeV/c)^2$, we observe relatively narrow A_1 and A_2 peaks, but for $t' < 0.08$ $(GeV/c)^2$ there is only a single broad peak centered at the A_1 mass. A further difference in the data between high and low t' can be seen in the decay angular distributions. In Figure 24 we show the distribution of the ρ^0-decay helicity angle $\cos\beta$, where we have selected on the A_1 and A_2 mass regions and cut on t'. The variable $\cos\beta$ is the equivalent of a Dalitz plot projection and is independent of the production mechanism--and therefore independent of t'--for a pure resonant state. The data clearly show a difference between t' less than or greater than 0.08 $(GeV/c)^2$. The A_2 distribution shows the expected 2^+ behavior (i.e., $\sin^2\beta$) only for large t' while the low t' distribution is consistent with a dominant 1^+ ($\ell = 0$) state as indicated by the OPE curve. The A_1 region data for small t' show a significant backward peaking in $\cos\beta$ which was previously interpreted as an indication of a d-wave contribution[7, 8, 15] to the 1^+ state. For large t', however, there is no backward peak and the distribution is more consistent with 1^+ s-wave.

One immediate conclusion can be drawn from the behavior of the A_2 distributions. It has been generally supposed that the A_2 is produced by exchange

of a vector meson despite the absence of a dip at $t' = 0$ expected of such an exchange. Aderholz et al[13] have suggested that the dip is obscured by the Deck effect background and we see that our data confirms this interpretation. Both the three-pion mass spectrum and the $\cos\beta$ distributions show the A_2 only for large t' while the small t' data are consistent with a Deck-type or OPE background. It is interesting to note that Ascoli et al[16] have also seen a dip at small t by using a general partial-wave technique to extract the 2^+ state from the data.

B. Region 2

Region 2 consists of all events with one pion of the same charge as the beam moving forward in the c.m. and all other particles going backward. Since there are two pions of the beam charge for each event, this provides an unambiguous selection criterion.

The $p\pi^+\pi^-$ mass distributions for reactions (1) and (2) are shown in Figures 25 and 26, respectively. The high-mass background events have been completely removed since only one of the two possible $p\pi^+\pi^-$ mass combinations is plotted for each event. Essentially all the N*(1470) and N*(1700) events are retained by the LPS selection. Again, there is a large broad background, similar to the three-pion case in region 1, which is well described by the OPE calculation. This can be easily understood by another Deck effect shown in Figure 19b where either a Δ^{++} or Δ^0 is formed and the exchanged pion scatters elastically at the upper vertex, producing a low mass enhancement in the $\pi\Delta$ mass distribution.

The $p\pi^+$, $p\pi^-$, and $\pi^+\pi^-$ mass spectra for region 2 are shown in Figures 27 and 28. The data are almost completely dominated by Δ^{++} production.

There is also some Δ^0 formation in the $p\pi^-$ system as well as a small enhancement in the 1400-1500 MeV region. The $\pi^+\pi^-$ distribution show an excess of events at low masses but there is no indication of either ρ^0 or f^0 formation. The OPE predictions agree with the general features of the two-body mass distributions but do not explain all of the observed Δ^{++} signal or any of the Δ^0 or other enhancements in the $p\pi^-$ and $\pi^+\pi^-$ spectra. Part of the difference between the data and the OPE model can be understood in terms of kinematical reflections from the N*(1470) and N*(1700) peaks. The Dalitz plot boundary for both the N*(1470) and the N*(1700) constrains the $\pi^+\pi^-$ mass toward low values and also causes the strong Δ^{++} to be reflected into the $p\pi^-$ mass distribution. For the N*(1700), this reflection is a relatively narrow peak in the 1400-1500 MeV region[17] which can account for the enhancement seen in the total region 2 data. We cannot, however, eliminate the possibility that there may be some real contribution from the 1470 MeV and 1520 MeV isobars in the $p\pi^-$ system.

The $p\pi^+\pi^-$ mass distributions are also shown in Figures 27 and 28 with the Δ^{++} and Δ^0 selected. The N*(1470) is unaffected by either cut but the N*(1700) appears to be almost entirely associated with the Δ^{++}. The behavior of the N*(1470) is caused in part by the strong overlap of the Δ bands which cover most of the $p\pi^+\pi^-$ Dalitz plot. Previous studies of the $p\pi^+\pi^-$ system[9] produced by π^+p, K^+p and pp interactions disagree on the existence of the $\Delta\pi$ decay mode of N*(1700). Our results for both reactions (1) and (2) are consistent with $\Delta^{++}\pi^-$ being the dominant decay mode. The decay ratio

$$R = \frac{\sigma(N^*(1700) \rightarrow \pi^-\Delta^{++})}{\sigma(N^*(1700) \rightarrow \pi^+\Delta^0)}$$

where only $\Delta^0 \rightarrow p\pi^-$ is seen, should be 9, 9/4, 1 for the isospin values I = 1/2, 3/2, 5/2. We conclude that I = 1/2 for the N*(1700) is in agreement with other experiments.

The t' differential cross sections for all region 2 events are shown in Figure 29. The OPE curves agree with the general shape of the experimental distributions but are systematically lower than the data points for all values of t'.

The production cross sections for the N*(1470) and N*(1700) were determined by fitting the $p\pi^+\pi^-$ mass spectrum with Breit-Wigner resonances plus the OPE background. Results from the π^-p and π^+p data were found to be consistent with each other so we have used the combined data sample to obtain the best fit. The resonance parameters from the fit are

$$\sigma(1470) = 32\ \mu b$$

$$M = 1430 \pm 20\ \text{MeV}$$

$$\Gamma = 150 \pm 40\ \text{MeV}$$

and

$$\sigma(1720) = 52 \pm 10\ \mu b$$

$$M = 1730 \pm 20\ \text{MeV}$$

$$\Gamma = 120 \pm 50\ \text{MeV}.$$

No error is quoted for the N*(1470) cross section because it was found to be extremely sensitive to the exact shape of the background curve near threshold. The fit value could be in error by as much as 50%. The masses and widths for both resonances are in good agreement with the values obtained in other production experiments at various energies[18].

Previous experiments have suggested that both the N*(1470) and N*(1700)

are diffractively produced. A recent compilation of πp and Kp data[23] also indicates that the cross sections decrease very slowly with the incident beam momentum. As a qualitative test of the production mechanism, we have imposed the same t' selection as in the three-pion case. The resulting $p\pi^+\pi^-$ mass spectra for high and low t' are shown in Figure 30. We observe that the N*(1700) peak is present only in the high t' region while an N*(1470) signal can be seen for all t'. The differential cross sections for the N*(1470) and N*(1700) are presented in Figure 31. We note that the data points and the OPE curve in the N*(1470) region are essentially parallel with a slope of approximately 10 $(GeV/c)^{-2}$. The N*(1700) distribution, however, has a slope of only 5 $(GeV/c)^{-2}$ while the corresponding OPE model slope is 8 $(GeV/c)^{-2}$. The experimental values agree well with previous measurements of the $p\pi^+\pi^-$ state from πp, Kp and pp interactions. This behavior is very analogous to the A_1-A_2 situation in region 1 and suggests that N*(1700) production may proceed differently from that of the N*(1470)--possibly also by vector meson exchange.

Although we have assumed that the N*(1700) enhancement is a single resonance, formation experiments indicate the existence of at least four I = 1/2 isobars with masses near 1700 MeV. Since the widths and branching ratios are different it may be informative to compare the $p\pi^+\pi^-$ spectrum with the $n\pi^+$ mass distribution from the reaction[20]

$$\pi^- p \rightarrow \pi^-\pi^+ n$$

We have imposed the same t' cut at 0.08 GeV^2 and the resulting mass spectra are shown in Figure 32. For $|t'| < 0.08$ GeV^2 there is some indication of Δ^+ and a narrow N*(1470) peak above the OPE background. In the high t' data we see further Δ^+ formation and a large enhancement peaking at 1700 MeV. The

presence of the N*(1700) at only high t' values in both the $n\pi^+$ and $p\pi^+\pi^-$ states suggests that we may be observing one of the "non-diffractive" isobars with comparable $N\pi$ and $N\pi\pi$ decay modes such as the $D_{15}(1670)$. Further studies of other decay modes as well as the t and energy dependence are clearly needed to establish the identity of this enhancement.

C. Region 3

Region 3 consists of all events with two pions of opposite charge moving forward in the c.m. and the proton and remaining pion moving backward. We expect this region as well as region 4 to provide the best comparisons with the OPE model since the associated exchange diagrams are the same as those used in the theoretical calculation.

The $\pi^+\pi^-$, $p\pi^+$ and $p\pi^-$ mass distributions are shown in Figures 33 and 34 where only the unique LPS selected mass combination is plotted for each event. The ρ^o and f^o mesons are produced with very little background and the recoiling $p\pi^+$ and $p\pi^-$ systems are completely dominated by N* isobars. The $\pi^+\pi^-$ mass spectra for both reactions are well described by the OPE calculation although the theoretical curve appears slightly higher than the data in the ρ^o region for reaction (2). The agreement with the $p\pi^+$ distribution is also very good except for a small N*(1900) enhancement predicted by the model which is not evident in the data. The $p\pi^-$ mass spectrum in reaction (1) shows a clear Δ^o peak above a broad background that may contain several other isobars. The discrepancy between data and theory in this case is partly due to the difficulty of incorporating the many N* resonances in this region into the OPE calculation[5].

The distributions of the four-momentum transfer squared, t' between the $\pi^+\pi^-$ and recoiling $p\pi^+$ systems are shown in Figure 35 for reactions (1) and (2).

Both reactions exhibit a very steep slope for small t' as expected for one-pion exchange. The OPE curve, which agrees well with the data, actually differs very little from a pure pion propagator $\sim(t + \mu^2)^{-2}$ over most of the t range. For $t' < 0.1$ $(GeV/c)^2$, the value of the slope is approximately 20 $(GeV/c)^{-2}$ in good agreement with experiments at other energies[13].

A good test of the inherent limitations of the LPS selection technique is provided by region 3. As we showed earlier in Figure 12, the upper limit on the $\pi^+\pi^-$ mass acceptance may affect the f^o and higher mass resonances. If we compare the mass distribution in Figure 34 with that of Figure 8 which shows the $\pi^+\pi^-$ events recoiling against the Δ^{++} with no other cuts, we see that the LPS selection tends to remove some of the f^o and most of the g^o signal. This limitation is clearly not important in our comparisons with the OPE model since we expect the theoretical distributions to show the same behavior. However, it can affect the value of the cross section and other detailed features of high mass resonances.

The production cross sections for the reactions

$$\pi^+ p \rightarrow \rho^o \Delta^{++} \tag{3}$$

$$\pi^+ p \rightarrow f^o \Delta^{++} \tag{4}$$

were measured and, as expected, the value for reaction (3) is independent of the data selection while the $f^o\Delta^{++}$ cross section is slightly smaller for the LPS selected events. The cross sections were determined from the overlap of the Δ^{++} band with the ρ^o and f^o bands, and a correction was applied for the tails of the Breit-Wigner resonances. The background level was estimated by extrapolation from the nonresonant events outside the overlap region. The cross sections obtained in this way are $\sigma(\rho^o\Delta^{++}) = 124 \pm 20$ μb and $\sigma(f^o\Delta^{++}) = 66 \pm 13$ μb.

The value for reaction (4) was determined without the LPS selection; for comparison, the region 3 value was 51 ± 10 μb which is only slightly smaller.

We compare our results with those of previous experiments in Figure 36 which shows a compilation of the cross sections for reactions (3) and (4) as a function of the laboratory momentum p_{LAB} of the incident pion. The high energy data above 4-5 GeV/c are all compatible with the simple relation[19] $\sigma \sim (p_{LAB})^{-n}$ where n is equal to 1.4 for both reactions. The solid curves shown in Figure 36 are the absolute OPE cross section predictions. Both the ρ^o and f^o data are very well described over the entire energy range from just above threshold up to 20 GeV/c. We note several interesting differences between these two reactions and the reactions[20]

$$\pi^- p \rightarrow \rho^o n \tag{5}$$

$$\pi^- p \rightarrow f^o n \tag{6}$$

which are also believed to proceed by one-pion exchange and are similarly well described by the OPE model. The cross sections for reactions (5) and (6) behave like $\sigma \sim (p_{LAB})^{-2}$ which is more characteristic of a simple one-pion exchange process. In addition, the $\rho^o n$ and $f^o n$ cross sections are nearly equal at high energies while the cross section for $f^o \Delta^{++}$ is a factor of two smaller than that for $\rho^o \Delta^{++}$. Wolf has pointed out[21], however, that such effects can be caused almost entirely by kinematics. This can be seen by comparing the values of t_{min} for the two sets of reactions. The difference in the t_{min} values for reactions (5) and (6) is much smaller than for the Δ^{++} reactions (3) and (4). Since the $d\sigma/dt$ distributions are very steep at small t, this can explain the greater difference in the cross sections of reactions (3) and (4). In addition, t_{min} decreases with increasing energy as $t_{min} \sim (p_{LAB})^{-2}$ for reactions (5) and

(6) but only as $t_{min} \sim (p_{LAB})^{-1}$ for reactions (3) and (4) so that the t_{min} value for $f^o\Delta^{++}$ remains relatively large even at high energies. However, since t_{min} eventually goes to zero with increasing energy for all reactions, this suggests that the difference in the cross sections must also decrease. This effect is not evident in the data due to the large errors, but the OPE model predicts a slow convergence of the cross sections for reactions (3) and (4) at high energy. The much slower dependence of the cross sections on p_{LAB} is also explained by the OPE model as a kinematic effect related to the large widths of the resonances. The value of t_{min} changes over the Δ^{++} mass distribution and introduces extra factors of p_{LAB} through the $d\sigma/dt$ integration limits so that the resulting energy dependence is slower than $(p_{LAB})^{-2}$.

In Figure 37 we compare the OPE model predictions with the $\pi^+\pi^-$ and $p\pi^+$ decay angular distributions for reaction (2). The polar Jackson[22] angle θ and the Treiman-Yang azimuthal angle ϕ are shown for all the region 3 data and for the $\rho^o\Delta^{++}$ events. Here, ' is the angle between the incident $\pi^+(p)$ and the outgoing $\pi^+(p)$ in the $\pi^+\pi^-$ ($p\pi^+$) rest frame. In all cases, the Treiman-Yang angle is consistent with isotropy in good agreement with one-pion exchange. The $\cos\theta$ distributions for all the region 3 events show a small asymmetry which is accurately reproduced by the OPE curves. When the $\rho^o\Delta^{++}$ events are selected, the experimental and OPE distributions for the Δ^{++} are both symmetric and consistent with $1 + 3\cos^2\theta$ as expected for one-pion exchange. The ρ^o distribution shows a strong asymmetry indicating the presence of other partial waves interfering with the p-wave decay. The OPE model also predicts an asymmetry from I = 0 and 2 s-wave contributions[5] but it is clearly not sufficient to explain the effect in the data.

In Figure 38 we show the corresponding angular distributions for reaction

(1). The agreement with the OPE model predictions is again very good for both the Jackson and Treiman-Yang angles.

Several experiments[4g, 24, 25] have reported significant correlation effects between the decay angles of the ρ^o and the Δ^{++}. Since the presence of any correlations may indicate a deviation from one-pion exchange, we have also looked for similar effects in our data. In Figure 39a we show a scatter diagram of the Jackson angles for the ρ^o and Δ^{++}. Projections of the separate $\cos\theta$ distributions are also presented in Figures 39b, c, d and e with the absolute OPE model predictions. The projected angular distributions have been divided into polar ($|\cos\theta| > 0.5$) and equatorial ($|\cos\theta| \leq 0.5$) regions in order to study any changes across the scatter plot. We see that the Δ^{++} distribution for equatorial ρ^o decays (Fig. 39e) appears much flatter than for the polar events (Fig. 39d). In the ρ^o decay, the forward-backward asymmetry seems slightly stronger for the polar Δ^{++} region. The same effects have also been observed at other energies. The theoretical OPE curves indicate no significant differences between the polar and equatorial distributions. The correlation effects have been explained--at least partially--by the inclusion of final state absorption[25], and Wolf has suggested that both vertex functions and absorption may be necessary for a completely satisfactory description.

D. Region 4

In region 4 we require the two pions of like charge to be moving forward in the c.m. and the remaining pion and proton to be moving backward. We observe the same type of one-pion exchange behavior in this region as we did in region 3. The distributions of $|t'|$, taken between the $\pi^+\pi^+$ or $\pi^-\pi^-$ system and the recoiling $p\pi$ system, are shown in Figure 40 for reactions (1) and (2). We again

see the steep forward slope for both reactions in good agreement with the OPE model.

In Figures 41 and 42 we see that the $p\pi^+$ system is dominated by Δ^{++} production and there is indication of Δ^0 and possibly some higher mass isobars in the $p\pi^-$ mass distribution. The recoiling dipion mass spectra are similar in both reactions and show no significant features. The OPE curves agree with the data except for the absolute magnitude in reaction (1). The theoretical predictions are too large as we saw previously from the cross section values in Table II.

The cross section for Δ^{++} production in reaction (1) is approximately 110 μb, corresponding to nearly 80% of the region 4 data. This value, however, cannot be directly compared with previous measurements of the reaction

$$\pi^- p \rightarrow \Delta^{++} \pi^- \pi^- \qquad (7)$$

since the LPS selection separates the events with low or high dipion mass into regions 4 or 2, respectively. As we saw in our discussion of region 2, the high mass events contribute to the Deck effect background under the $p\pi^+\pi^-$ resonances. An upper limit for the cross section of reaction (7) can be obtained by subtracting the N*(1470) and N*(1700) resonances. The result, $\sim$260 μb, is consistent with the values of 275 $\pm$ 28 μb and 183 $\pm$ 23 μb measured at 13 and 20 GeV/c[3], respectively.

The Jackson and Treiman-Yang angular distributions for the $\pi\pi$ and recoiling $p\pi$ systems are shown in Figure 43 for reactions (1) and (2). The dipion distributions have been symmetrized by folding about $\cos\theta = 0$ and $\phi = \pi/2$ to take into account the identical pions. For both reactions, the dipion Jackson angle seems to show much less contribution from higher partial waves than is

indicated by the OPE calculation. The $p\pi^+$ Jackson angle also seems to show a greater asymmetry than the OPE curve. When the Δ^{++} events are selected in reaction (1), the distribution is still strongly asymmetric, in contrast to the $\rho^0\Delta^{++}$ events in region 3. The Treiman-Yang distributions are compatible with the OPE model, but it seems clear that other effects--such as absorption--may be necessary for a better description of the data.

Other studies of reaction (7) at different beam energies have also been reported, although with very different interpretations of the exchange mechanisms involved. Mott et al[26] compared their results at 6 GeV/c with a double-Regge-pole model and obtained a good description of their data using only pion and Pomeranchuk exchanges. In contrast, Bartsch et al[12] used the multiperipheral model of Chan, Loskiewics and Allison[27] to fit their data at 16 GeV/c and concluded that a large baryon exchange contribution was necessary in addition to the meson exchanges. Both models, however, start from essentially the same multiperipheral exchange diagrams and differ only in their treatment of the low invariant mass regions. The double-Regge model uses the same amplitude for all masses while the CLA model interpolates to a constant phase-space-like behavior at small invariant masses. We see from our LPS selection that almost two-thirds of the Δ^{++} events come from region 2 where the $\pi^-\Delta^{++}$ system is constrained toward low invariant mass values by a Deck-type mechanism. Both our data and the OPE model, however, show significant mass-dependent structure which is in strong disagreement with the CLA model approach. We also note that the simple double-Regge model and the OPE model are essentially equivalent in region 2, aside from detailed considerations of form-factors or Reggeization, which therefore explains the similarity of their predictions.

III. DISCUSSION

The preceding discussion demonstrates that our simple selection of events according to their longitudinal momenta provides a valuable technique for studying the distinct final state contributions in our data. We note that the LPS regions are particularly useful when making comparisons with a theory like the OPE model which describes the complete four-body state rather than just resonance production. The problems of background and kinematical reflections are also considerably simplified although it is clear that many of our results could have been obtained by the conventional methods of selecting separately on masses, momentum transfers, and so forth. As an example, the problem of having to plot two (or more) mass combinations for each event is often resolved by choosing the combination with the smallest momentum transfer; in fact, we see that the LPS selection is equivalent to this procedure. The advantage of using the LPS selection is clearly that it greatly simplifies the analysis by reducing the number of variables involved.

We conclude that the OPE calculation of Wolf provides a very good description of reactions (1) and (2) with the exception of the three-particle resonances which have not been incorporated in the model. The other minor differences between data and theory which we discussed are very likely due to the fact that the values of the OPE model parameters were initially determined from data at lower energies where the one-pion exchange contributions are more difficult to separate out. This would explain why the OPE predictions appear to agree much better with the "standard" experimental distributions in Section I, than they do with the individual LPS region distributions. Most of the differences we observe, however, could be resolved by relatively small adjustments in the OPE

parameters[5].

We would like to thank G. Wolf, F. Gilman and F. Winkelmann for several useful discussions.

REFERENCES

1. H. Foelsche and J. Sandweiss, "Operating Energies and Fluxes for the R.F. Separated Beam", BNL Report HF/JS-1 (Unpublished).

2. K. J. Foley, R. S. Jones, S. J. Lindenbaum, W. A. Love, S. Ozaki, E. D. Platner, C. A. Quarles and E. H. Willen, Phys. Rev. Letters 19, 330 (1967).

3. Data for $\pi^- p$

   a. 1.59 GeV/c: Saclay-Orsay-Bari-Bologna Collaboration, Nuovo Cimento 29, 515 (1963).

   b. 2.1 GeV/c: P. H. Satterblom, W. D. Walker, and A. R. Erwin, Phys. Rev. 134, B207 (1964).

   c. 2.75 GeV/c: Saclay-Orsay-Bari-Bologna Collaboration, Nuovo Cimento 35, 713 (1965).

   d. 4.0 GeV/c: Aachen-Birmingham-Bonn-Hamburg-London (I.C.)-München Collaboration, (1) Nuovo Cimento 31, 485 (1964), (2) Nuovo Cimento 31, 729 (1964).

   e. 8.05 GeV/c: J. W. Lamsa, N. M. Cason, N. N. Biswas, I. Derado, T. H. Graves, V. P. Kenney, J. A. Poirier, and W. D. Shepherd, Phys. Rev. 166, 1395 (1968).

   f. 11 GeV/c: Genova-Hamburg-Milano-Saclay Collaboration, Nuovo Cimento 47A, 675 (1967).

   g. 13 and 20 GeV/c: G. W. Brandenburg, A. E. Brenner, M. L. Ioffredo, W. H. Johnson, Jr., J. K. Kim, M. E. Law, J. E. Mueller, B. M. Salzberg, J. H. Scharenguivel, L. K. Sisterson, and

J. J. Szymanski, Nuclear Physics B16, 287 (1970).

4. Data for $\pi^+ p$

a. 1.95 GeV/c: F. E. James and H. L. Kraybill, Bull. Am. Phys. Soc. 8, 342 (1963) and Yale University Report, (1963) (Unpublished).

b. 3.7 GeV/c: B. C. Shen, Ph.D. Thesis, University of California, UCRL-16170 (Sept. 1965).

c. 4.0 GeV/c: Aachen-Berlin-Birmingham-Bonn-Hamburg-London (I.C.)-München Collaboration, Phys. Rev. 138, B897 (1965).

d. 5.0 GeV/c: Bonn-Durham-Nijmegen-Paris-Strasbourg-Turin Collaboration, Nuclear Physics B7, 681 (1968).

e. 7.0 GeV/c: P. Slattery, H. Kraybill, B. Forman and T. Ferbel, Nuovo Cimento 50, 377 (1967).

f. 8 GeV/c: Aachen-Berlin-CERN Collaboration, Physics Letters 12, 356 (1964).

g. 13 GeV/c: J. A. Gaidos, et al, to be published.

h. 18.5 GeV/c: N. N. Biswas, et al, Phys. Rev. D2, 2529 (1970).

5. G. Wolf, Phys. Rev. 182, 1538 (1969).

6. L. Van Hove, Nuclear Physics B9, 331 (1969).

7. J. Ballam, A. D. Brody, G. B. Chadwick, D. Fries, Z. G. T. Guiragossian, W. B. Johnson, R. R. Larsen, D. W. G. S. Leith, F. Martin, M. Perl, E. Pickup, and T. H. Tan, Phys. Rev. Letters 21, 934 (1968).

8. David J. Crennell, Uri Karshon, Kwan Wu Lai, J. Michael Scan and W. H. Sims, Phys. Rev. Letters 24, 781 (1970).

9. S. Miyashita, et al, Nuovo Cimento 66A, 606 (1970); V. E. Barnes, et al, Phys. Rev. Letters 23, 1516 (1969); R. B. Willmann, et al, Phys. Rev. Letters 24, 1260 (1970); G. W. Brandenburg, et al, Nuclear Physics B16, 287 (1970); J. G. Rushbrooke, Proceedings of the Fourteenth International Conference on High Energy Physics, Vienna, Austria, September 1968, p. 158.

10. A. P. Sheng, Ph.D. Thesis, M.I.T. (Unpublished) (February 1970).

11. K. Moriyasu, SLAC Group B Physics Note 42 (April 1970) (Unpublished).

12. J. Bartsch, et al, (Aachen-Berlin-Bonn-CERN-Heidelberg-London-Vienna Collaboration), Nuclear Physics B19, 381 (1970).

13. M. Aderholz, et al, (Aachen-Berlin-CERN Collaboration), Nuclear Physics B8, 45 (1968).

14. J. C. Berlinghieri, et al, Conf. on High Energy Collisions of Hadrons, CERN Report 68-7, Vol. 2 (1968) p. 172.

15. J. Ballam, et al, Phys. Rev. D1, 94 (1970).

16. G. Ascoli, et al, Phys. Rev. Letters 25, 962 (1970).

17. This effect was verified with the OPE model by selecting a $p\pi^+\pi^-$ mass band around 1700 MeV to simulate the effect of a resonance.

18. R. J. Plano, XVth Intl. Conf. on High Energy Physics, Kiev (1970).

19. D. R. O. Morrison, Phys. Letters 22, 528 (1966).

20. J. Ballam, et al, Phys. Letters 31B, 489 (1970).

21. G. Wolf, Phys. Rev. Letters 19, 925 (1967).

22. J. D. Jackson, Nuovo Cimento 34, 1644 (1964).

23. D. R. O. Morrison, XVth Intl. Conf. on High Energy Physics, Kiev (1970).

24. G. Goldhaber et al, Phys. Letters 18, 76 (1965).

25. F. Crijns, et al, (Aachen-Berlin-CERN Collaboration), Phys. Letters 22, 533 (1966).

26. J. E. Mott, H. J. Martin and K. F. Galloway, Nuclear Physics B16, 102 (1970).

27. Chan Hong-Mo, J. Loskiewics and W. W. M. Allison, Nuovo Cimento 57A, 93 (1968).

TABLE I

Class	$\sigma(\pi^- p)$ mb	$\sigma(\pi^+ p)$ mb
2 prongs	8.7 ± 0.6	7.6 ± 0.6
4 prongs	8.8 ± 0.7	8.6 ± 0.6
6 prongs	4.6 ± 0.6	4.5 ± 0.5
8 prongs	1.5 ± 0.3	1.1 ± 0.3
10 prongs	0.2 ± 0.1	0.1 ± 0.05
Visible V^o	1.6 ± 0.3	2.1 ± 0.3

Table II

	$\pi^- p$		$\pi^+ p$	
LPS Region	σ_{EXP} (μb)	σ_{OPE} (μb)	σ_{EXP} (μb)	σ_{OPE} (μb)
Total	1080 $\pm$ 120	980	1320 $\pm$ 150	1150
1	477 $\pm$ 53	415	506 $\pm$ 60	419
2	261 $\pm$ 29	176	275 $\pm$ 34	170
3	207 $\pm$ 23	202	430 $\pm$ 52	470
4	128 $\pm$ 23	181	77 $\pm$ 12	80
5	7 $\pm$ 1	6	32 $\pm$ 4	10

FIGURE CAPTIONS

1. Cross sections for $\pi^- p \to p\pi^+\pi^-\pi^-$ and $\pi^+ p \to p\pi^+\pi^+\pi^-$ as a function of incident laboratory momentum. The solid curves are from the OPE model calculation. The open circles indicate our data at 16 GeV/c.
2. Three-pion invariant mass distributions from reactions (1) and (2). The solid curves are the absolute OPE model predictions.
3. Three-pion mass spectra from reactions (1) and (2) with at least one $\pi^+\pi^-$ combination in the ρ^0 and no Δ^0 or Δ^{++}. The OPE model predictions are indicated by the solid curves.
4. Three-pion mass distributions from reactions (1) and (2) with at least one $\pi^+\pi^-$ combination in the f^0 and no Δ. The solid curves are the absolute OPE model predictions.
5. $p\pi^+\pi^-$ invariant mass distributions from reactions (1) and (2). Both combinations are plotted for each event. The solid curves are the absolute OPE model predictions.
6. $p\pi^+\pi^-$ mass distributions from reactions (1) and (2) with selection $t < 0.25$ $(\text{GeV/c})^2$. Both mass combinations are plotted per event. The OPE model predictions are given by the solid curves.
7. $\pi^+\pi^-$ invariant mass spectra for reactions (1) and (2). Both combinations are plotted for each event. The solid curves are the absolute OPE model predictions.
8. Invariant mass of the $\pi^+\pi^-$ system recoiling against the Δ^0 for reaction (1) and against the Δ^{++} for reaction (2). The solid curves are the absolute OPE model predictions.

9. $p\pi^+$ mass distributions from reactions (1) and (2). Both combinations are plotted for reaction (2). The solid curves show the OPE contribution.

10. $p\pi^-$ invariant mass distributions from reactions (1) and (2). Both mass combinations are plotted for reaction (1). The solid curves are the absolute OPE model predictions.

11. (a) Cuboctahedron which defines the boundary of the four-body longitudinal phase space. Numbers of square and triangular faces correspond to exchange diagrams in (c).

    (b) Projection of LPS in polar and azimuthal coordinates θ, ϕ.

    (c) Quasi-two body exchange diagrams associated with each LPS region. The listed resonances are those expected to be produced in each region.

12. Invariant mass and four-momentum transfer on the boundary of the LPS plot for the $p\pi^+\pi^-$, $p\pi^+$, $p\pi^-$ and $\pi^+\pi^-$ systems. The curves are calculated for a γ value of 2 radians and transverse momenta of 400 and 300 MeV/c for the pions and proton, respectively. Only one of the two possible mass combinations is shown in each case.

13. Longitudinal (P_L) and transverse (P_T) momenta in the overall c.m. frame for the outgoing particles from reaction (1). The solid curves are the absolute OPE model predictions.

14. Longitudinal (P_L) and transverse (P_T) momenta in the overall c.m. frame for the outgoing particles from reaction (2). The solid curves are the absolute OPE model predictions.

15. Scatter diagram of θ versus ϕ for reaction (1). The absolute OPE predictions are shown as solid curves on the θ and ϕ projections.

16. Scatter diagram of θ versus ϕ for reaction (2). The absolute OPE predictions are shown as solid curves on the θ and ϕ projections.

17. (a) $\pi^+\pi^-\pi^-$ invariant mass distribution in LPS region 1 for reaction (1).
    (b) same as (a) with at least one $\pi^+\pi^-$ combination in the ρ^0. The OPE model contributions are shown by the solid curves.
18. (a) $\pi^+\pi^+\pi^-$ invariant mass distribution in LPS region 1 for reaction (2).
    (b) same as (a) with at least one $\pi^+\pi^-$ combination in the ρ^0. The OPE model contributions are shown by the solid curves.
19. Deck effect exchange diagrams for the final states (a) $\rho\pi p$ and (b) $\pi\pi N^*$.
20. $\pi^+\pi^-$ mass spectra for region 1 from reactions (1) and (2). Both combinations are plotted for each event. The solid curves are the OPE model contributions.
21. (a) $d\sigma/d|t'|$ distribution for region 1 events from reaction 1.
    (b) same as (a) with at least one $\pi^+\pi^-$ combination in ρ^0. The solid curves are the absolute OPE contributions.
22. (a) $d\sigma/d't'$ distribution for region 1 events from reaction 2.
    (b) same as (a) with at least one $\pi^+\pi$ combination in ρ^0. The solid curves are the absolute OPE contributions.
23. Three-pion mass spectrum in region 1 for combined reaction (1) and (2) data. (a) $|t'| < 0.08$ $(GeV/c)^2$ (b) $|t'| > 0.08$ $(GeV/c)^2$. The absolute OPE contributions are shown by the solid curves.
24. Distribution of the ρ^0-decay helicity angle $\cos\beta$ for the combined data.
    (a) $|t'| < 0.08$ $(GeV/c)^2$ for the A_1 region (1.0 - 1.16 GeV)
    (b) $|t'| > 0.08$ $(GeV/c)^2$ for the A_1
    (c) $|t'| < 0.08$ $(GeV/c)^2$ for the A_2 region (1.2 - 1.36 GeV)
    (d) $|t'| > 0.08$ $(GeV/c)^2$ for the A_2.
    The solid curves show the OPE model contributions.
25. $p\pi^+\pi^-$ invariant mass distribution for reaction (1) in LPS region 2 (a) all events (b) $p\pi^+$ in the Δ^{++} (c) $p\pi^-$ in the Δ^0. The solid curves show the

absolute OPE model contributions.

26. $p\pi^+\pi^-$ invariant mass distribution for reaction (2) in region 2. (a) all events (b) $p\pi^+$ in the Δ^{++} (c) $p\pi^-$ in the Δ^0. The solid curves show the absolute OPE model contributions.

27. Two-body invariant mass distributions in region 2 from reaction (1). (a) $p\pi^+$ system (b) $p\pi^-$ system (c) $\pi^+\pi^-$ system. The solid curves are the OPE contributions.

28. Two-body invariant mass distributions in region 2 from reaction (2). (a) $p\pi^+$ system (b) $p\pi^-$ system (c) $\pi^+\pi^-$ system. The solid curves are the OPE contributions.

29. $d\sigma/d|t'|$ distribution of region 2 events from reactions (1) and (2). The OPE model contributions are shown by the solid curves.

30. $p\pi^+\pi^-$ invariant mass spectrum in region 2 for the combined data from reactions (1) and (2). (a) $|t'| < 0.08$ (GeV/c)^2 (b) $|t'| > 0.08$ (GeV/c)^2. The absolute OPE contributions are indicated by the solid curves.

31. $d\sigma/d|t'|$ distribution for combined data in region 2. (a) $p\pi^+\pi$ in N*(1470) region (1.35 - 1.55 GeV) (b) $p\pi^+\pi^-$ in N*(1700) region (1.62 - 1.82 GeV). The solid curves are the OPE model contributions.

32. $n\pi^+$ mass distributions for the reaction $\pi^-p \rightarrow \pi^-\pi^+n$ at 16 GeV/c. (a) $|t'| < 0.08$ (GeV/c)^2 (b) $|t'| > 0.08$ (GeV/c)^2. The OPE model contributions are indicated by the solid curves.

33. Invariant mass distributions of the $\pi^+\pi^-$ and recoiling $p\pi^-$ systems for reaction (1) in LPS region 3. The solid curves show the absolute OPE model predictions.

34. Invariant mass distributions of the $\pi^+\pi^-$ and recoiling $p\pi^+$ systems for reaction (2) in LPS region 3. The solid curves show the absolute OPE

model predictions.

35. Distributions of four-momentum transfer squared $|t'|$ between the $\pi^+\pi^-$ and recoiling $p\pi^+$ systems in region 3. The solid curves represent the absolute OPE model predictions.

36. Production cross sections for the reactions $\pi^+p \to \rho^o\Delta^{++}$ and $\pi^+p \to f^o\Delta^{++}$ as a function of incident laboratory momentum. The solid curves show the absolute OPE model calculations.

37. Jackson ($\cos\theta$) and Treiman-Yang (ϕ) decay angular distributions for all region 3 events and for the $\rho^o\Delta^{++}$ final state from reaction (2). The solid curves are the absolute OPE predictions.

38. Jackson ($\cos\theta$) and Treiman-Yang (ϕ) decay angular distributions for all region 3 events from reaction (1). The solid curves are the absolute OPE predictions.

39. (a) Scatter diagram of the ρ^o and Δ^{++} decay polar angles for reaction (2). (b)-(e) Distributions of $\cos\theta$ projections for polar ($|\cos\theta| > 0.5$) and equatorial ($|\cos\theta| \leq 0.5$) regions of recoiling system. The solid curves show the OPE model predictions.

40. Distributions of four-momentum transfer squared $|t'|$ between the $\pi^+\pi^+(\pi^-\pi^-)$ and recoiling $p\pi^-(p\pi^+)$ systems in region 4. The solid curves are the absolute OPE model predictions.

41. The $\pi^-\pi^-$ and recoiling $p\pi^+$ mass spectra for reaction (1) in region 4. The solid curves show the absolute OPE calculations.

42. The $\pi^+\pi^+$ and recoiling $p\pi^-$ mass spectra for reaction (2) in region 4. The solid curves show the absolute OPE calculations.

43. Jackson ($\cos\theta$) and Treiman-Yang (ϕ) decay angular distributions for all region 4 events from (a) reaction (1) and (b) reaction (2). The solid curves are the absolute OPE model predictions.

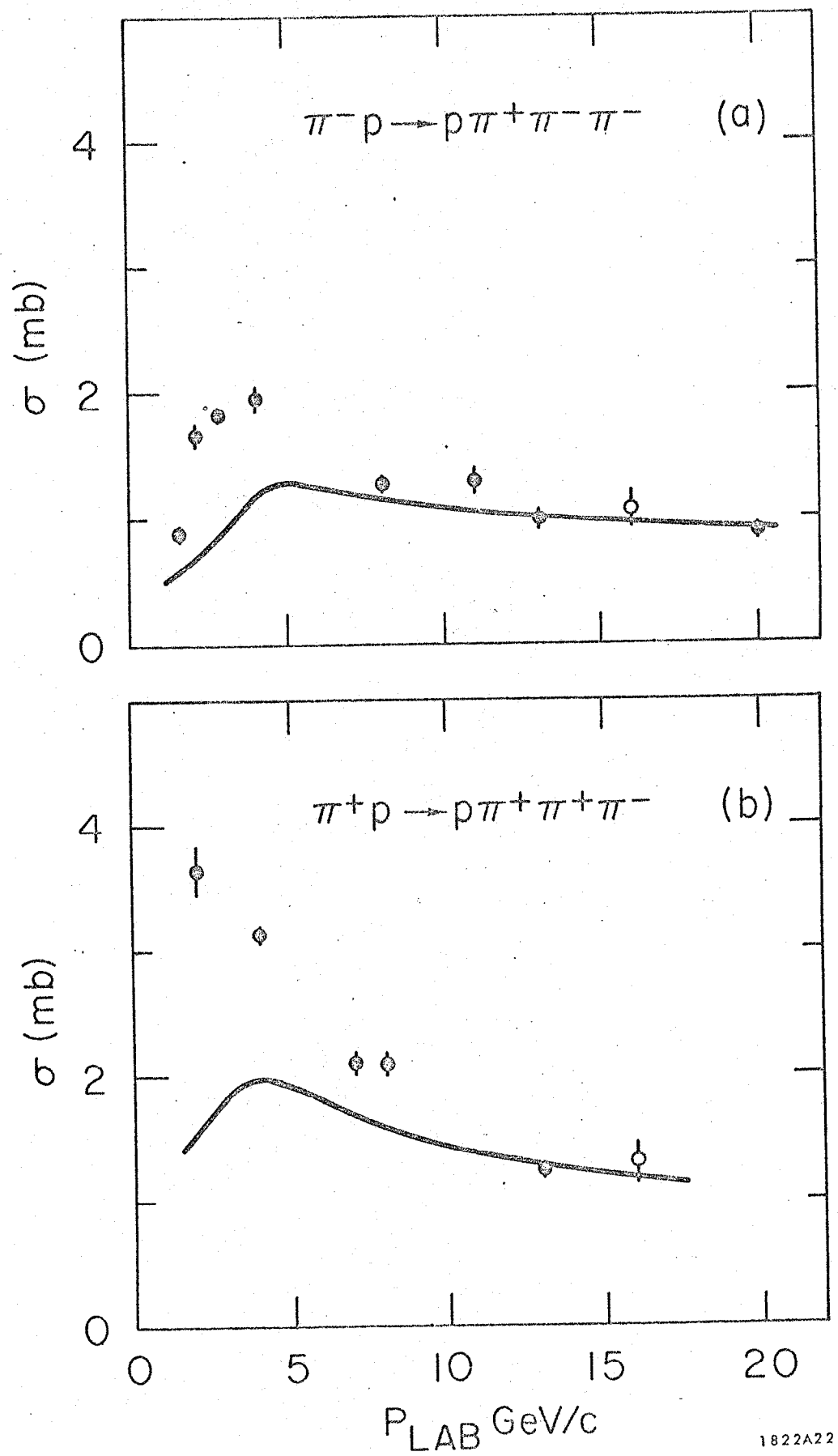
$\pi^- p \rightarrow p\pi^+\pi^-\pi^-$ (a)
$\pi^+ p \rightarrow p\pi^+\pi^+\pi^-$ (b)
σ (mb)
4
2
0
0
5
10
15
20
P_{LAB} GeV/c
1822A22

Fig. 1

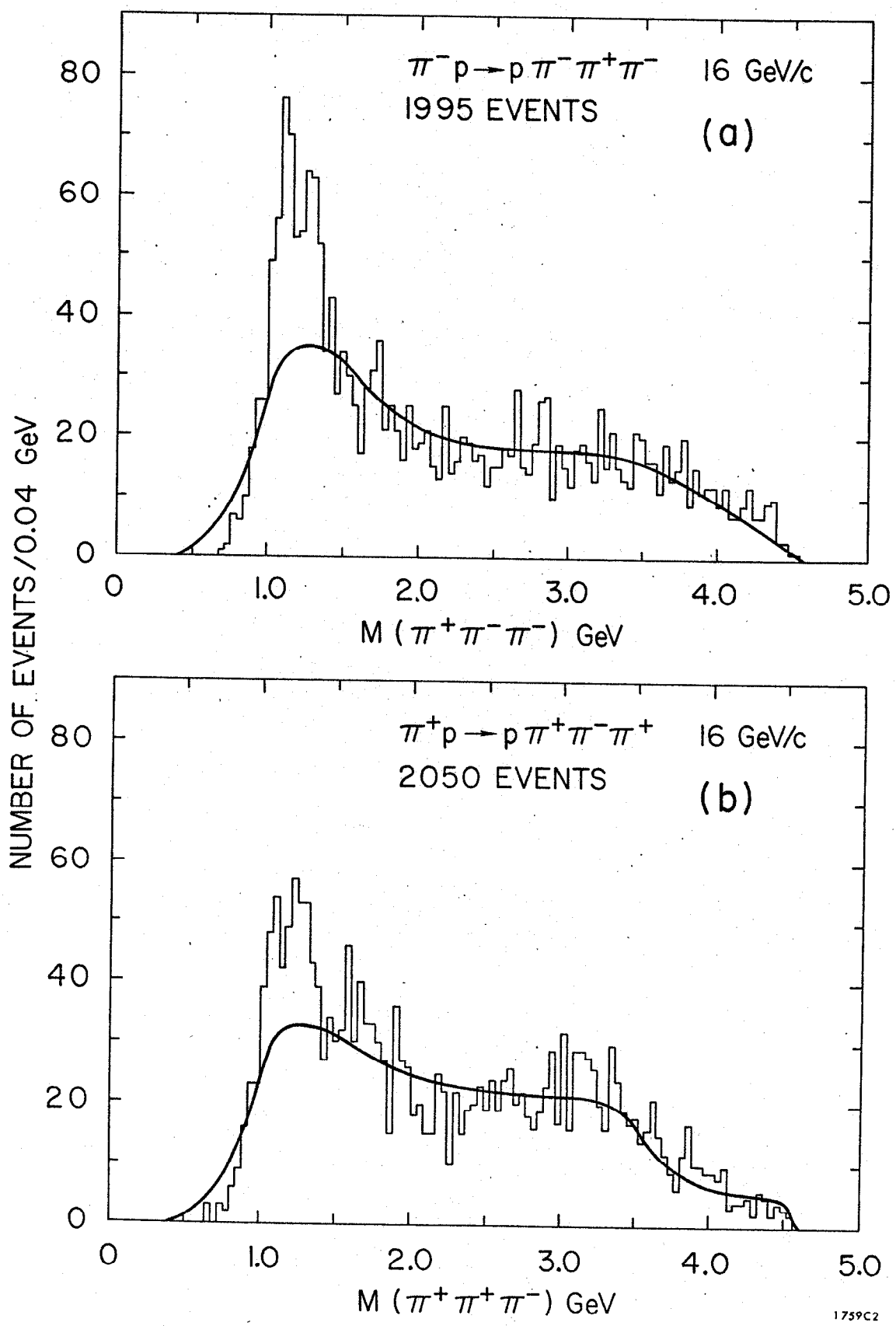
$\pi^- p \to p\,\pi^-\pi^+\pi^-$ 16 GeV/c
1995 EVENTS
(a)
$\pi^+ p \to p\,\pi^+\pi^-\pi^+$ 16 GeV/c
2050 EVENTS
(b)
NUMBER OF EVENTS/0.04 GeV
M ($\pi^+\pi^-\pi^-$) GeV
M ($\pi^+\pi^+\pi^-$) GeV
0
20
40
60
80
1.0
2.0
3.0
4.0
5.0
1759C2

Fig. 2

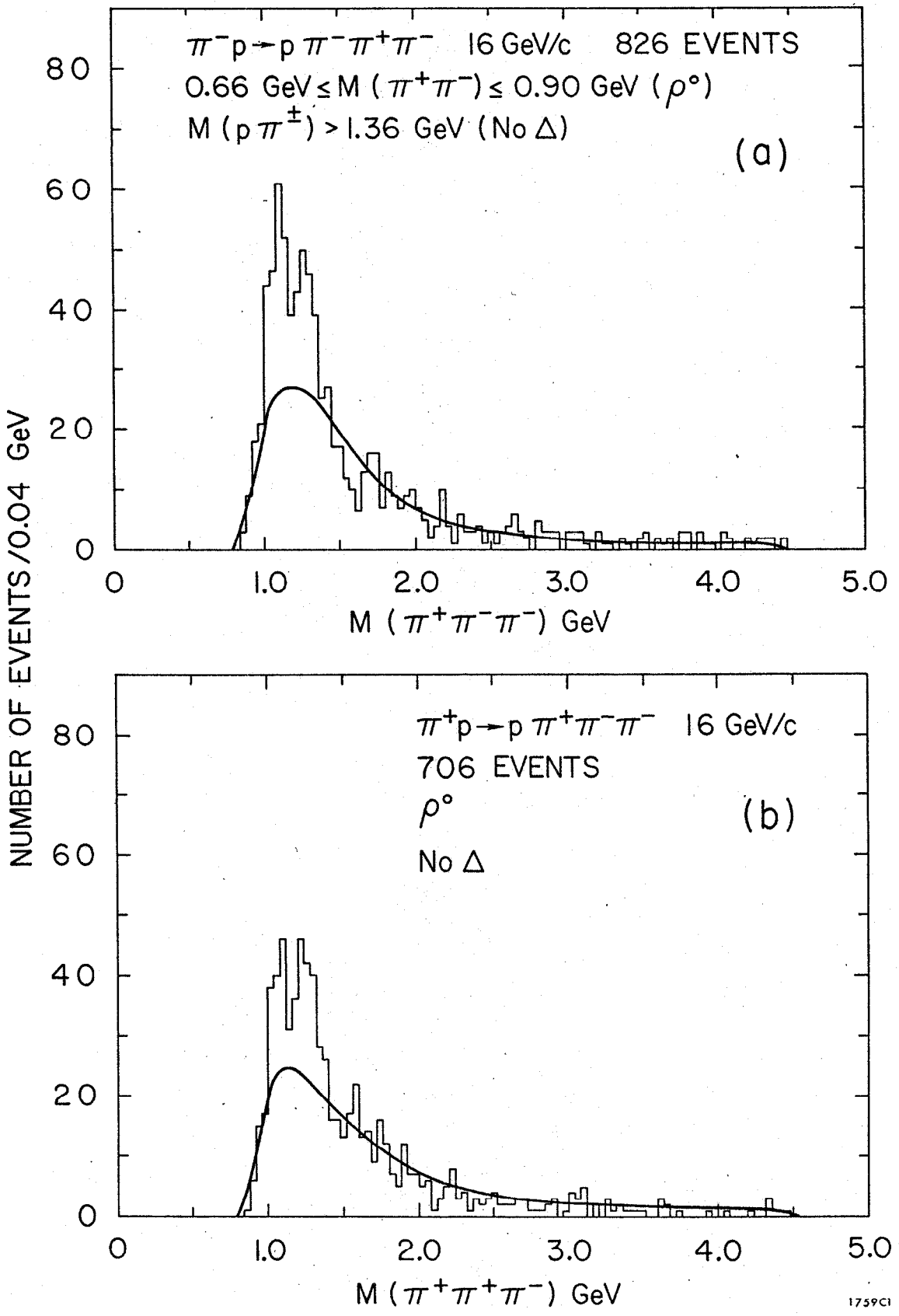
$\pi^- p \to p\,\pi^-\pi^+\pi^-$ 16 GeV/c 826 EVENTS
0.66 GeV ≤ M ($\pi^+\pi^-$) ≤ 0.90 GeV (ρ°)
M ($p\,\pi^\pm$) > 1.36 GeV (No Δ)
(a)
$\pi^+ p \to p\,\pi^+\pi^-\pi^-$ 16 GeV/c
706 EVENTS
ρ°
No Δ
(b)
NUMBER OF EVENTS/0.04 GeV
M ($\pi^+\pi^-\pi^-$) GeV
M ($\pi^+\pi^+\pi^-$) GeV
0
20
40
60
80
1.0
2.0
3.0
4.0
5.0
1759C1

Fig. 3

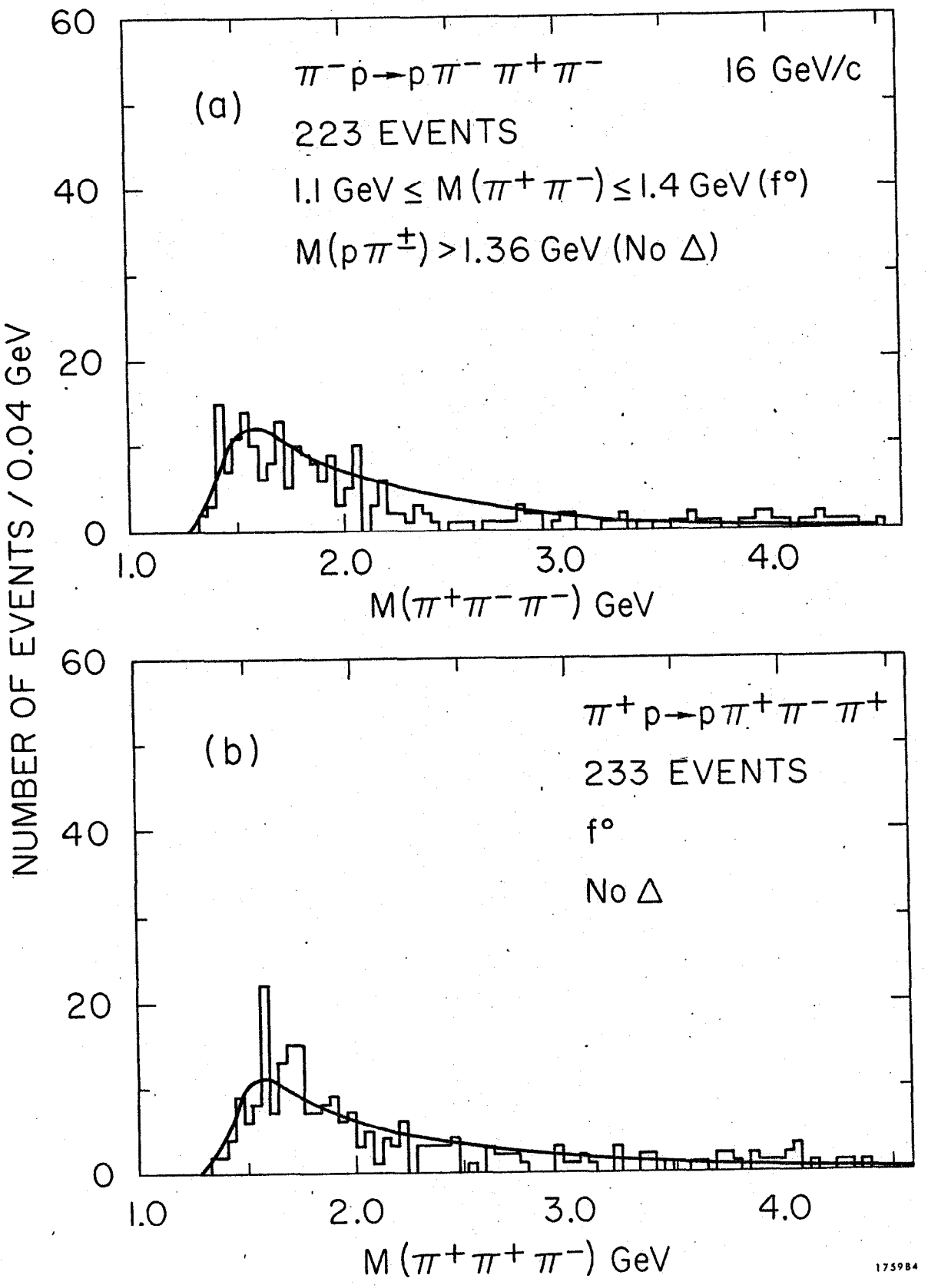
60
40
20
0
(a)
$\pi^- p \to p\pi^- \pi^+ \pi^-$
16 GeV/c
223 EVENTS
1.1 GeV ≤ M($\pi^+ \pi^-$) ≤ 1.4 GeV (f°)
M($p\pi^\pm$) > 1.36 GeV (No Δ)
1.0
2.0
3.0
4.0
M($\pi^+\pi^-\pi^-$) GeV
NUMBER OF EVENTS / 0.04 GeV
60
40
20
0
(b)
$\pi^+ p \to p\pi^+ \pi^- \pi^+$
233 EVENTS
f°
No Δ
1.0
2.0
3.0
4.0
M ($\pi^+\pi^+\pi^-$) GeV
175984

Fig. 4

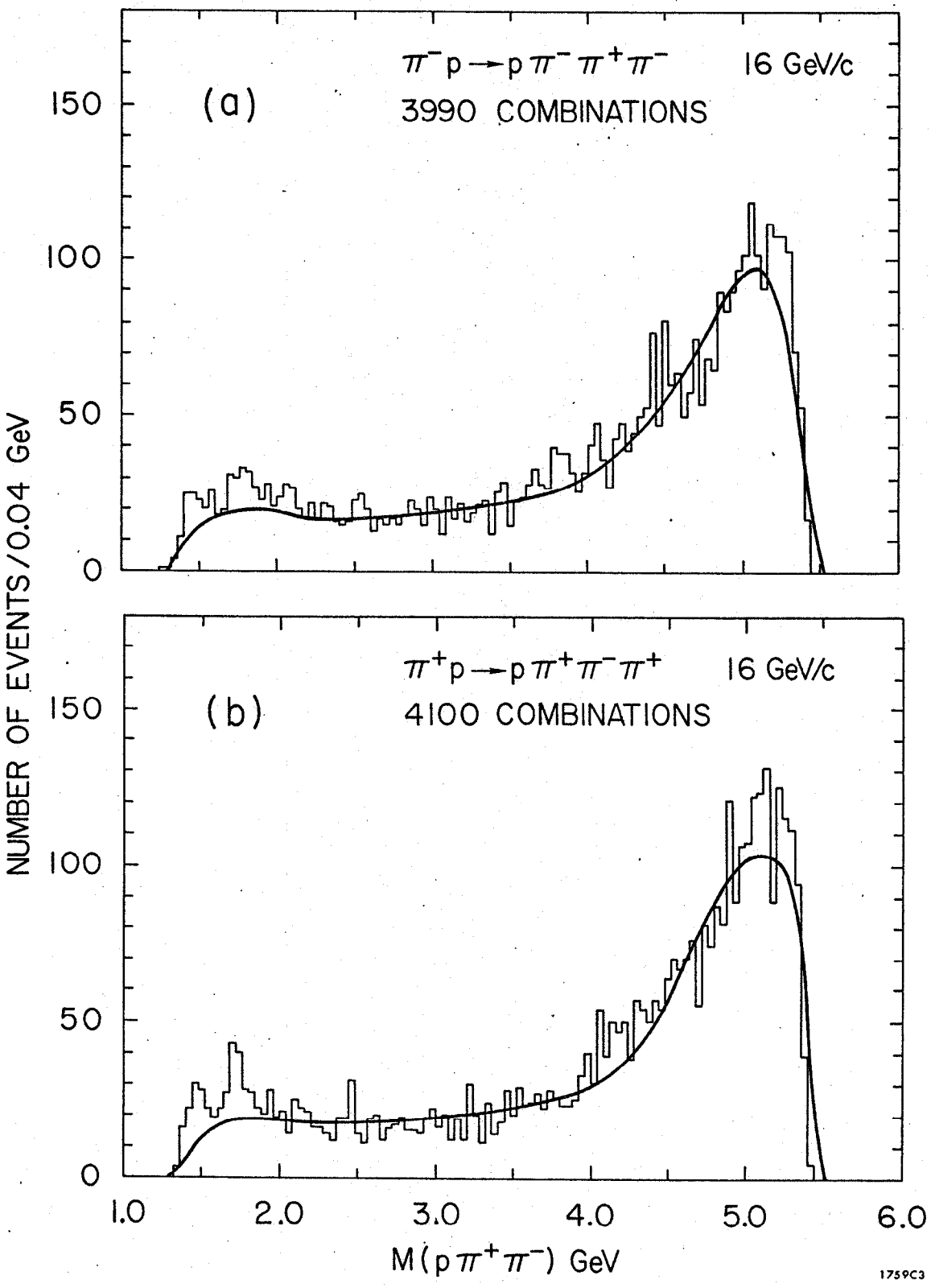
$\pi^- p \to p\pi^-\pi^+\pi^-$ 16 GeV/c
(a)
3990 COMBINATIONS
$\pi^+ p \to p\pi^+\pi^-\pi^+$ 16 GeV/c
(b)
4100 COMBINATIONS
NUMBER OF EVENTS/0.04 GeV
0
50
100
150
1.0
2.0
3.0
4.0
5.0
6.0
M(p$\pi^+\pi^-$) GeV
1759C3

Fig. 5

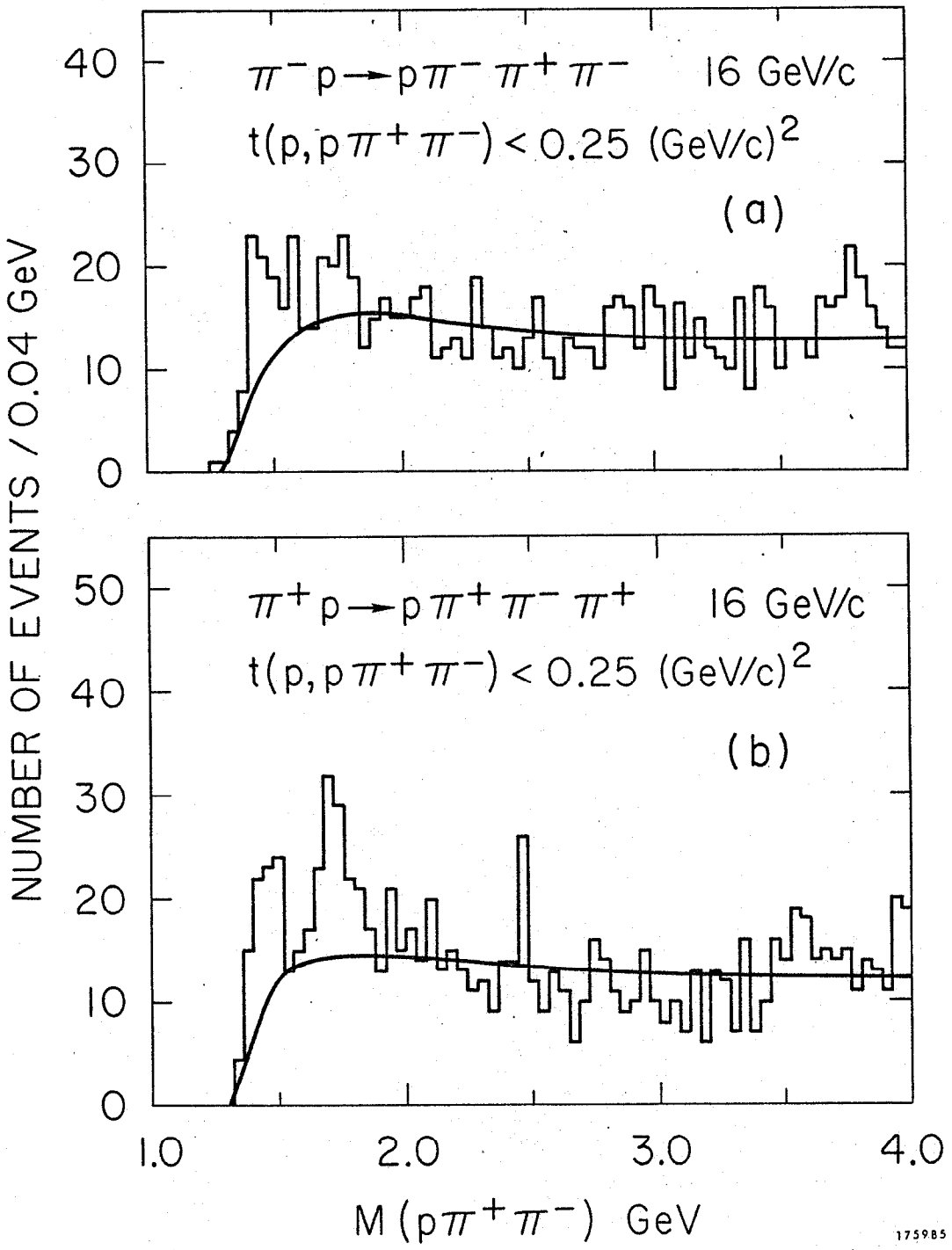
$\pi^- p \to p\pi^-\pi^+\pi^-$ 16 GeV/c
$t(p, p\pi^+\pi^-) < 0.25$ (GeV/c)^2
(a)
$\pi^+ p \to p\pi^+\pi^-\pi^+$ 16 GeV/c
$t(p, p\pi^+\pi^-) < 0.25$ (GeV/c)^2
(b)
NUMBER OF EVENTS / 0.04 GeV
0
10
20
30
40
50
1.0
2.0
3.0
4.0
M ($p\pi^+\pi^-$) GeV
175985

Fig. 6

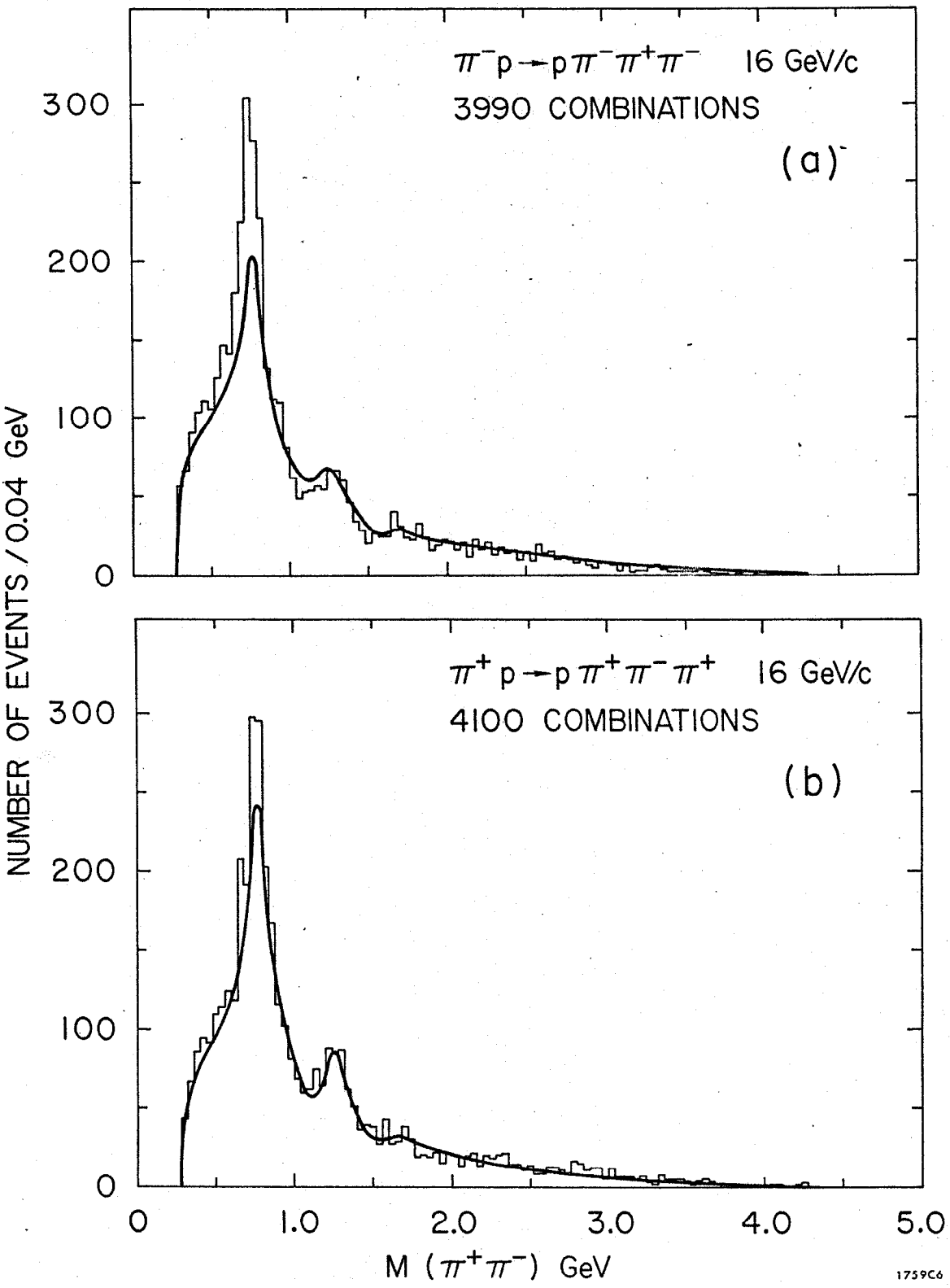
$\pi^- p \to p\pi^-\pi^+\pi^-$ 16 GeV/c
3990 COMBINATIONS
(a)
$\pi^+ p \to p\pi^+\pi^-\pi^+$ 16 GeV/c
4100 COMBINATIONS
(b)
NUMBER OF EVENTS / 0.04 GeV
0
100
200
300
0
1.0
2.0
3.0
4.0
5.0
M ($\pi^+\pi^-$) GeV
1759C6

Fig. 7

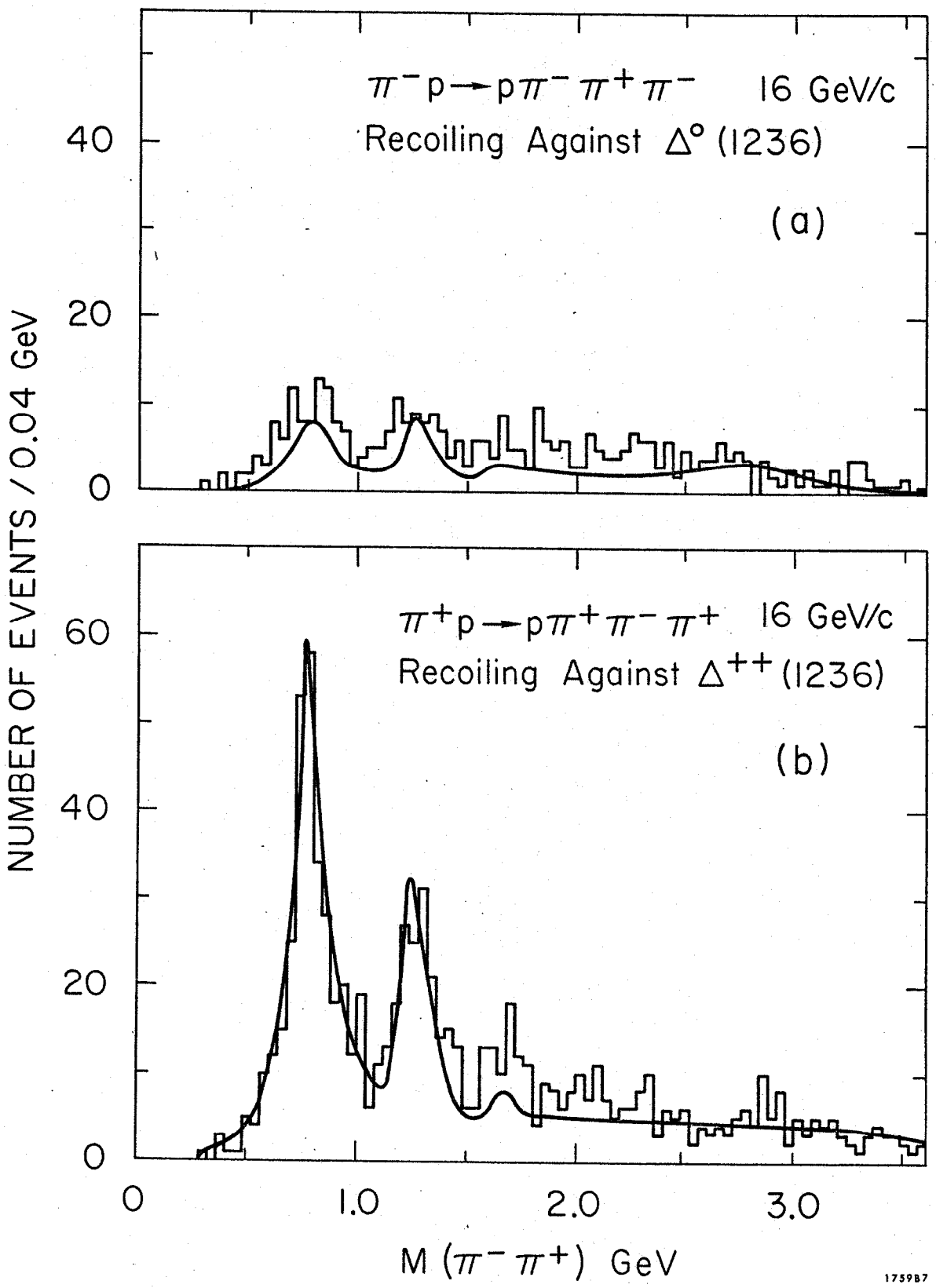
$\pi^- p \to p\pi^- \pi^+ \pi^-$ 16 GeV/c
Recoiling Against Δ^0 (1236)
(a)
$\pi^+ p \to p\pi^+ \pi^- \pi^+$ 16 GeV/c
Recoiling Against Δ^{++} (1236)
(b)
NUMBER OF EVENTS / 0.04 GeV
M ($\pi^- \pi^+$) GeV
0
20
40
60
1.0
2.0
3.0
1759B7

Fig. 8

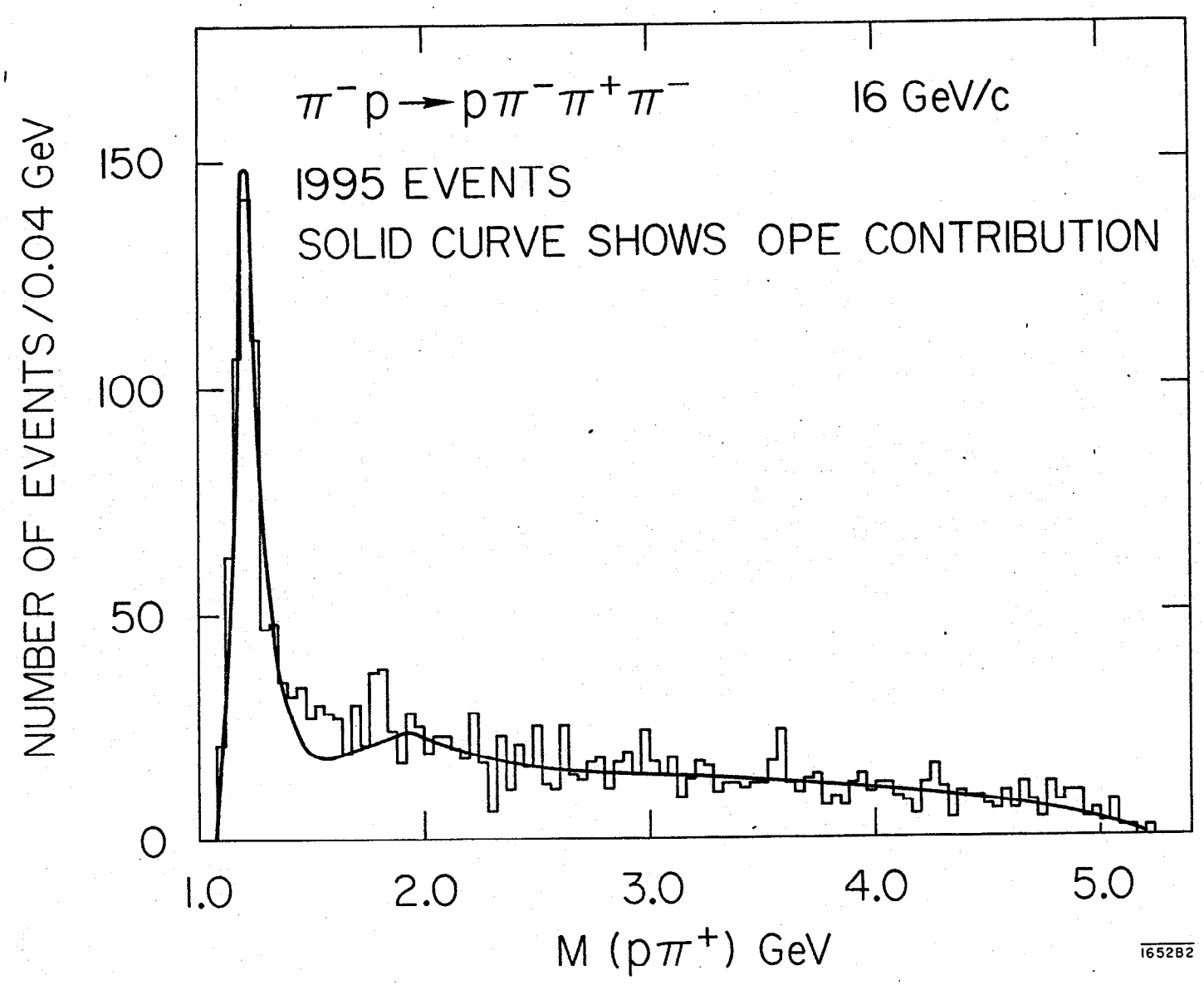
$\pi^- p \rightarrow p\pi^-\pi^+\pi^-$
16 GeV/c
1995 EVENTS
SOLID CURVE SHOWS OPE CONTRIBUTION
NUMBER OF EVENTS/0.04 GeV
150
100
50
0
1.0
2.0
3.0
4.0
5.0
M ($p\pi^+$) GeV
165282

Fig. 9a

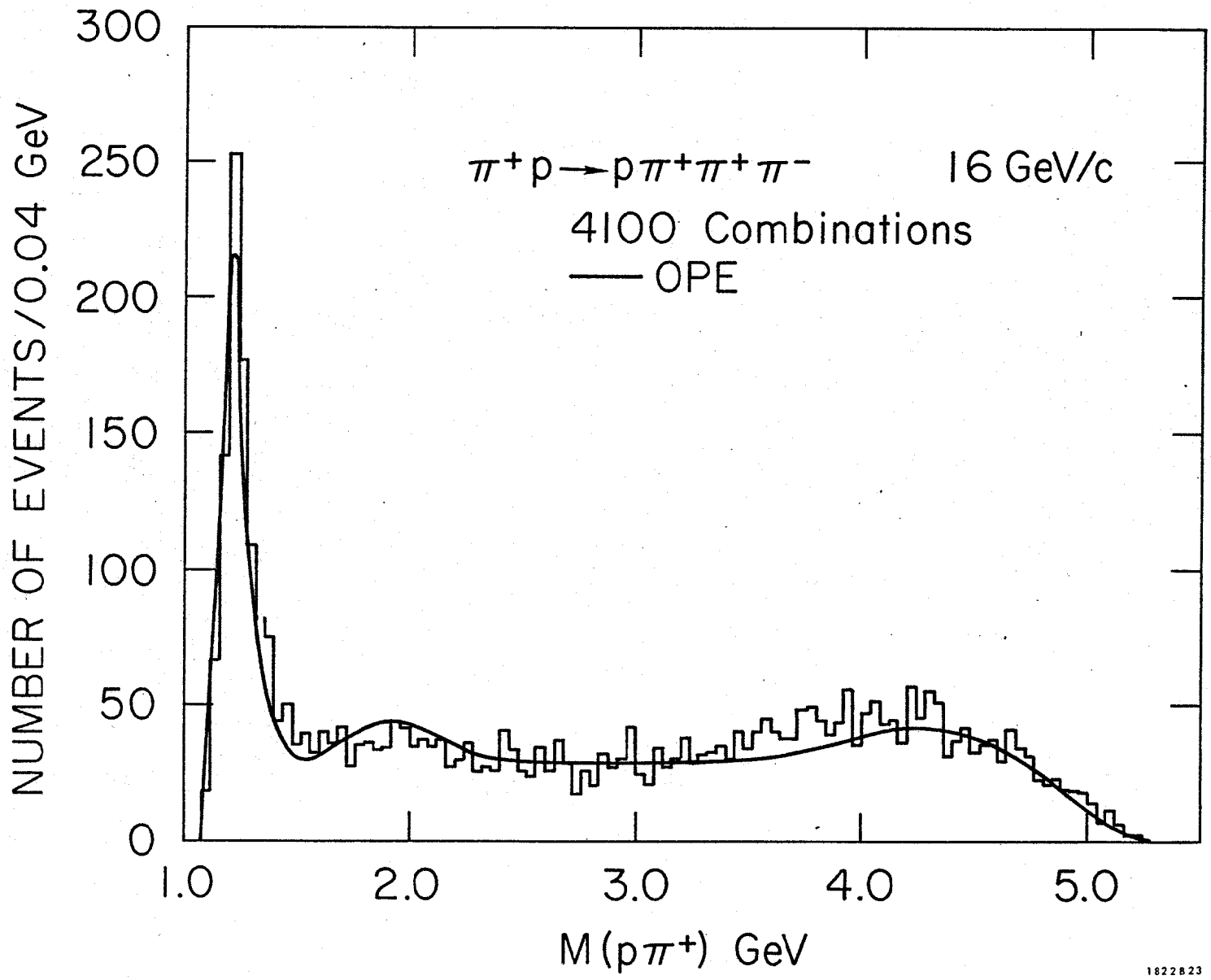
300
250
200
150
100
50
0
NUMBER OF EVENTS/0.04 GeV
$\pi^+ p \rightarrow p\pi^+\pi^+\pi^-$
16 GeV/c
4100 Combinations
OPE
1.0
2.0
3.0
4.0
5.0
M($p\pi^+$) GeV
1822B23

Fig. 9b

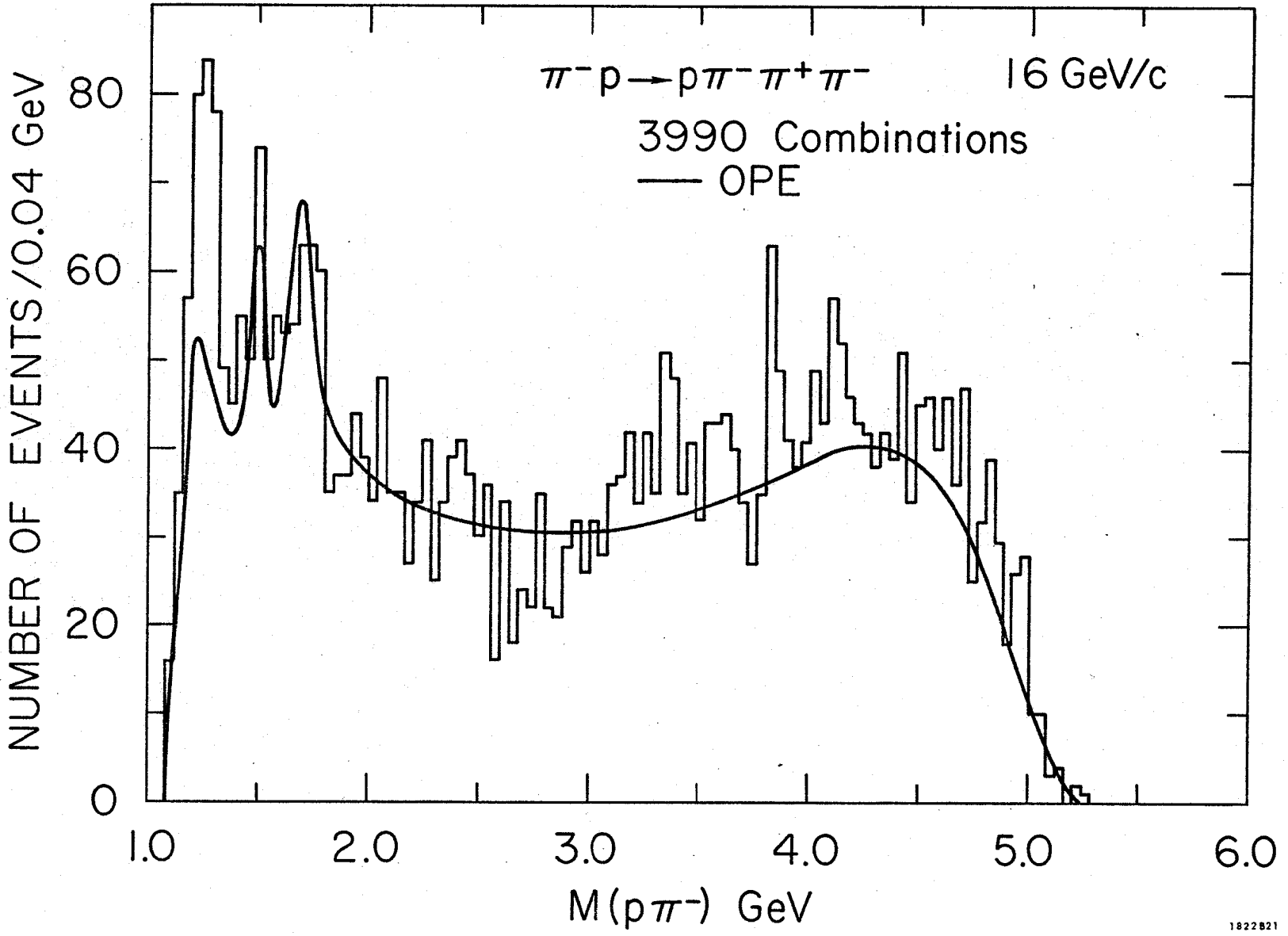
$\pi^- p \rightarrow p\pi^-\pi^+\pi^-$ 16 GeV/c
3990 Combinations
— OPE
NUMBER OF EVENTS/0.04 GeV
0
20
40
60
80
1.0
2.0
3.0
4.0
5.0
6.0
M(pπ⁻) GeV
1822B21

Fig. 10a

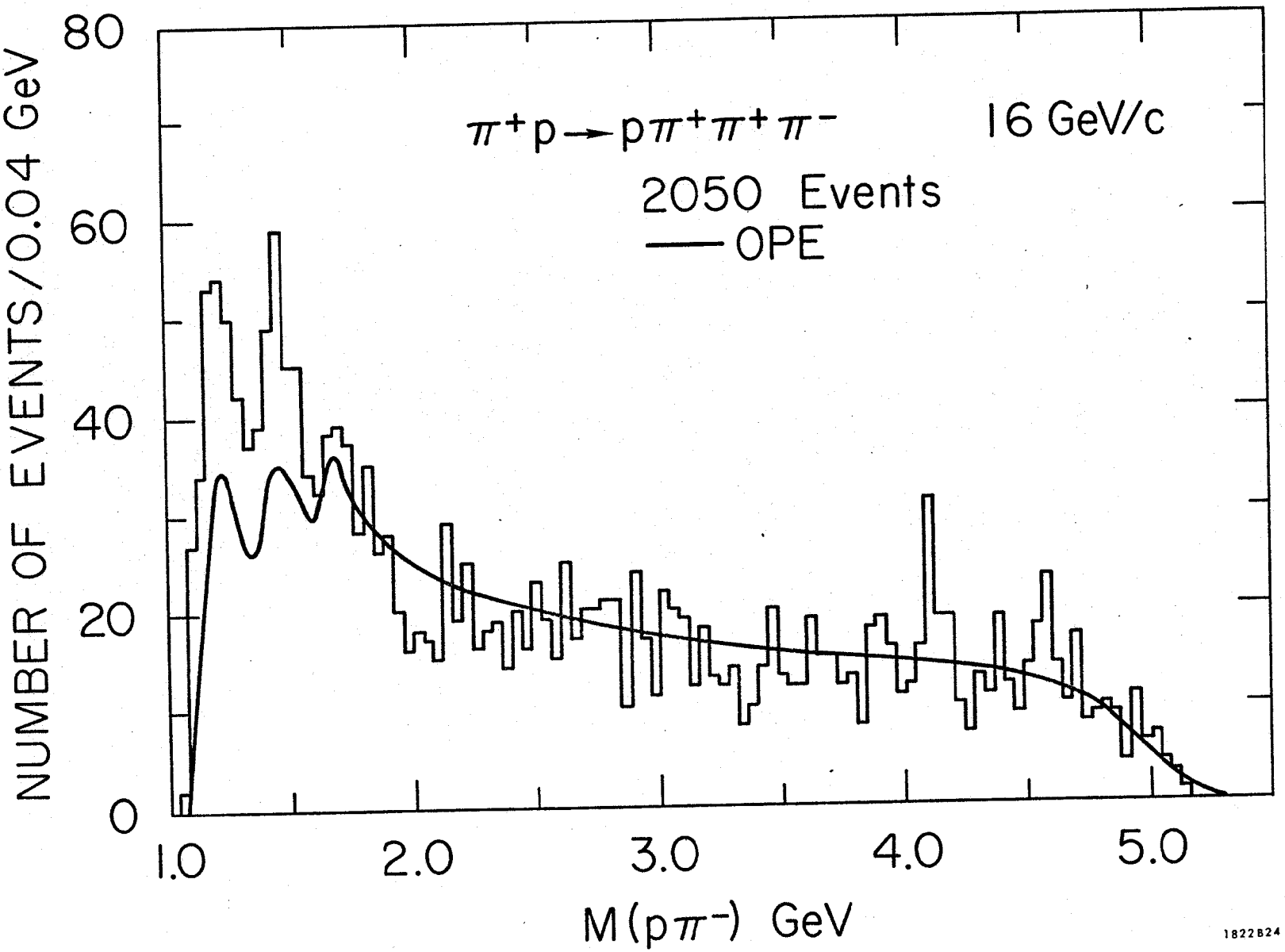
80
60
40
20
0
NUMBER OF EVENTS/0.04 GeV
$\pi^+ p \rightarrow p\pi^+\pi^+\pi^-$
16 GeV/c
2050 Events
OPE
1.0
2.0
3.0
4.0
5.0
M(pπ⁻) GeV
1822B24

Fig. 10b

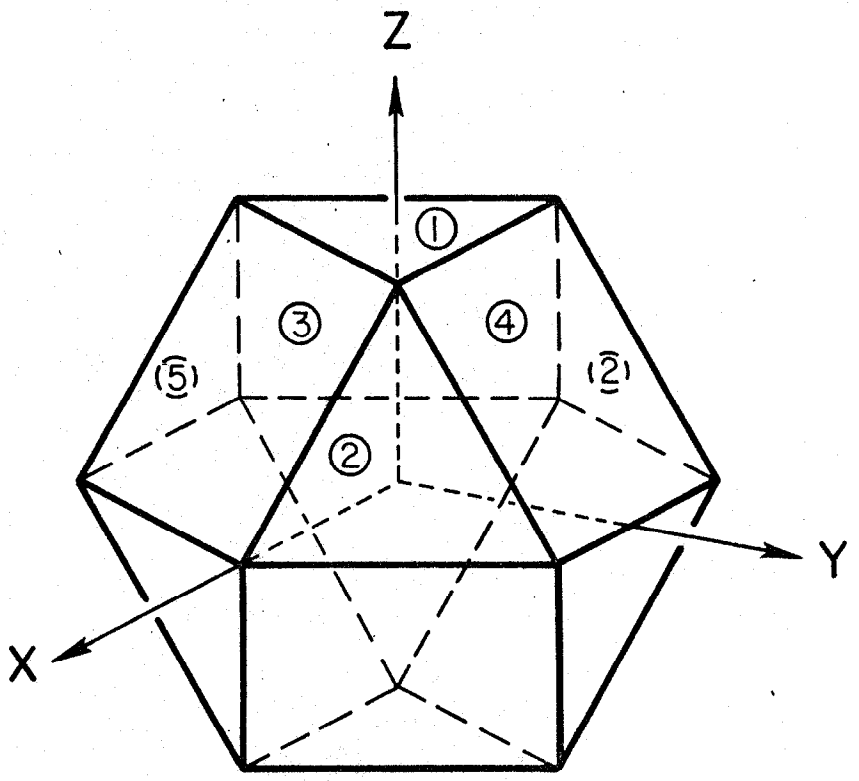

LPS CUBOCTAHEDRON

(a)

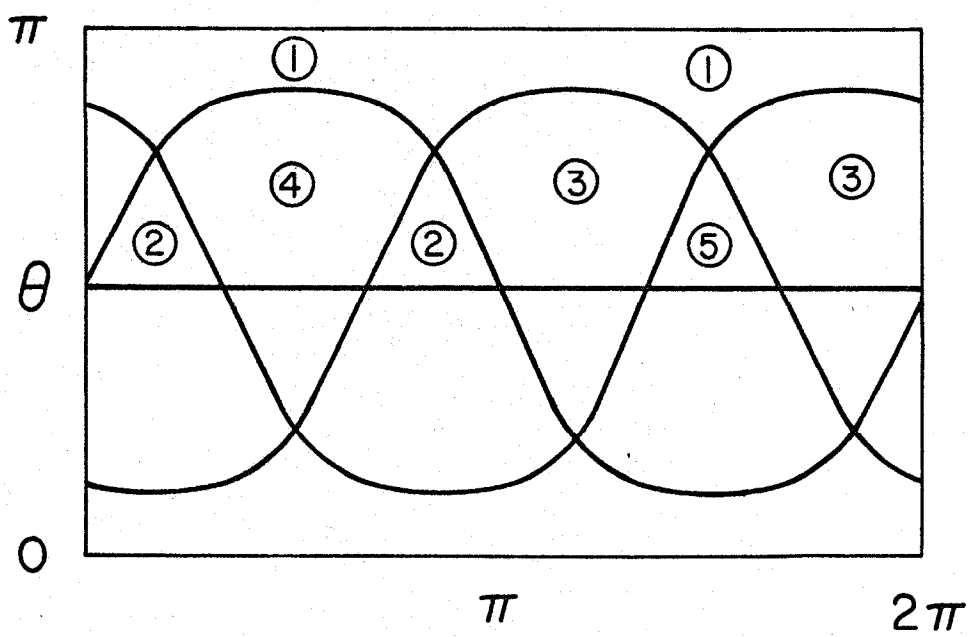

(b)

1704A2

Fig. 11
a,b

LPS REGION	QUASI-TWO-BODY REACTION	RESONANCES
1	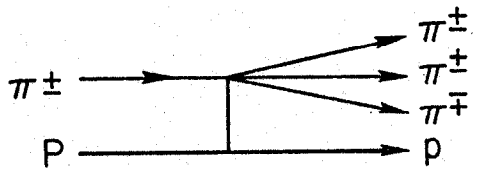	A_1, A_2, ρ, f
2	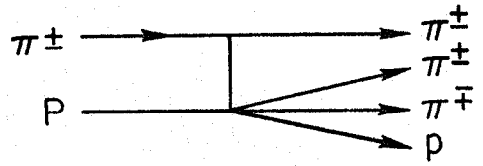	$N^*(1400), N^*(1700)$ $N^*(1236)$
3	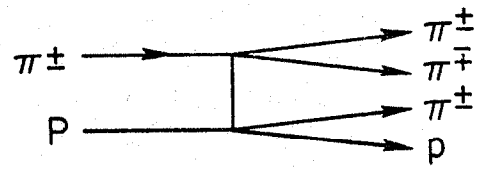	ρ, f, N^*
4	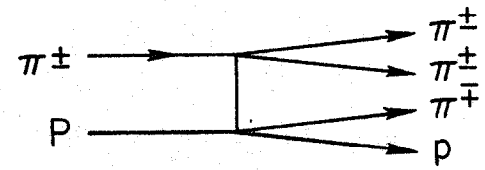	N^*
5	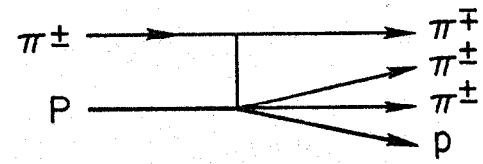	

1704A1

Fig. 11c

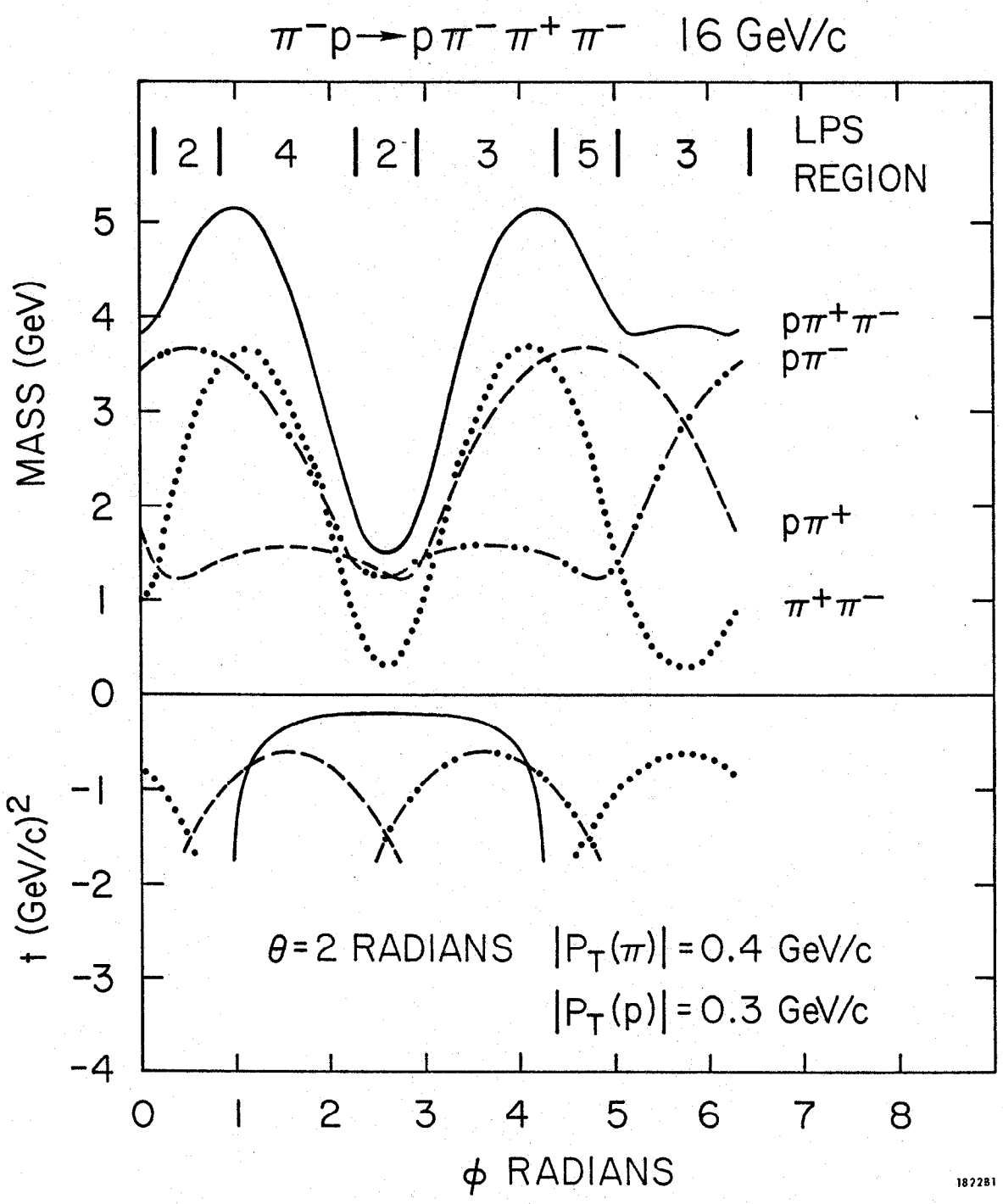
$\pi^- p \rightarrow p\pi^-\pi^+\pi^-$ 16 GeV/c
2
4
2
3
5
3
LPS REGION
MASS (GeV)
$p\pi^+\pi^-$
$p\pi^-$
$p\pi^+$
$\pi^+\pi^-$
t (GeV/c)^2
θ = 2 RADIANS
$|P_T(\pi)|$ = 0.4 GeV/c
$|P_T(p)|$ = 0.3 GeV/c
ϕ RADIANS
182281

Fig. 12

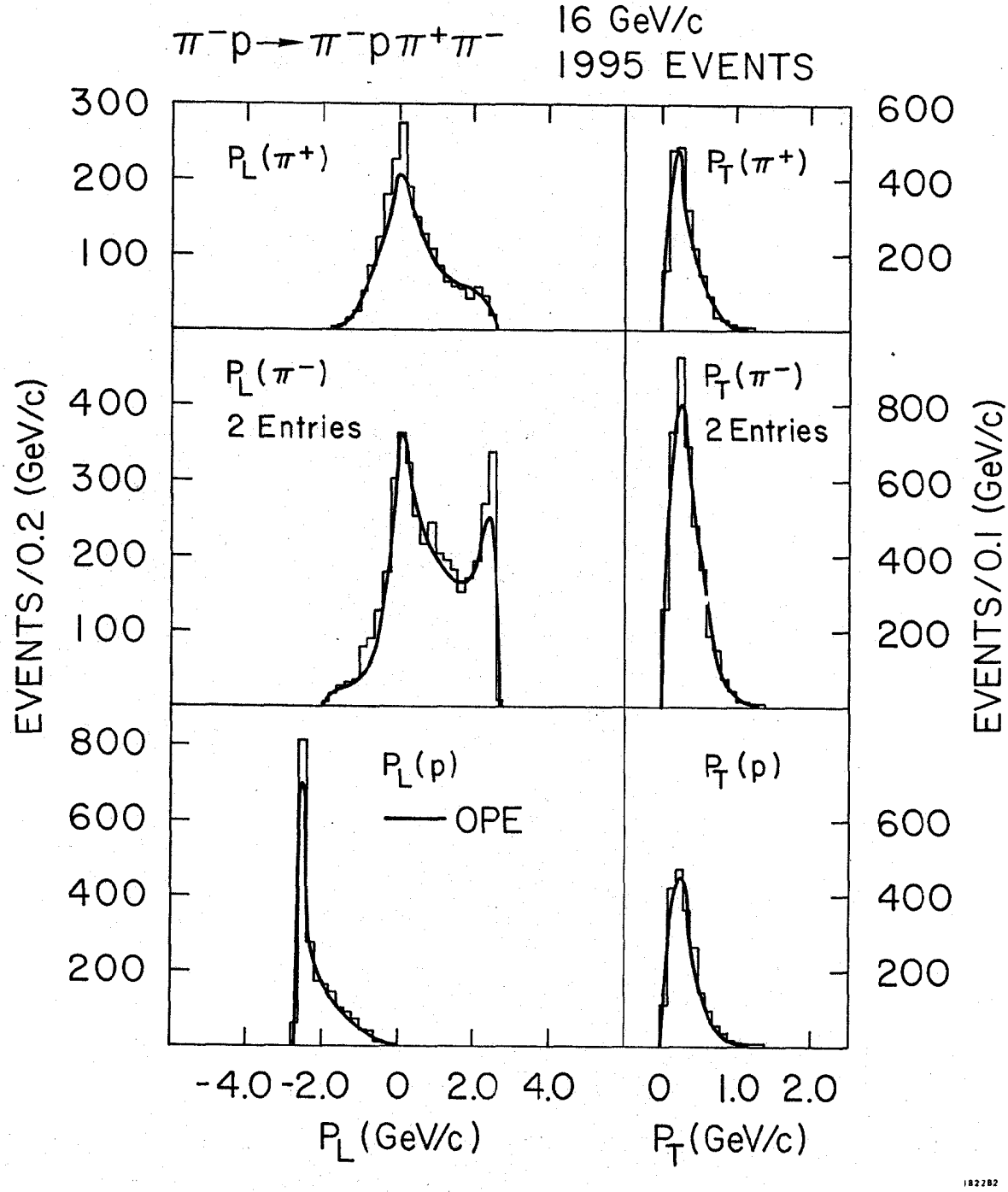
$\pi^- p \rightarrow \pi^- p \pi^+ \pi^-$
16 GeV/c
1995 EVENTS
$P_L(\pi^+)$
$P_T(\pi^+)$
$P_L(\pi^-)$
2 Entries
$P_T(\pi^-)$
2 Entries
$P_L(p)$
OPE
$P_T(p)$
EVENTS/0.2 (GeV/c)
EVENTS/0.1 (GeV/c)
P_L (GeV/c)
P_T (GeV/c)
182282

Fig. 13

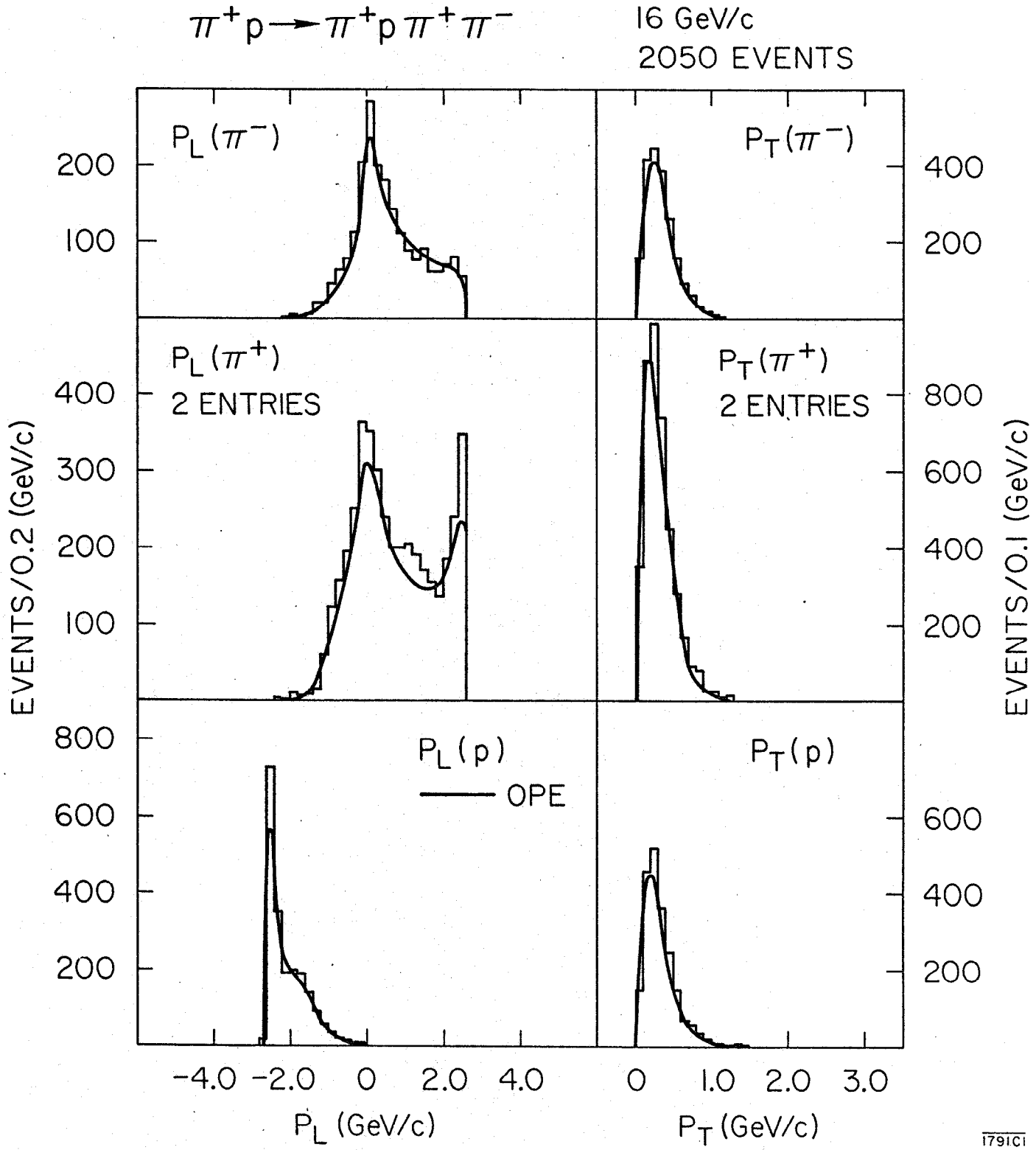
$\pi^+ p \rightarrow \pi^+ p \pi^+ \pi^-$
16 GeV/c
2050 EVENTS
$P_L(\pi^-)$
$P_T(\pi^-)$
$P_L(\pi^+)$
2 ENTRIES
$P_T(\pi^+)$
2 ENTRIES
$P_L(p)$
OPE
$P_T(p)$
EVENTS/0.2 (GeV/c)
EVENTS/0.1 (GeV/c)
P_L (GeV/c)
P_T (GeV/c)
1791C1

Fig. 14

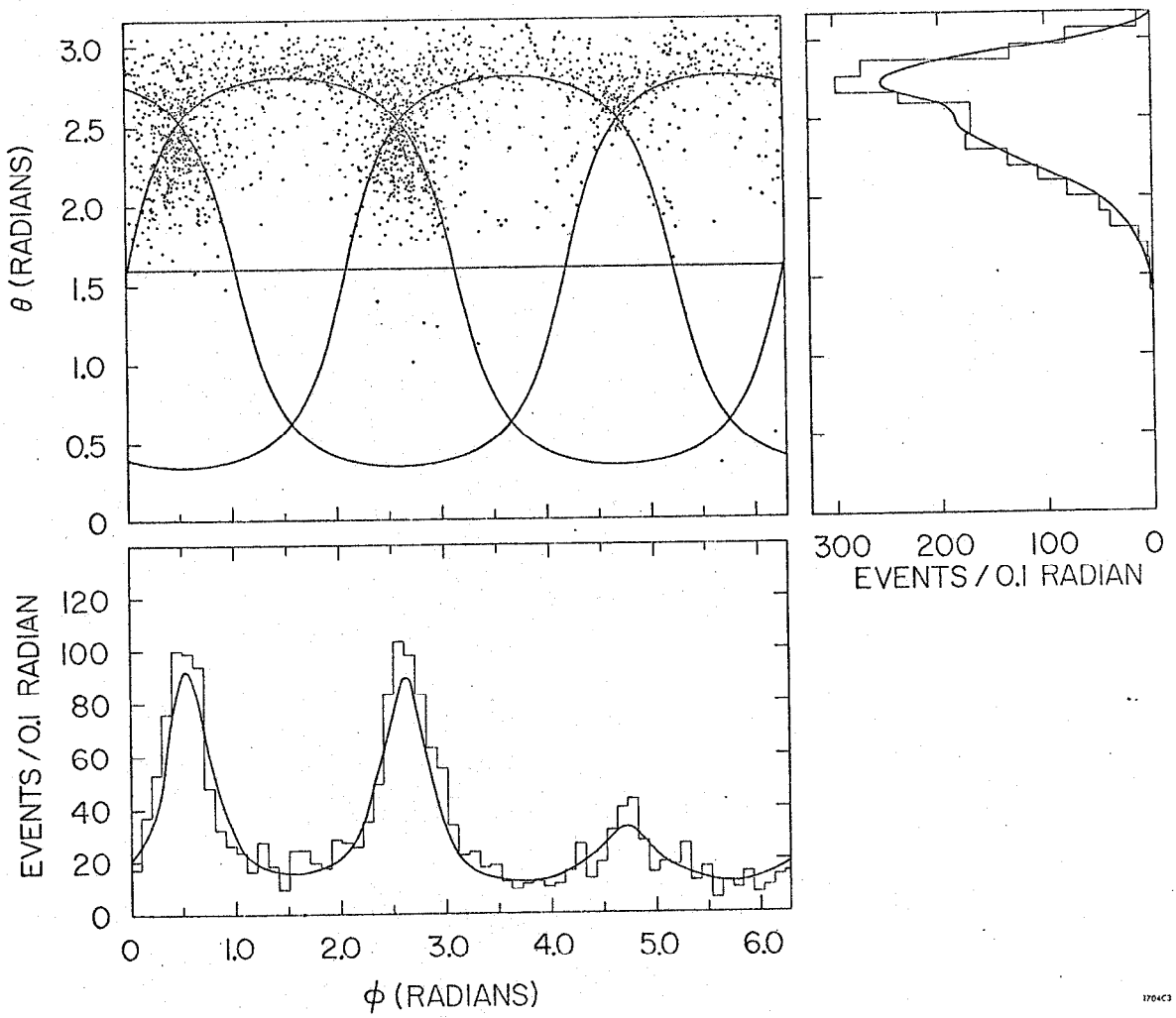
θ (RADIANS)
3.0
2.5
2.0
1.5
1.0
0.5
0
300
200
100
0
EVENTS / 0.1 RADIAN
EVENTS / 0.1 RADIAN
120
100
80
60
40
20
0
0
1.0
2.0
3.0
4.0
5.0
6.0
φ (RADIANS)

Fig. 15

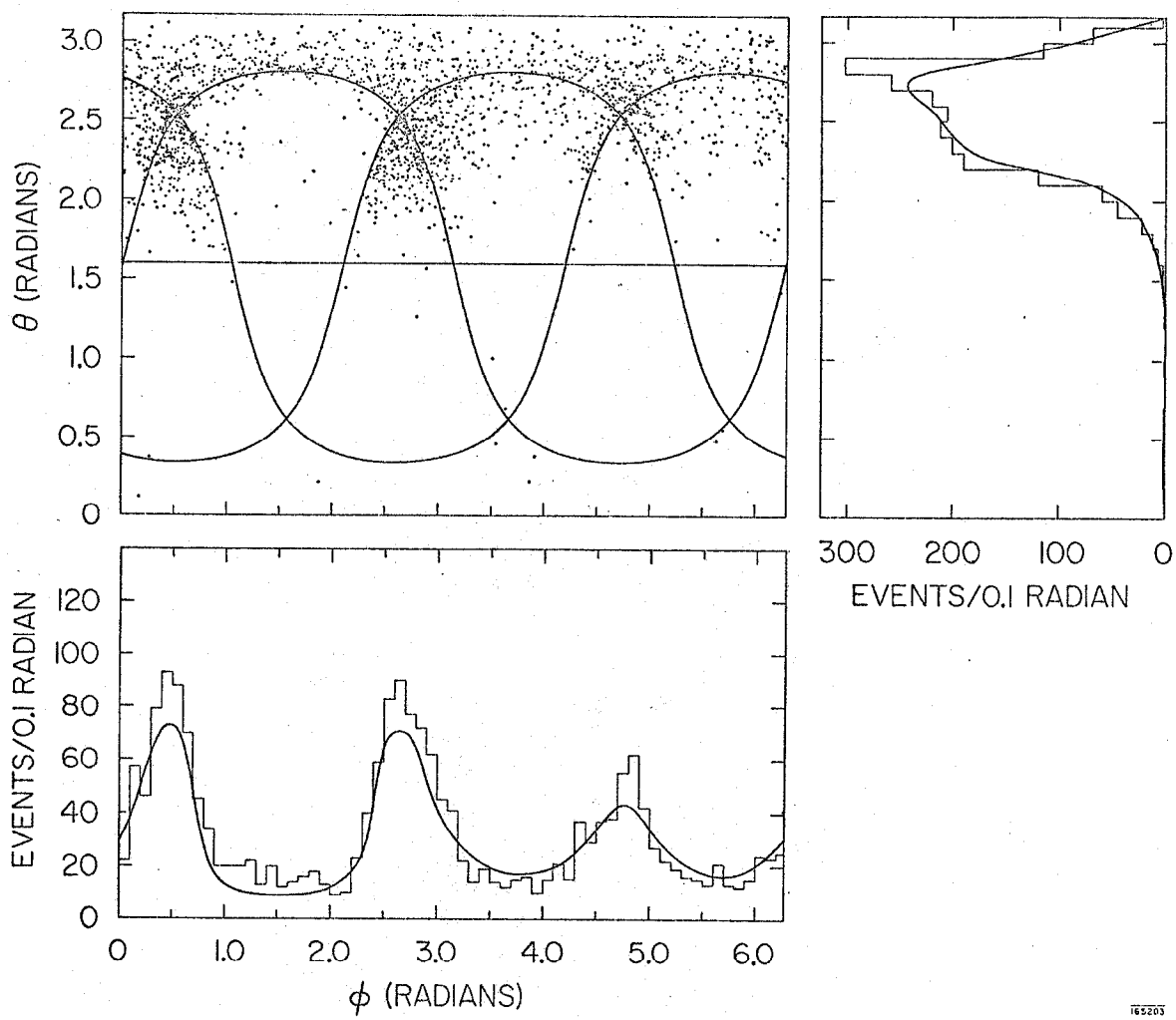
θ (RADIANS)
3.0
2.5
2.0
1.5
1.0
0.5
0
300
200
100
0
EVENTS/0.1 RADIAN
EVENTS/0.1 RADIAN
120
100
80
60
40
20
0
0
1.0
2.0
3.0
4.0
5.0
6.0
φ (RADIANS)
165203

Fig 16

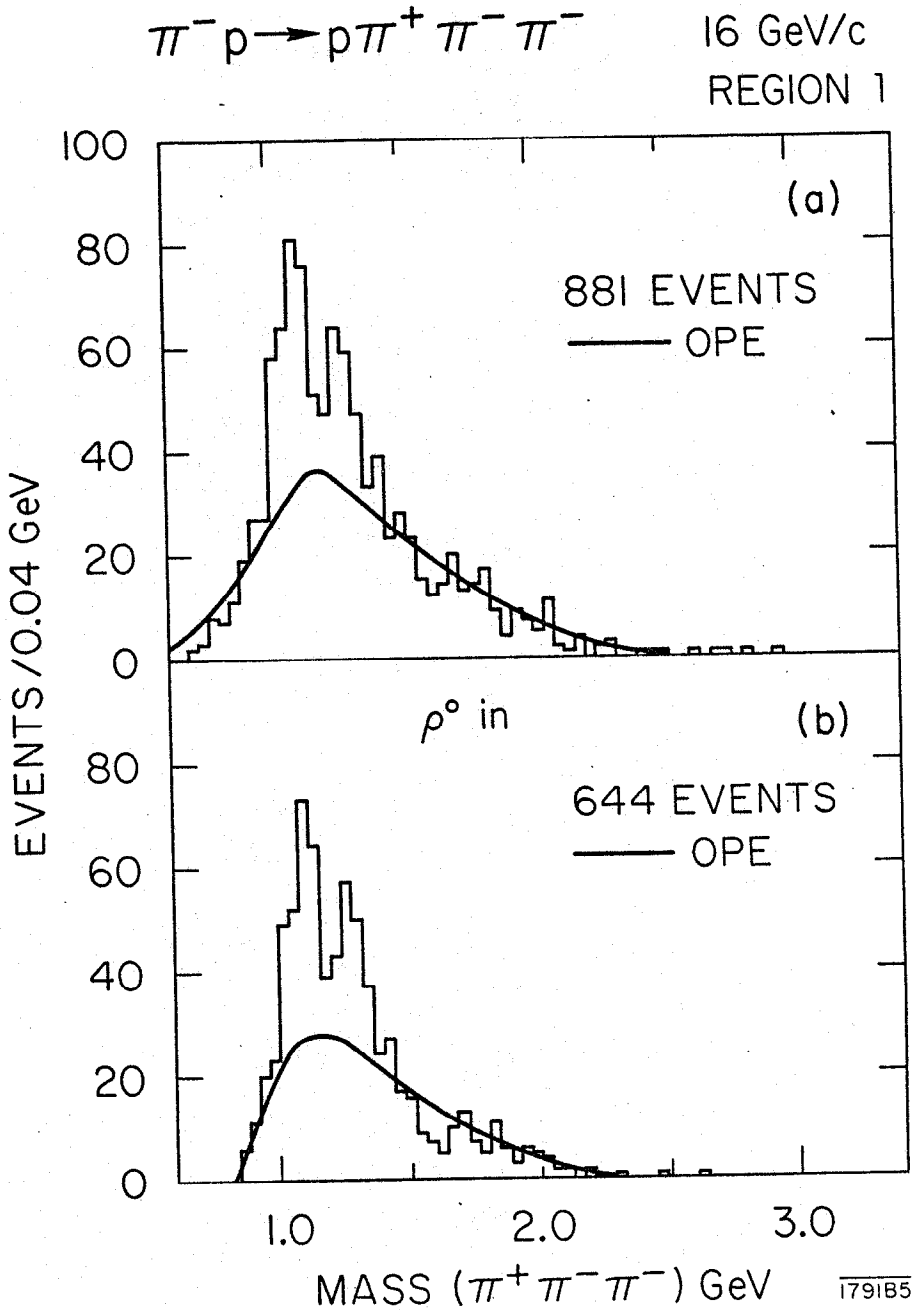
$\pi^- p \rightarrow p\pi^+\pi^-\pi^-$
16 GeV/c
REGION 1
(a)
881 EVENTS
OPE
ρ° in
(b)
644 EVENTS
OPE
EVENTS/0.04 GeV
MASS $(\pi^+\pi^-\pi^-)$ GeV
179185

Fig. 17

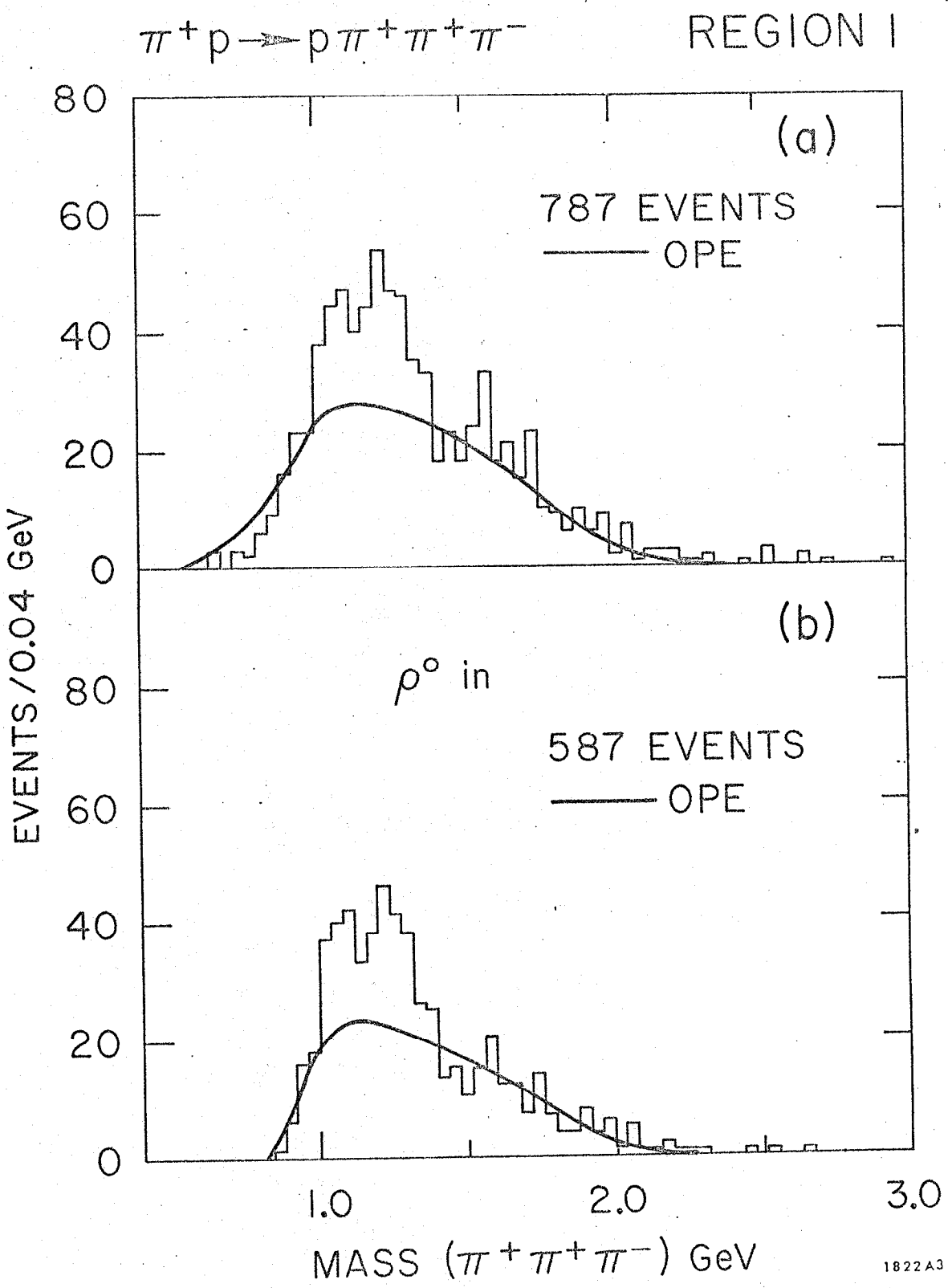
$\pi^+ p \rightarrow p\pi^+\pi^+\pi^-$
REGION I
(a)
787 EVENTS
OPE
(b)
ρ° in
587 EVENTS
OPE
EVENTS/0.04 GeV
MASS $(\pi^+\pi^+\pi^-)$ GeV
1822A3

Fig. 18

DECK MECHANISM DIAGRAMS

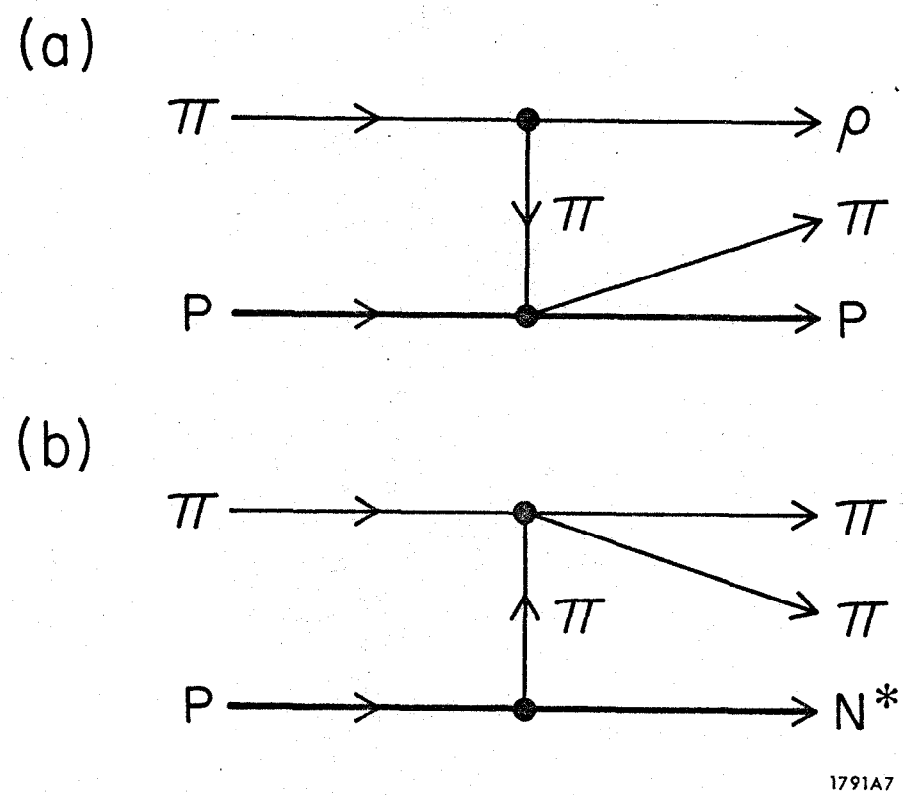

Fig. 19

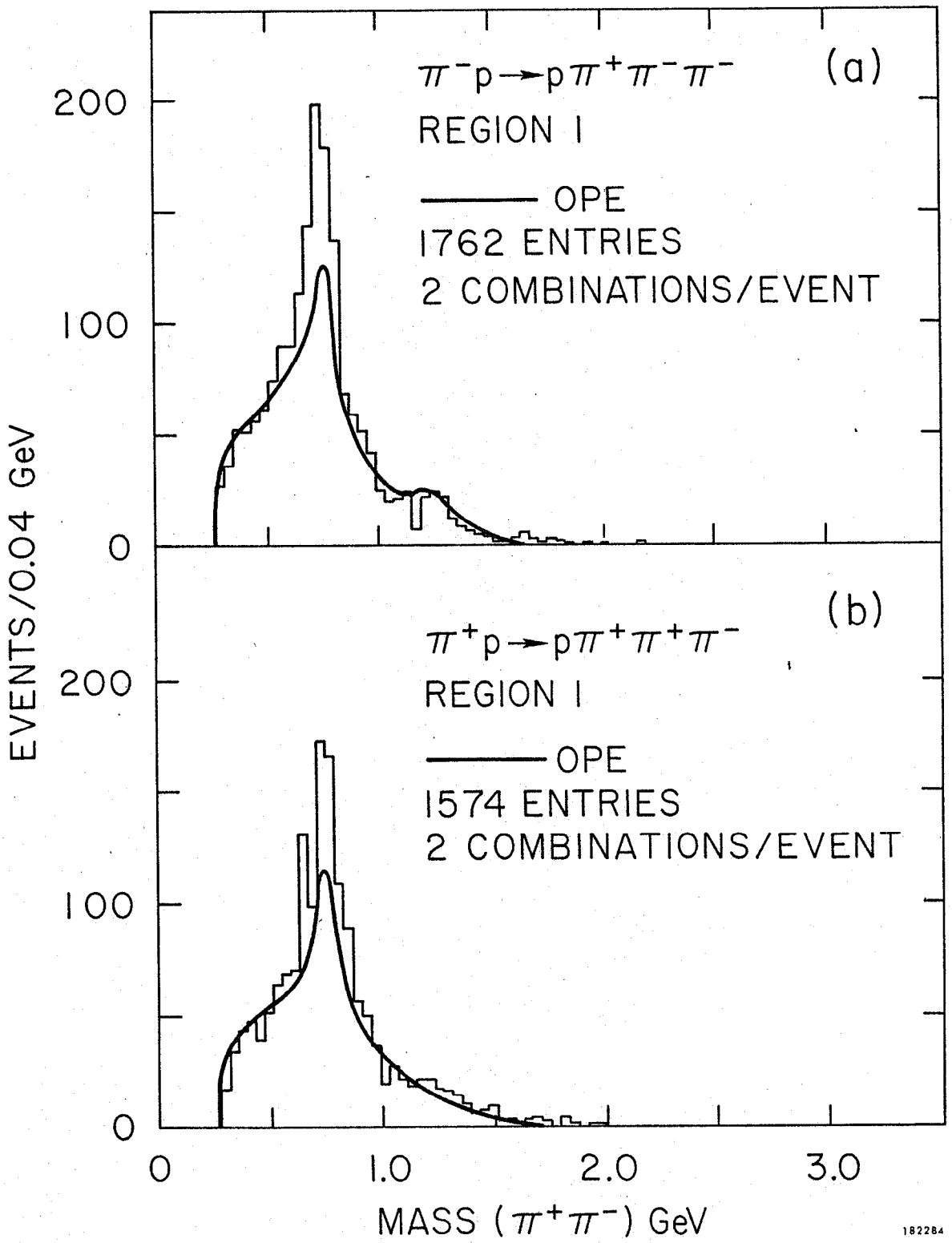
$\pi^- p \to p\pi^+\pi^-\pi^-$
(a)
REGION I
OPE
1762 ENTRIES
2 COMBINATIONS/EVENT
$\pi^+ p \to p\pi^+\pi^+\pi^-$
(b)
REGION I
OPE
1574 ENTRIES
2 COMBINATIONS/EVENT
EVENTS/0.04 GeV
200
100
0
200
100
0
0
1.0
2.0
3.0
MASS ($\pi^+\pi^-$) GeV
182284

Fig. 20

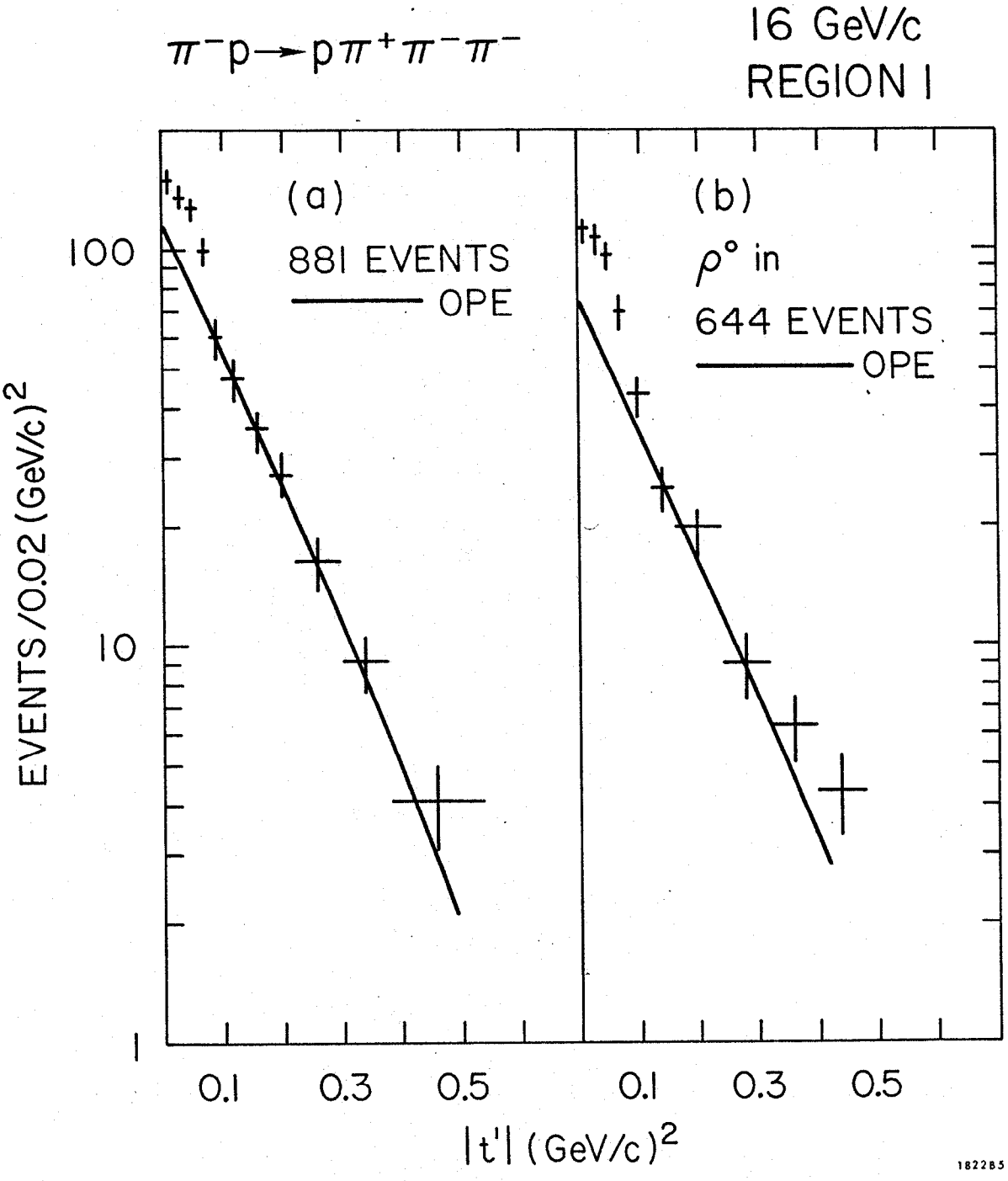
$\pi^- p \rightarrow p\pi^+\pi^-\pi^-$
16 GeV/c
REGION I
(a)
881 EVENTS
OPE
(b)
ρ° in
644 EVENTS
OPE
100
10
1
EVENTS/0.02 (GeV/c)^2
0.1
0.3
0.5
0.1
0.3
0.5
$|t'|$ (GeV/c)^2
1822B5

Fig. 21

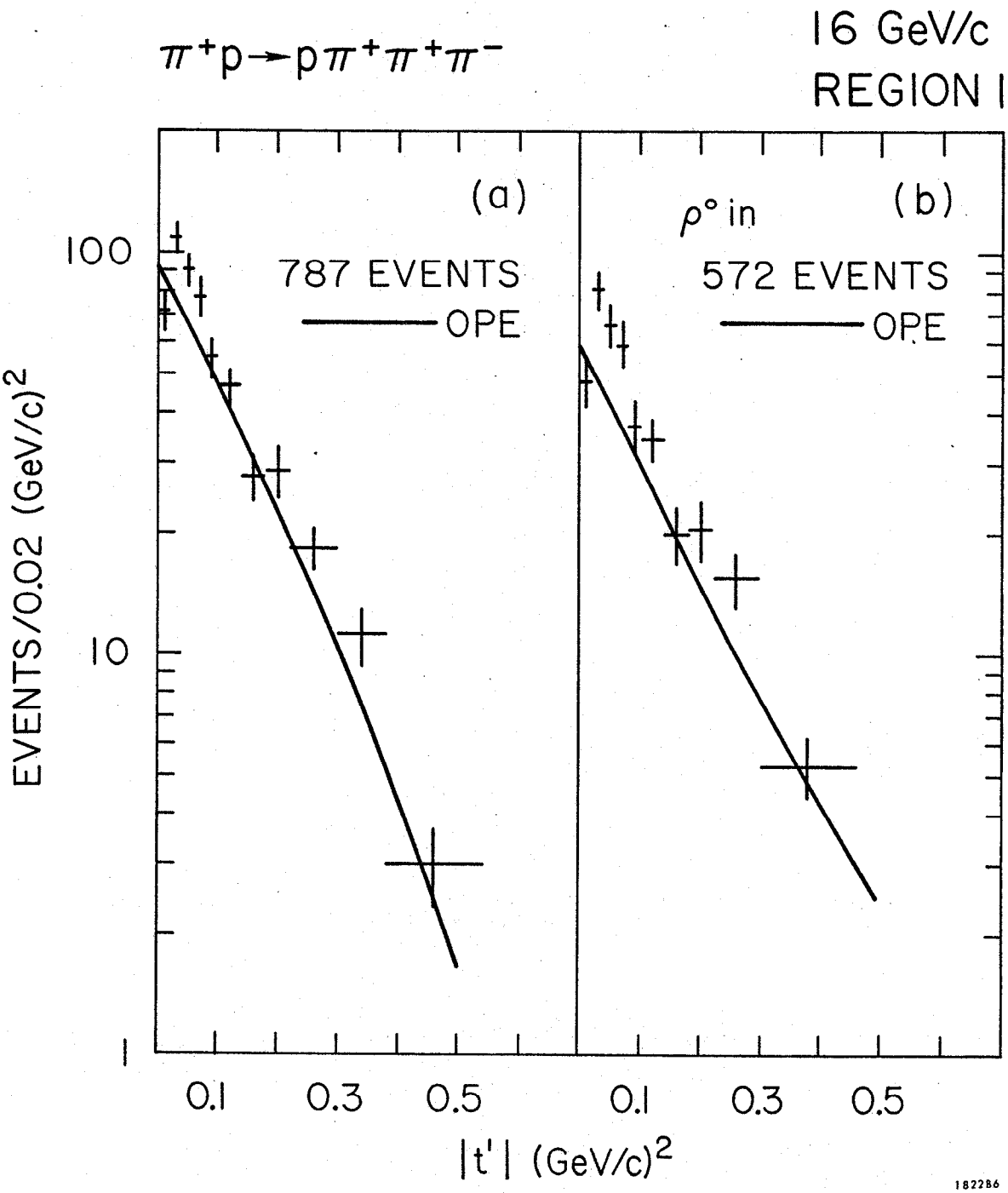
$\pi^+p \rightarrow p\pi^+\pi^+\pi^-$
16 GeV/c
REGION I
(a)
787 EVENTS
OPE
ρ° in
(b)
572 EVENTS
OPE
100
10
1
EVENTS/0.02 (GeV/c)^2
0.1
0.3
0.5
0.1
0.3
0.5
$|t'|$ (GeV/c)^2
182286

Fig. 22

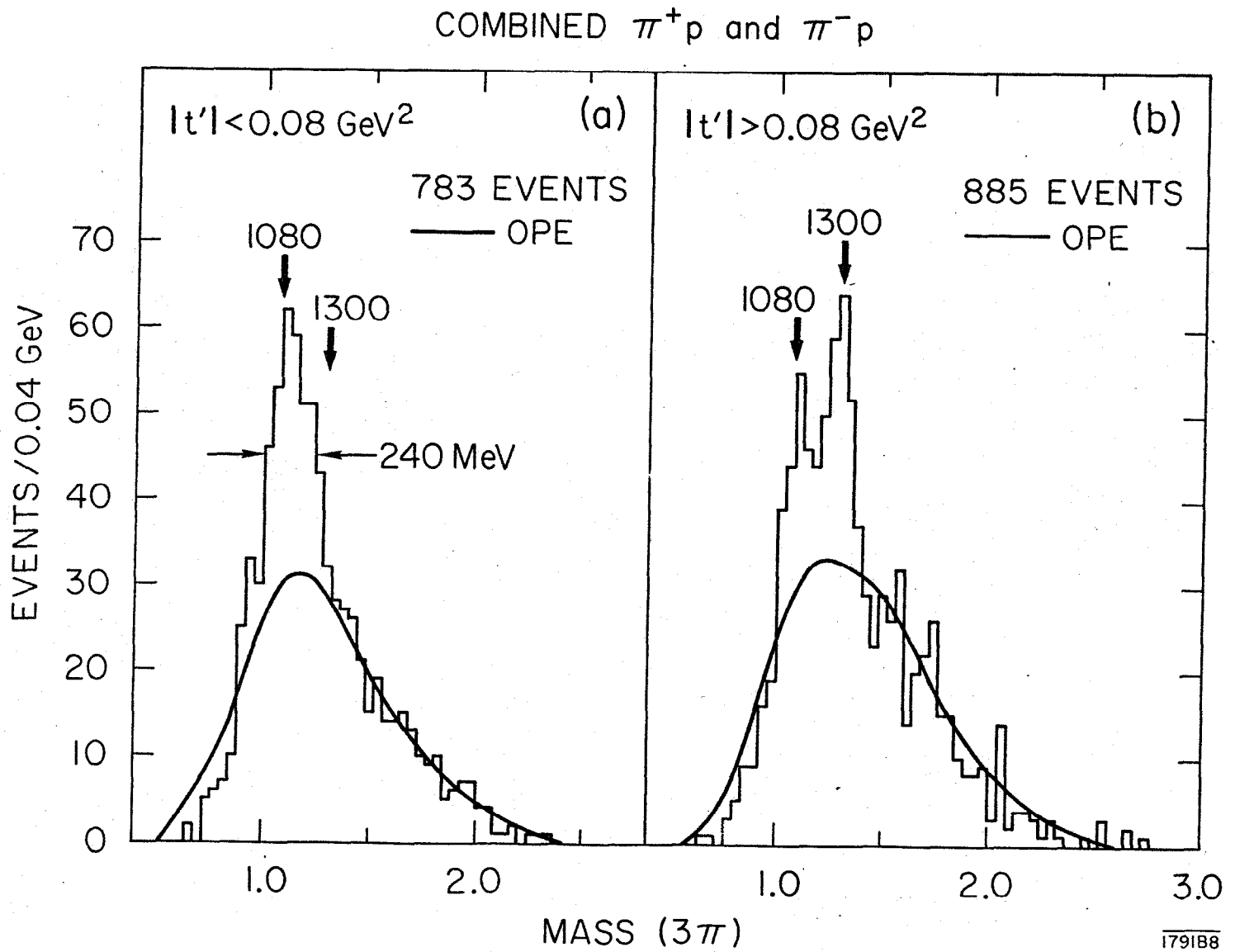
COMBINED π^+p and π^-p
$|t'|<0.08$ GeV^2
(a)
783 EVENTS
OPE
1080
1300
240 MeV
$|t'|>0.08$ GeV^2
(b)
885 EVENTS
OPE
1300
1080
EVENTS/0.04 GeV
0
10
20
30
40
50
60
70
1.0
2.0
1.0
2.0
3.0
MASS (3π)
179188

Fig. 23

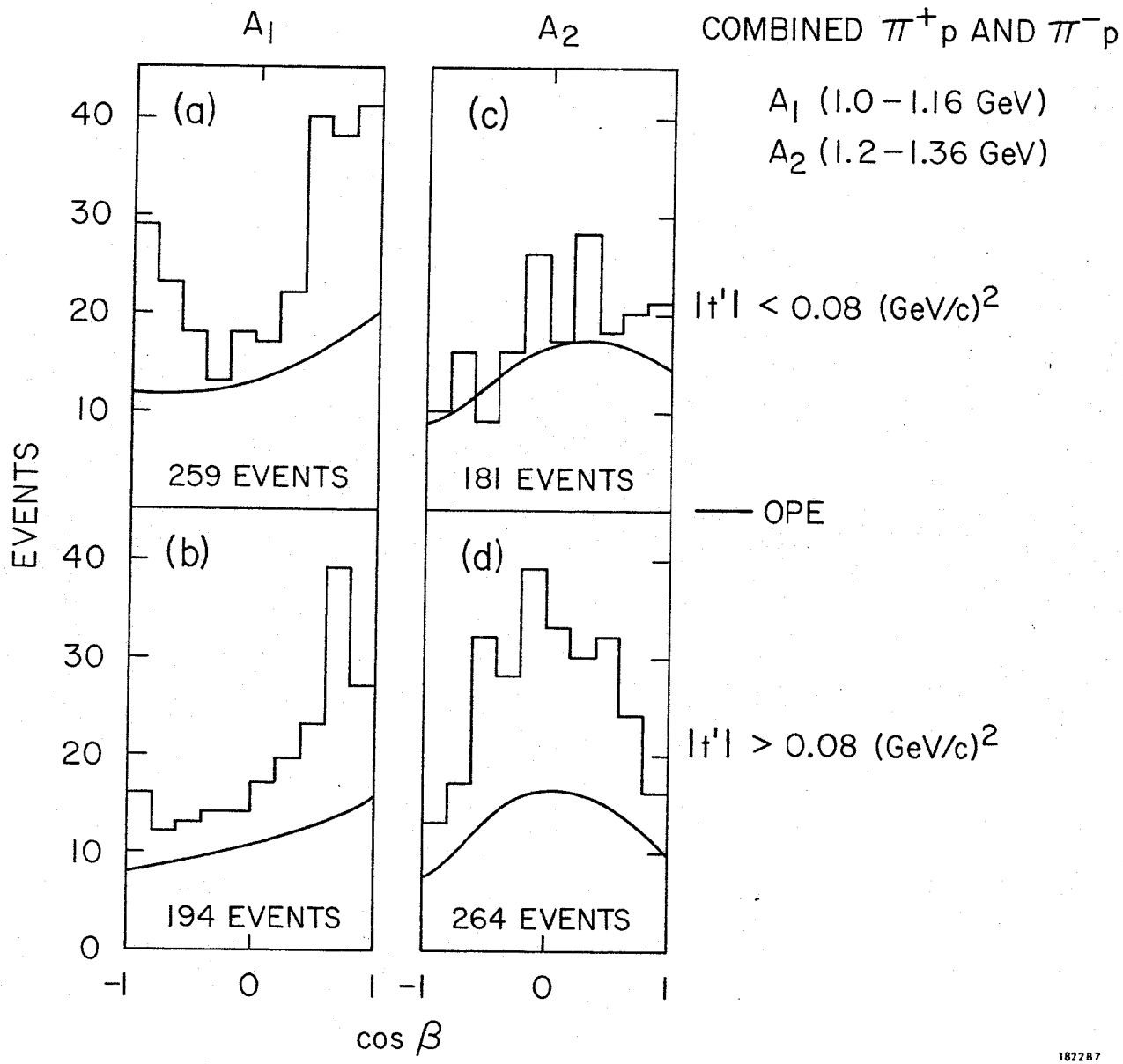
A1
A2
COMBINED π+p AND π−p
A1 (1.0 − 1.16 GeV)
A2 (1.2 − 1.36 GeV)
(a)
(c)
(b)
(d)
259 EVENTS
181 EVENTS
194 EVENTS
264 EVENTS
|t'| < 0.08 (GeV/c)2
|t'| > 0.08 (GeV/c)2
OPE
EVENTS
cos β
182287

Fig. 24

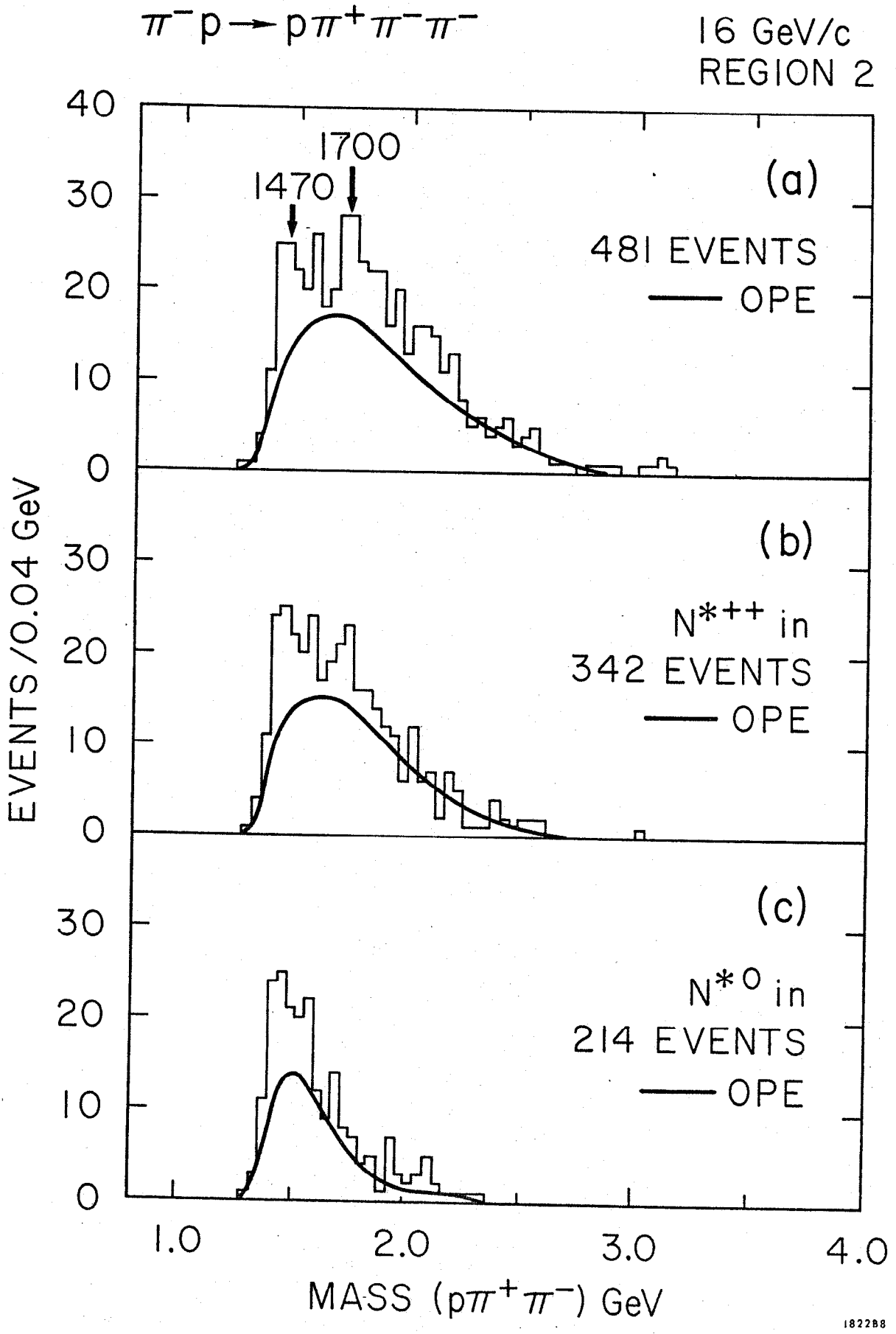
$\pi^- p \rightarrow p\pi^+\pi^-\pi^-$
16 GeV/c
REGION 2
1700
1470
(a)
481 EVENTS
OPE
(b)
N^{*++} in
342 EVENTS
OPE
(c)
N^{*0} in
214 EVENTS
OPE
EVENTS/0.04 GeV
MASS $(p\pi^+\pi^-)$ GeV
1822B8

Fig. 25

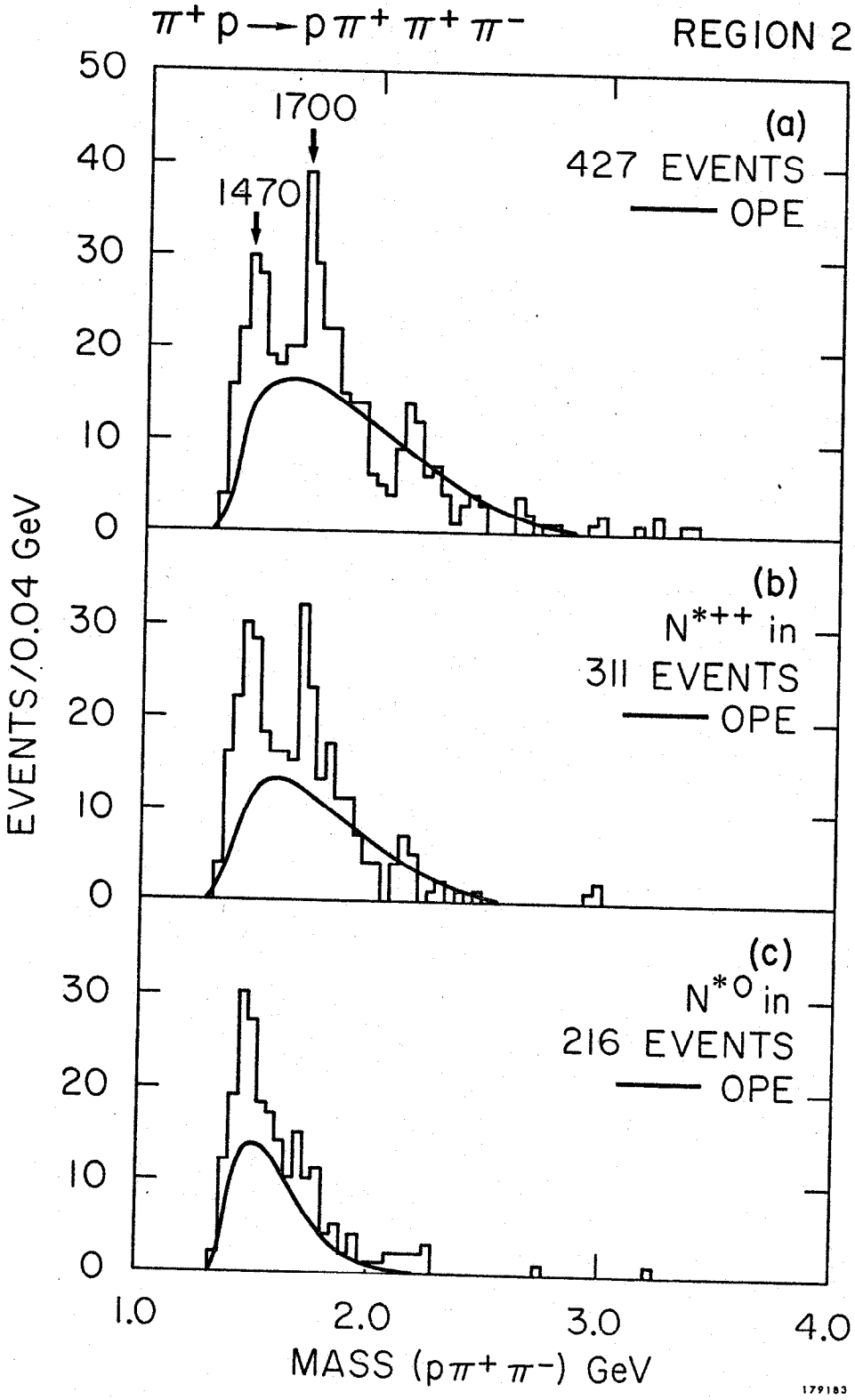
$\pi^+ p \rightarrow p\pi^+\pi^+\pi^-$
REGION 2
1700
1470
(a)
427 EVENTS
OPE
(b)
N^{*++} in
311 EVENTS
OPE
(c)
N^{*0} in
216 EVENTS
OPE
EVENTS/0.04 GeV
MASS ($p\pi^+\pi^-$) GeV
179183

Fig. 26

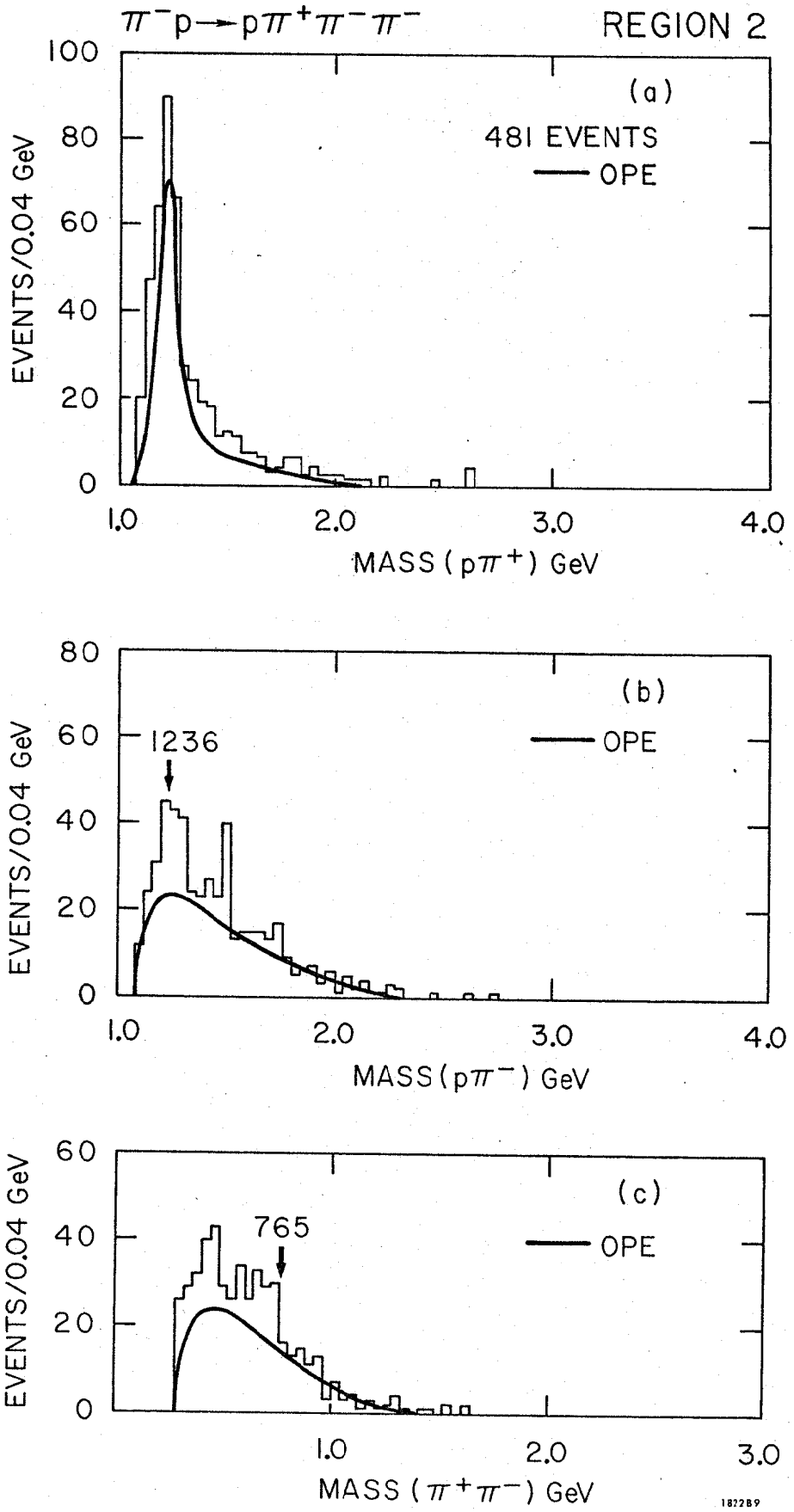
$\pi^- p \to p\pi^+\pi^-\pi^-$
REGION 2
(a)
481 EVENTS
OPE
EVENTS/0.04 GeV
MASS ($p\pi^+$) GeV
(b)
1236
OPE
EVENTS/0.04 GeV
MASS ($p\pi^-$) GeV
(c)
765
OPE
EVENTS/0.04 GeV
MASS ($\pi^+\pi^-$) GeV
1822B9

Fig. 27

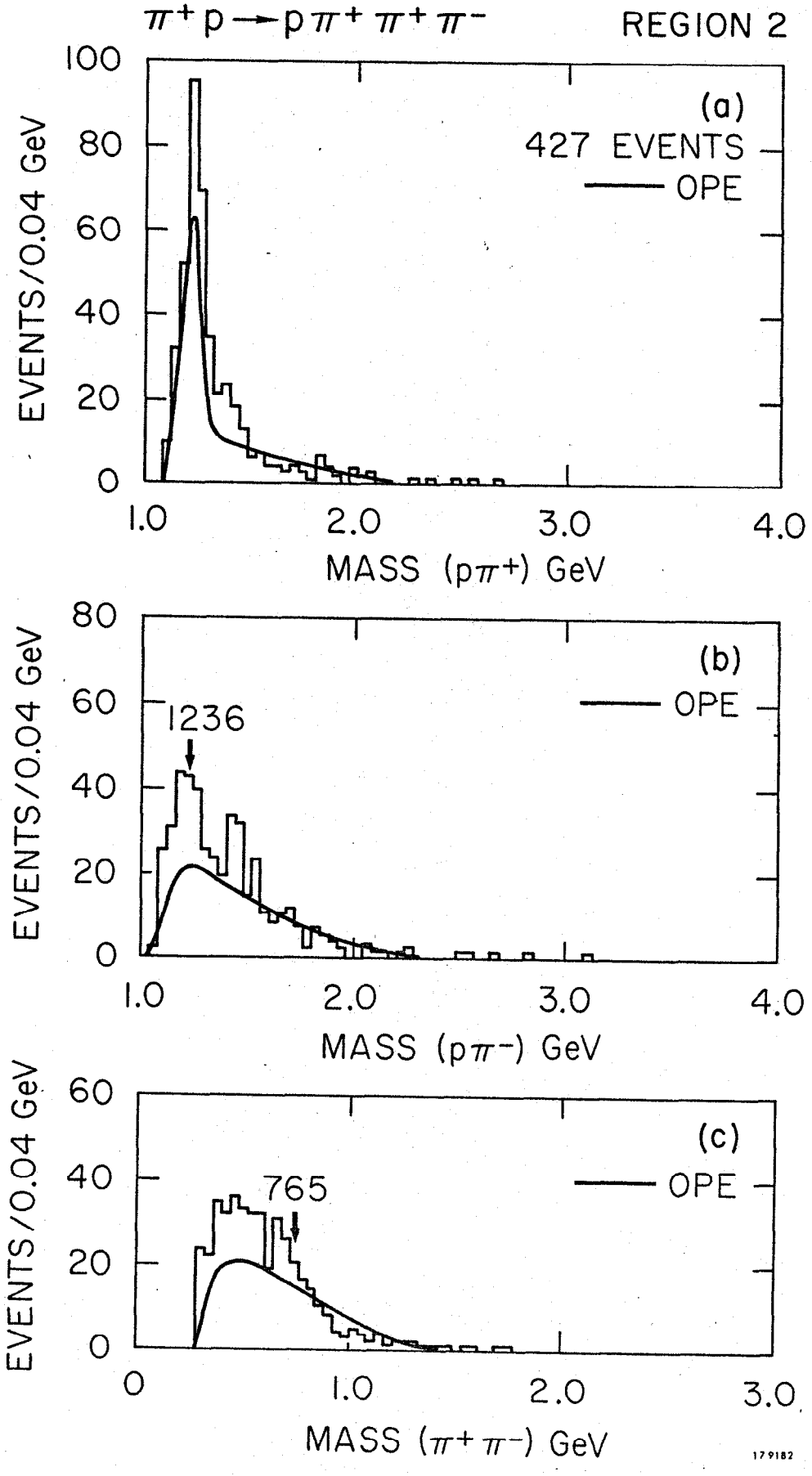
$\pi^+ p \rightarrow p\pi^+\pi^+\pi^-$
REGION 2
(a)
427 EVENTS
OPE
EVENTS/0.04 GeV
MASS $(p\pi^+)$ GeV
(b)
OPE
1236
EVENTS/0.04 GeV
MASS $(p\pi^-)$ GeV
(c)
OPE
765
EVENTS/0.04 GeV
MASS $(\pi^+\pi^-)$ GeV
179182

Fig. 28

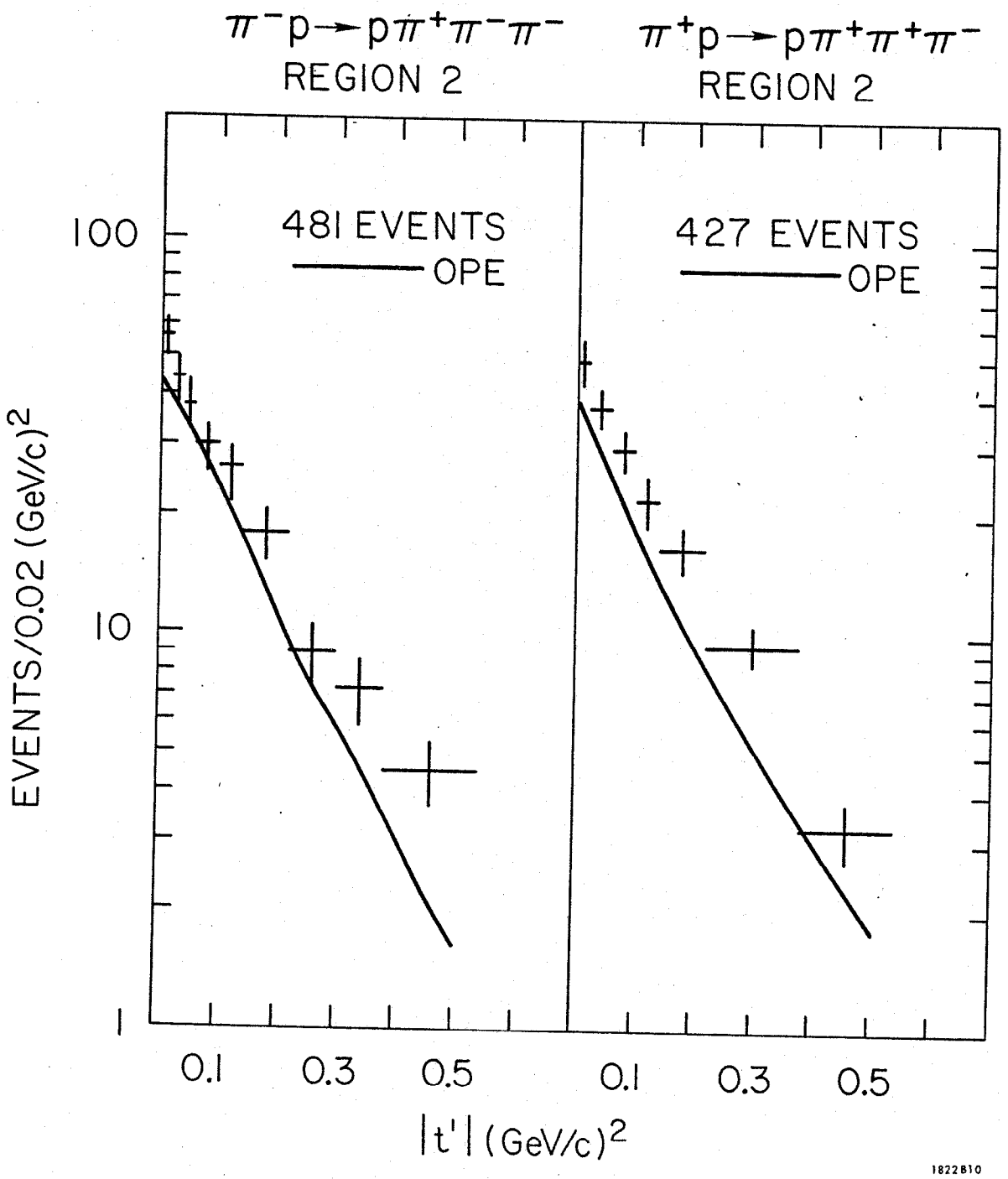
$\pi^- p \to p\pi^+\pi^-\pi^-$
REGION 2
$\pi^+ p \to p\pi^+\pi^+\pi^-$
REGION 2
481 EVENTS
OPE
427 EVENTS
OPE
100
10
1
EVENTS/0.02 (GeV/c)^2
0.1
0.3
0.5
0.1
0.3
0.5
$|t'|$ (GeV/c)^2
1822B10

Fig. 29

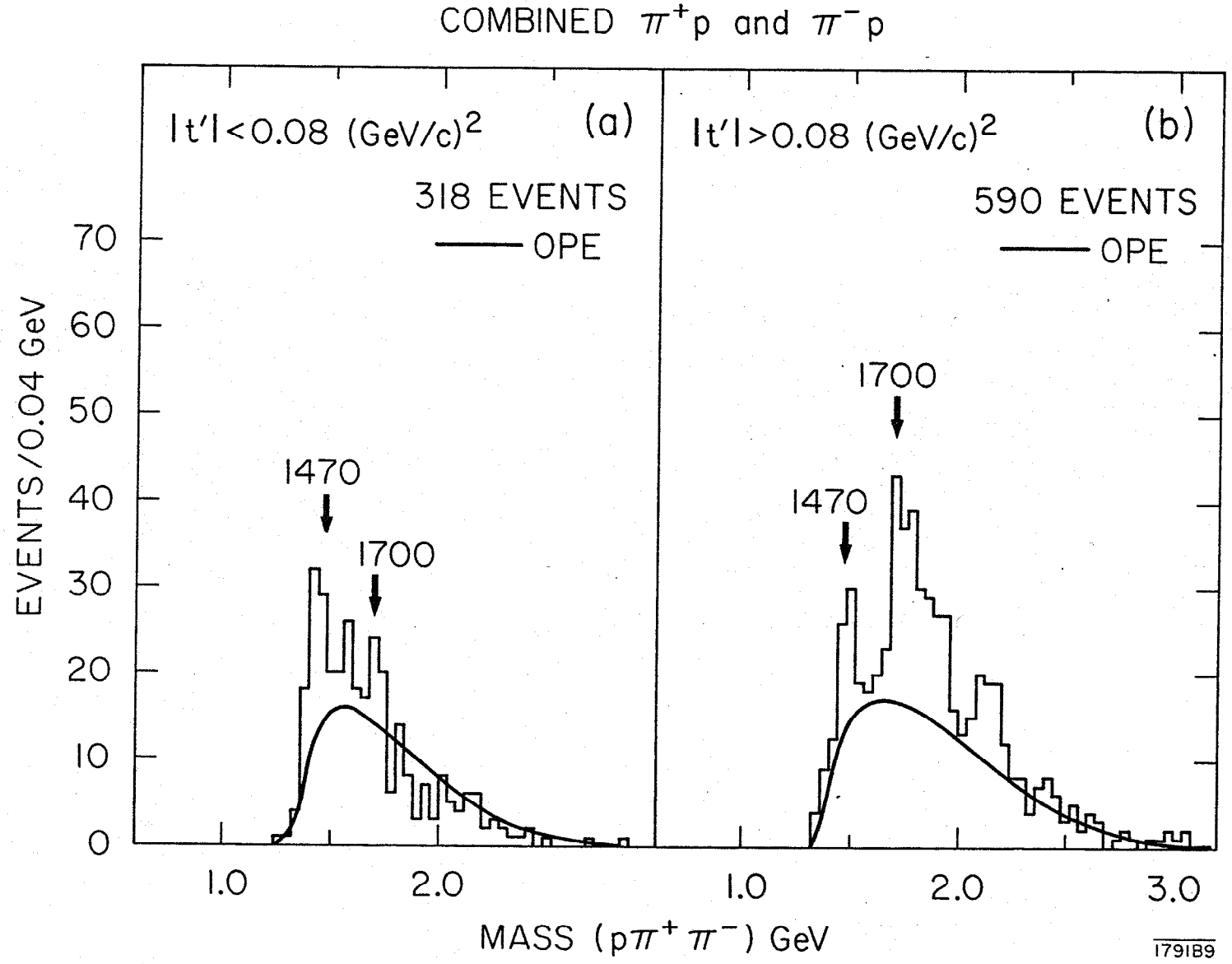
COMBINED π^+p and π^-p
$|t'|<0.08$ (GeV/c)^2
(a)
318 EVENTS
OPE
1470
1700
$|t'|>0.08$ (GeV/c)^2
(b)
590 EVENTS
OPE
1700
1470
EVENTS/0.04 GeV
0
10
20
30
40
50
60
70
1.0
2.0
1.0
2.0
3.0
MASS ($p\pi^+\pi^-$) GeV
179189

Fig. 30

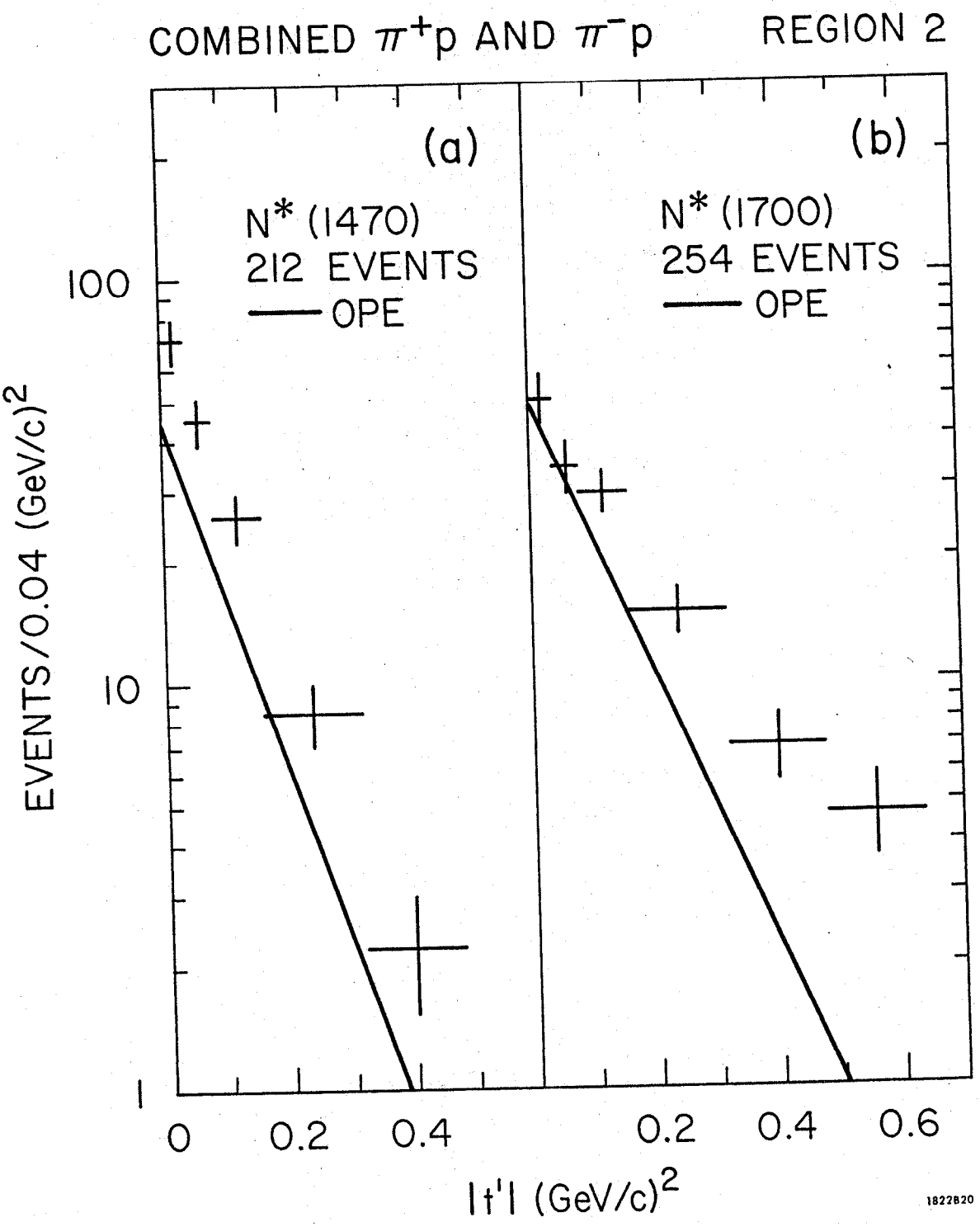
COMBINED π^+p AND π^-p
REGION 2
(a)
N* (1470)
212 EVENTS
OPE
(b)
N* (1700)
254 EVENTS
OPE
100
10
1
EVENTS/0.04 (GeV/c)^2
0
0.2
0.4
0.2
0.4
0.6
$|t'|$ (GeV/c)^2
1822B20

Fig. 31

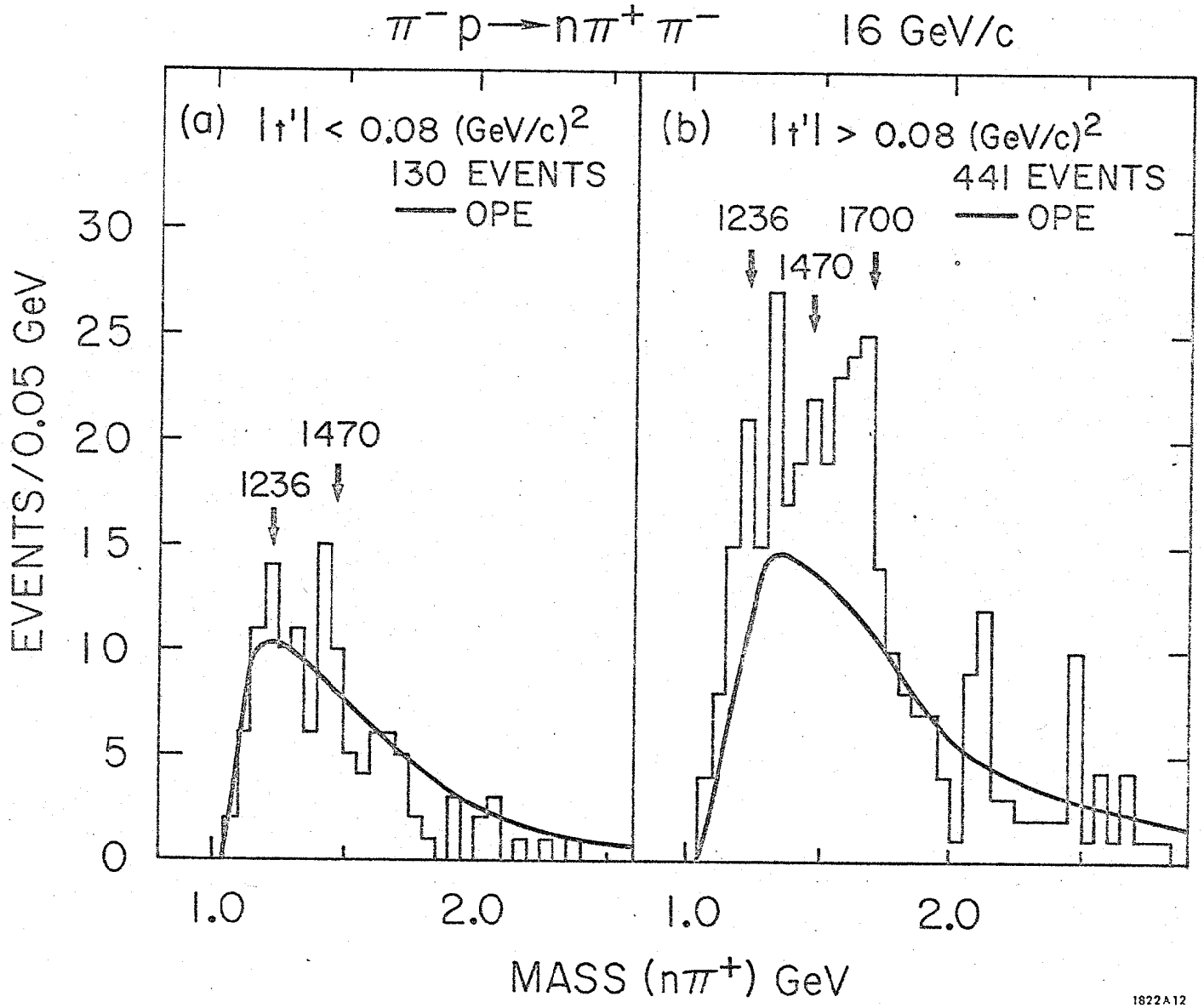
$\pi^- p \rightarrow n\pi^+\pi^-$ 16 GeV/c
(a) $|t'| < 0.08$ (GeV/c)^2
130 EVENTS
OPE
(b) $|t'| > 0.08$ (GeV/c)^2
441 EVENTS
OPE
1236
1470
1700
EVENTS/0.05 GeV
0
5
10
15
20
25
30
1.0
2.0
MASS ($n\pi^+$) GeV
1822A12

Fig. 32

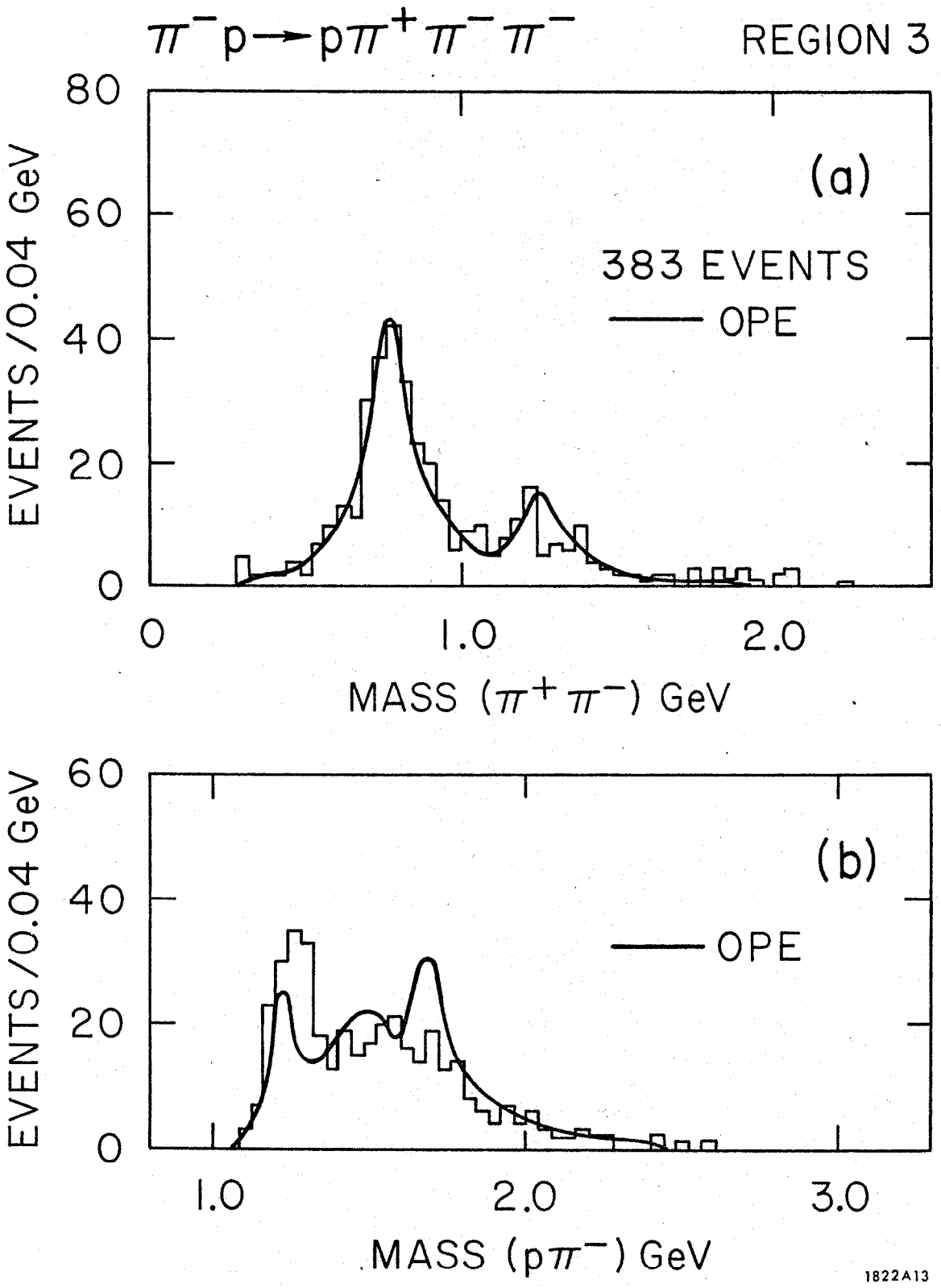
$\pi^- p \rightarrow p\pi^+\pi^-\pi^-$
REGION 3
(a)
383 EVENTS
OPE
EVENTS/0.04 GeV
MASS $(\pi^+\pi^-)$ GeV
(b)
OPE
EVENTS/0.04 GeV
MASS $(p\pi^-)$ GeV
1822A13

Fig. 33

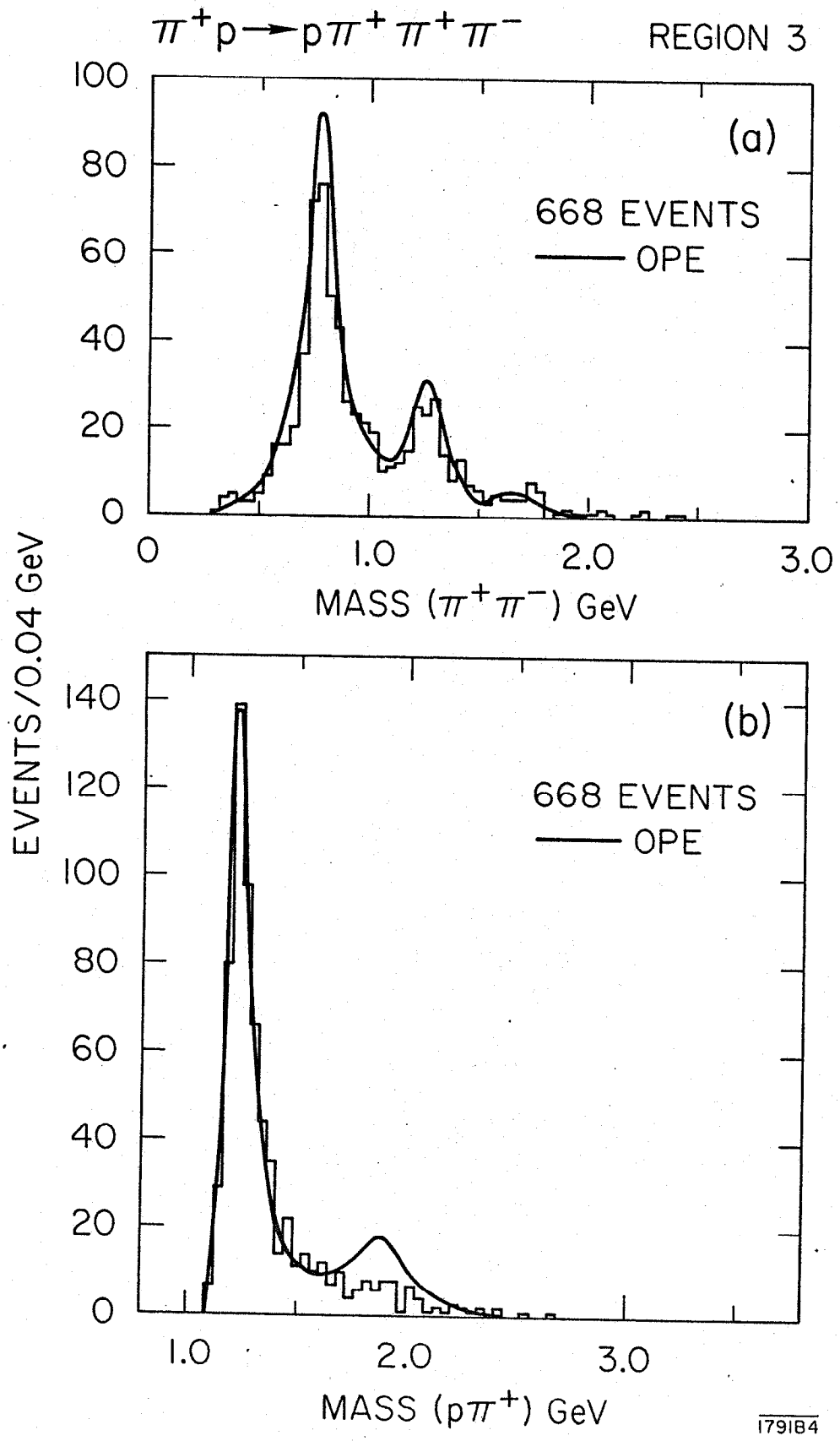
$\pi^+ p \rightarrow p\pi^+\pi^+\pi^-$
REGION 3
(a)
668 EVENTS
OPE
MASS $(\pi^+\pi^-)$ GeV
(b)
668 EVENTS
OPE
EVENTS/0.04 GeV
MASS $(p\pi^+)$ GeV
179184

Fig. 34

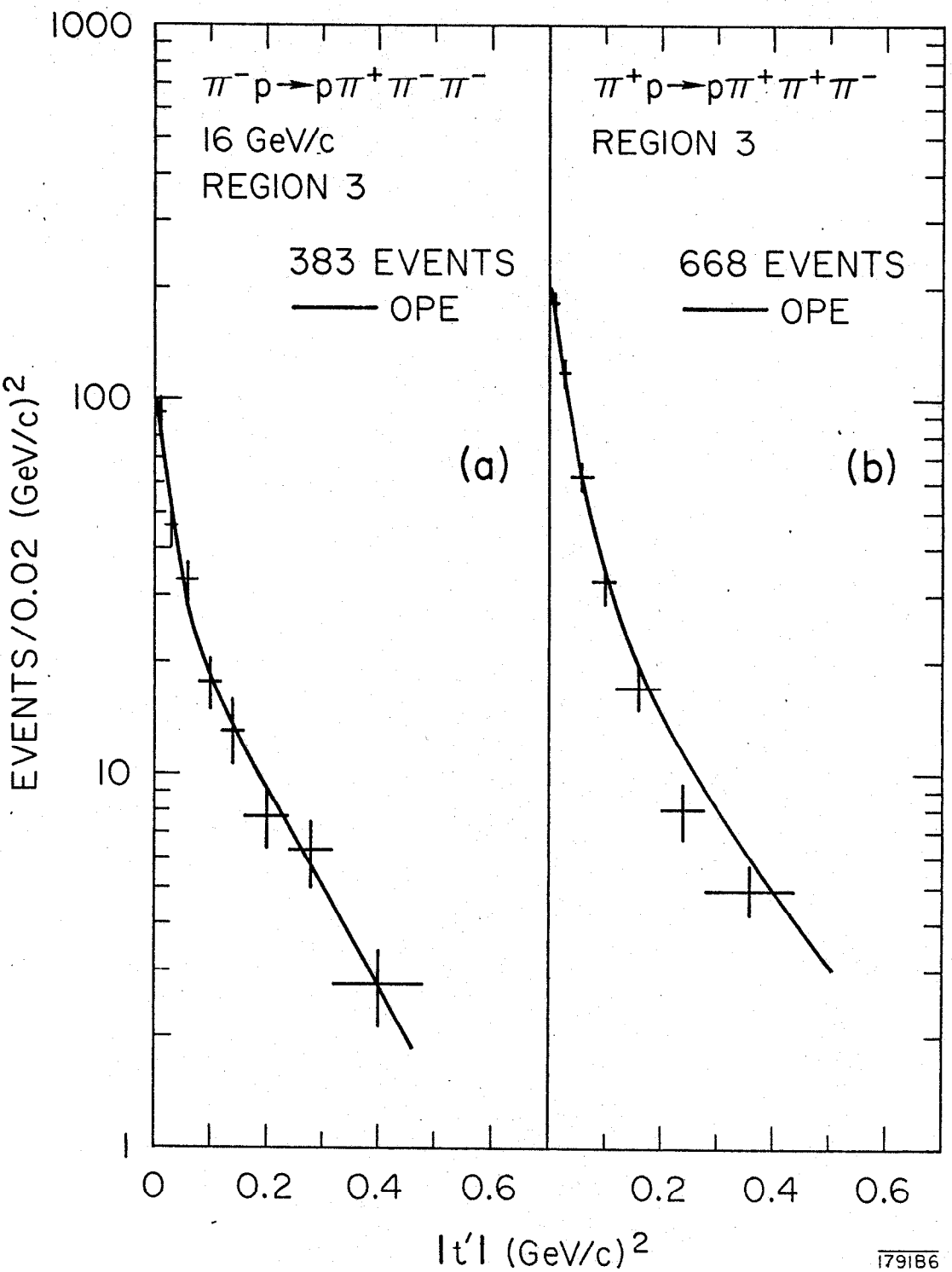
1000
100
10
1
EVENTS/0.02 (GeV/c)²
π⁻p→pπ⁺π⁻π⁻
16 GeV/c
REGION 3
383 EVENTS
OPE
(a)
π⁺p→pπ⁺π⁺π⁻
REGION 3
668 EVENTS
OPE
(b)
0
0.2
0.4
0.6
0.2
0.4
0.6
|t'| (GeV/c)²
179186

Fig. 35

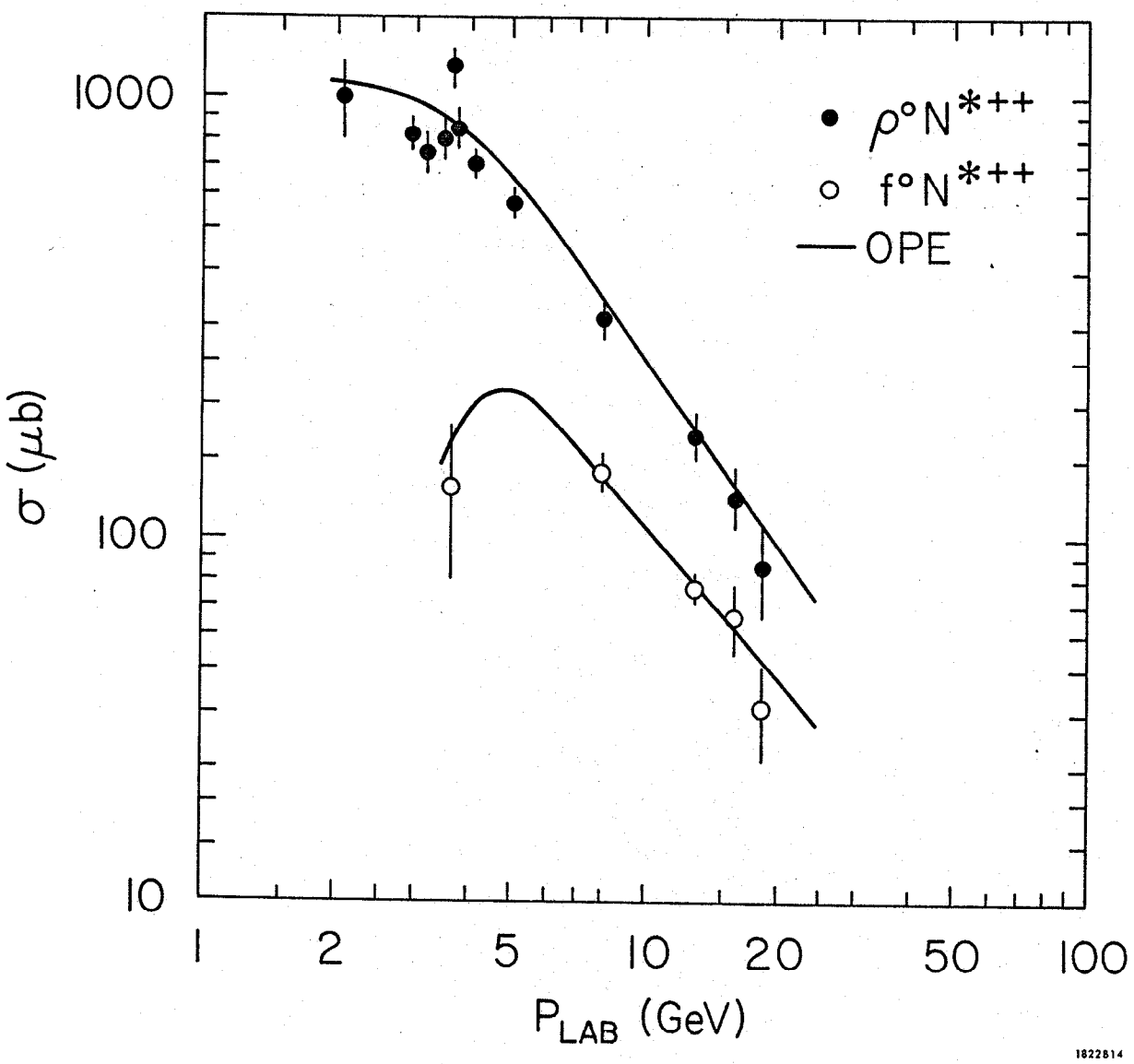

Fig 36

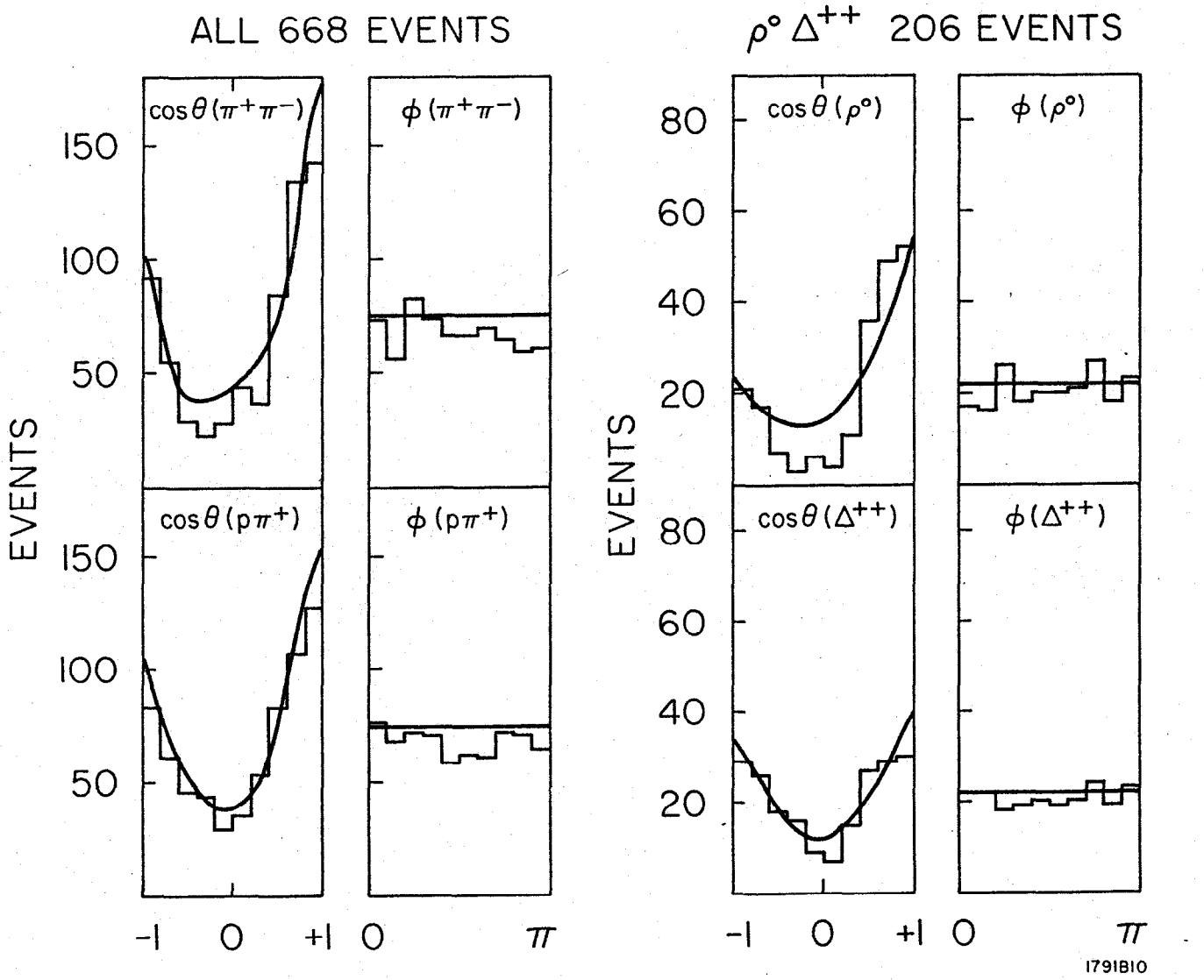
ALL 668 EVENTS
ρ° Δ++ 206 EVENTS
cos θ (π+π−)
φ (π+π−)
cos θ (pπ+)
φ (pπ+)
cos θ (ρ°)
φ (ρ°)
cos θ (Δ++)
φ (Δ++)
EVENTS
150
100
50
80
60
40
20
−1
0
+1
0
π
1791B10

Fig. 37.

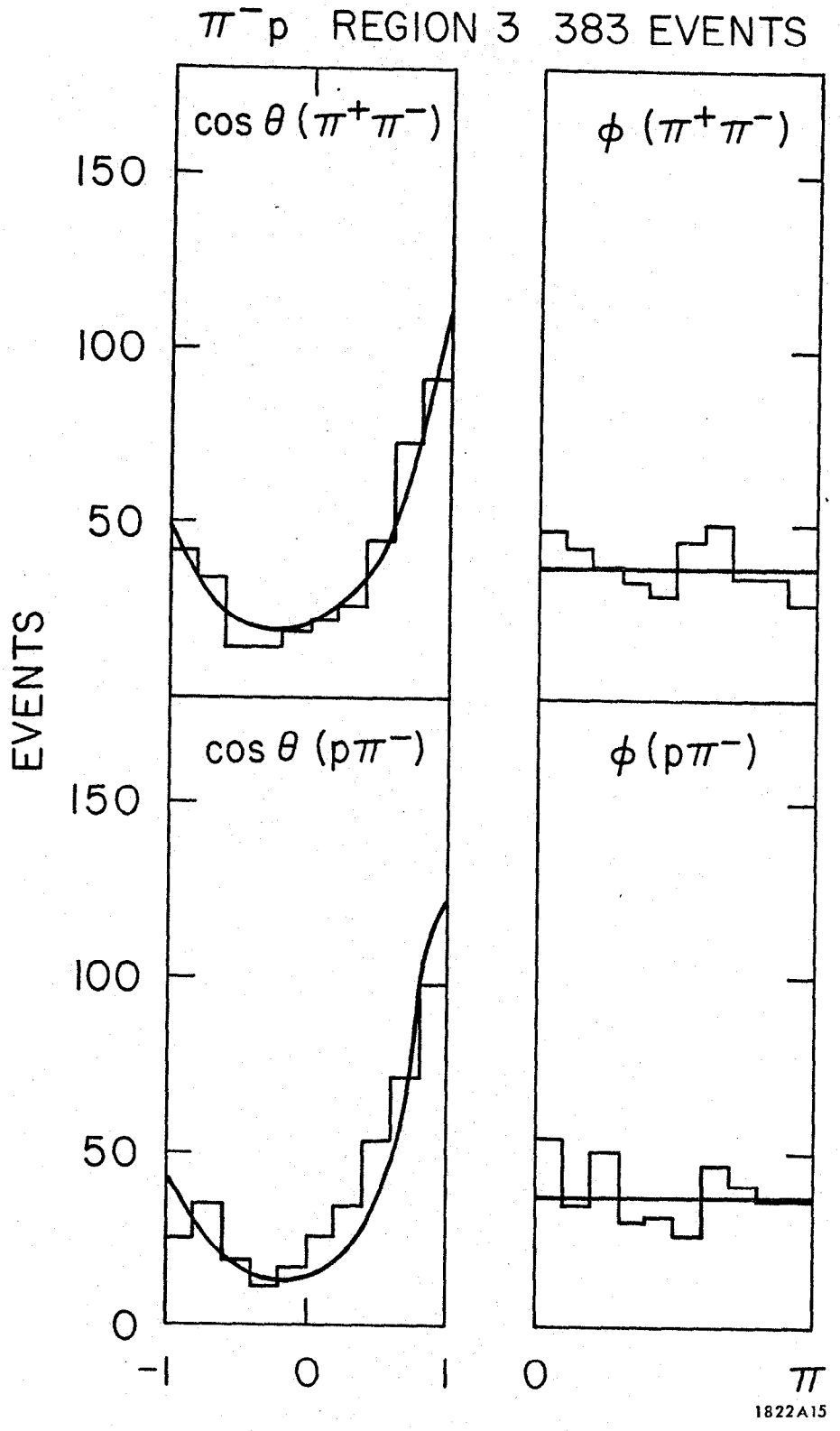
$\pi^- p$ REGION 3 383 EVENTS
$\cos\theta\,(\pi^+\pi^-)$
$\phi\,(\pi^+\pi^-)$
$\cos\theta\,(p\pi^-)$
$\phi\,(p\pi^-)$
EVENTS
150
100
50
0
150
100
50
0
-1
0
1
0
π
1822A15

Fig. 38

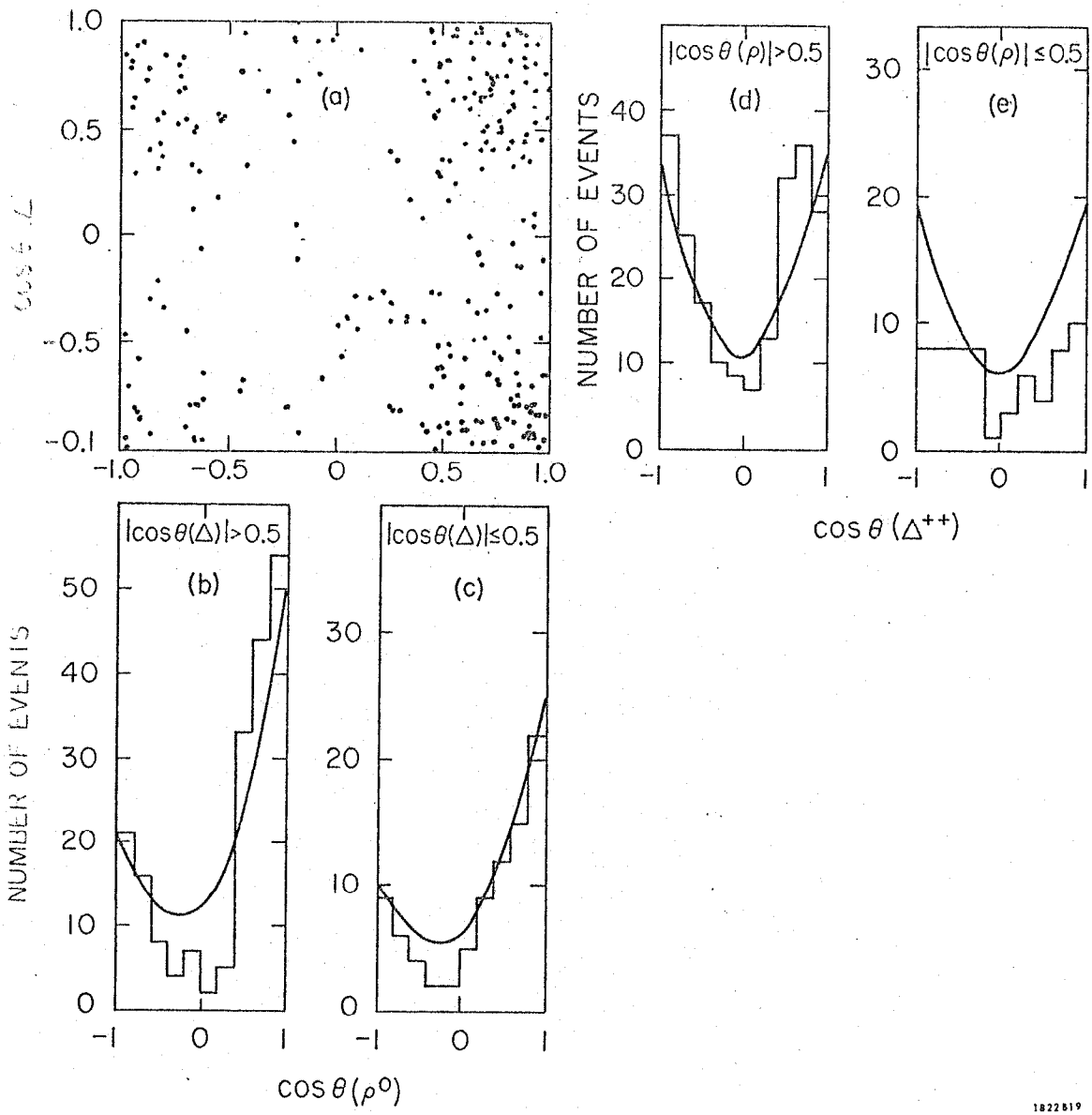
(a)
(b)
(c)
(d)
(e)
|cos θ(Δ)|>0.5
|cos θ(Δ)|≤0.5
|cos θ (ρ)|>0.5
|cos θ(ρ)| ≤0.5
NUMBER OF EVENTS
cos θ (ρ⁰)
cos θ (Δ⁺⁺)
1822819

Fig. 39

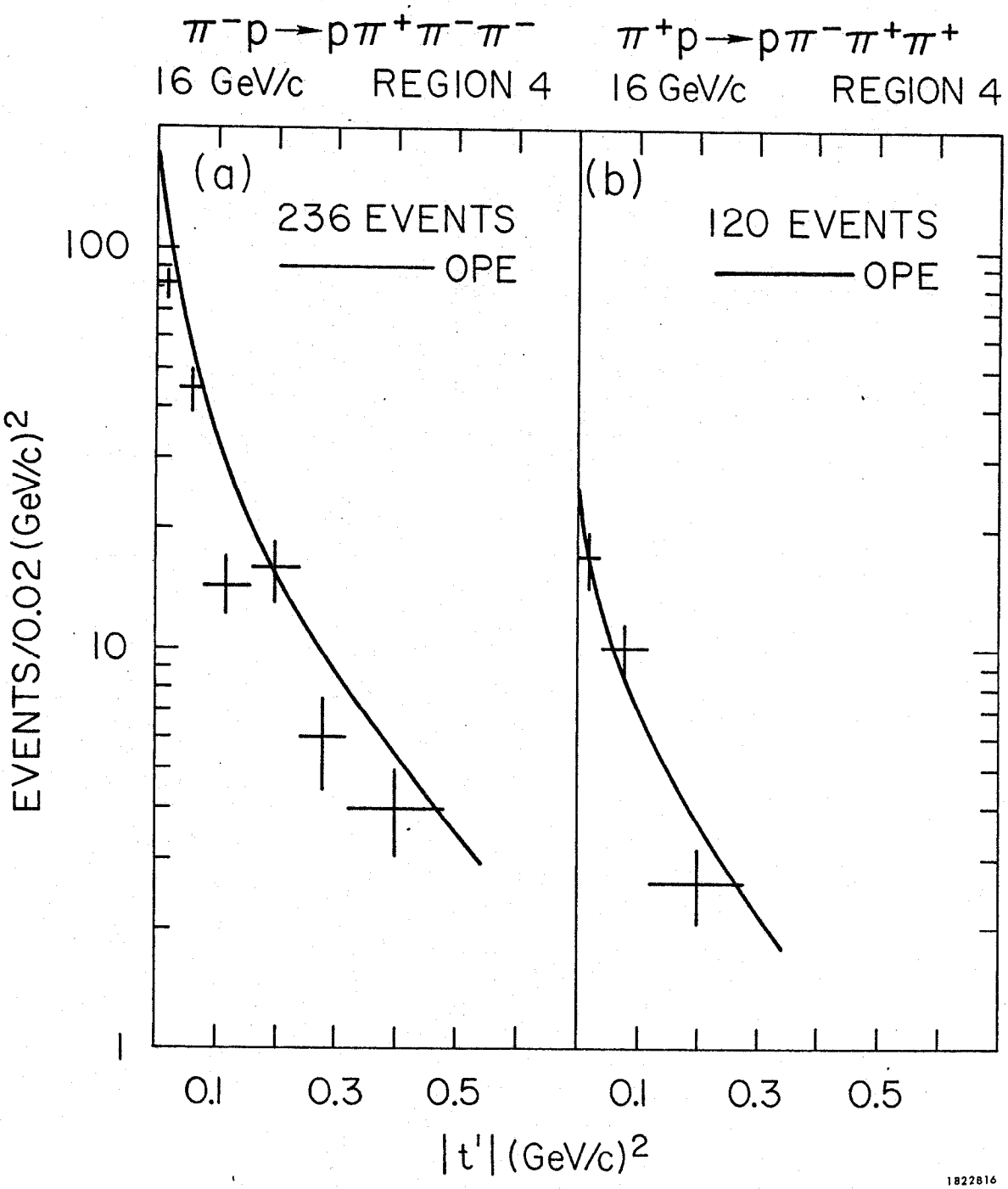
$\pi^- p \to p\pi^+\pi^-\pi^-$
16 GeV/c REGION 4
$\pi^+ p \to p\pi^-\pi^+\pi^+$
16 GeV/c REGION 4
(a)
236 EVENTS
OPE
(b)
120 EVENTS
OPE
100
10
1
EVENTS/0.02 (GeV/c)^2
0.1
0.3
0.5
0.1
0.3
0.5
$|t'|$ (GeV/c)^2
1822816

Fig. 40

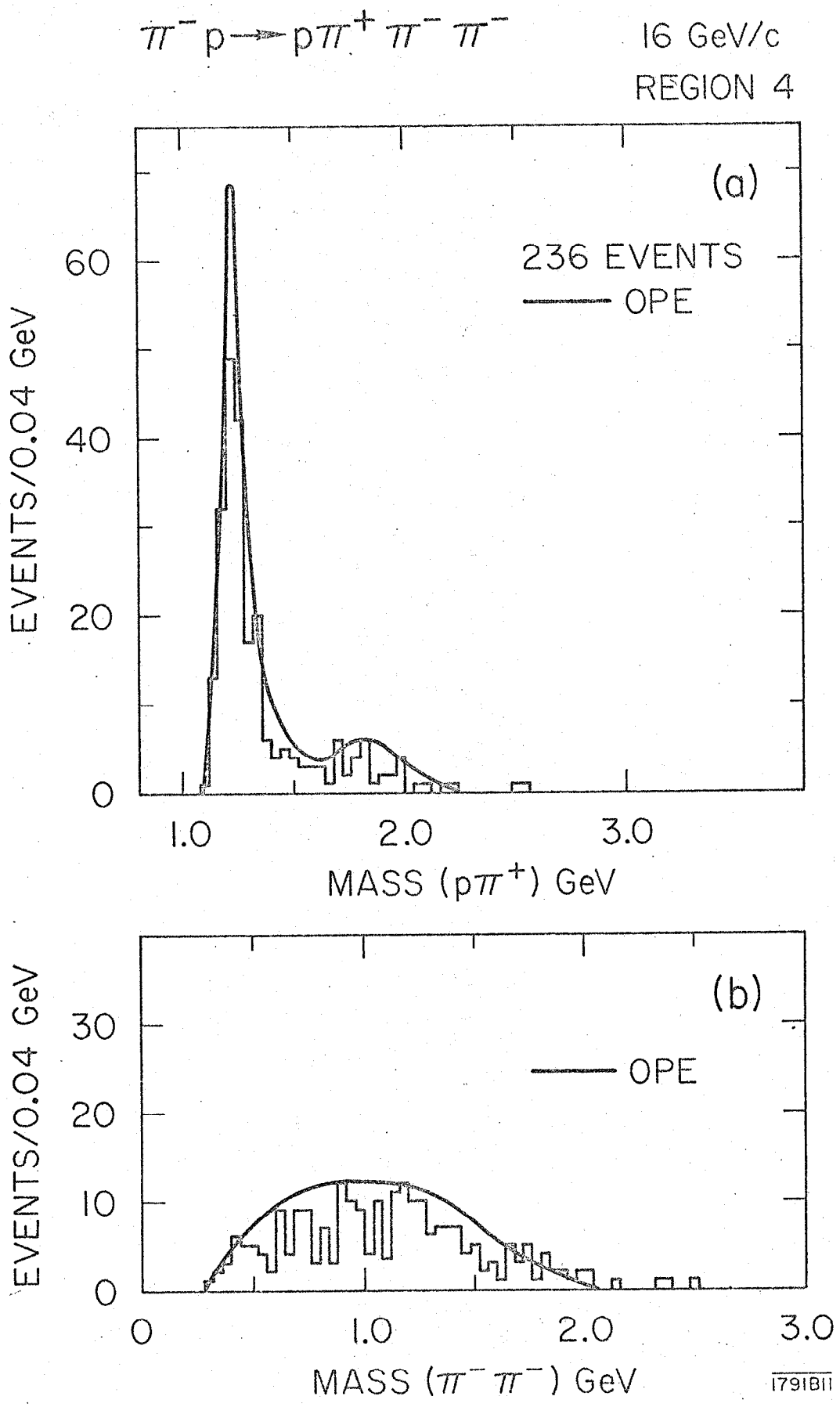
$\pi^- p \rightarrow p\pi^+ \pi^- \pi^-$
16 GeV/c
REGION 4
(a)
236 EVENTS
OPE
EVENTS/0.04 GeV
0
20
40
60
1.0
2.0
3.0
MASS ($p\pi^+$) GeV
(b)
OPE
EVENTS/0.04 GeV
0
10
20
30
0
1.0
2.0
3.0
MASS ($\pi^- \pi^-$) GeV
1791B11

Fig. 41

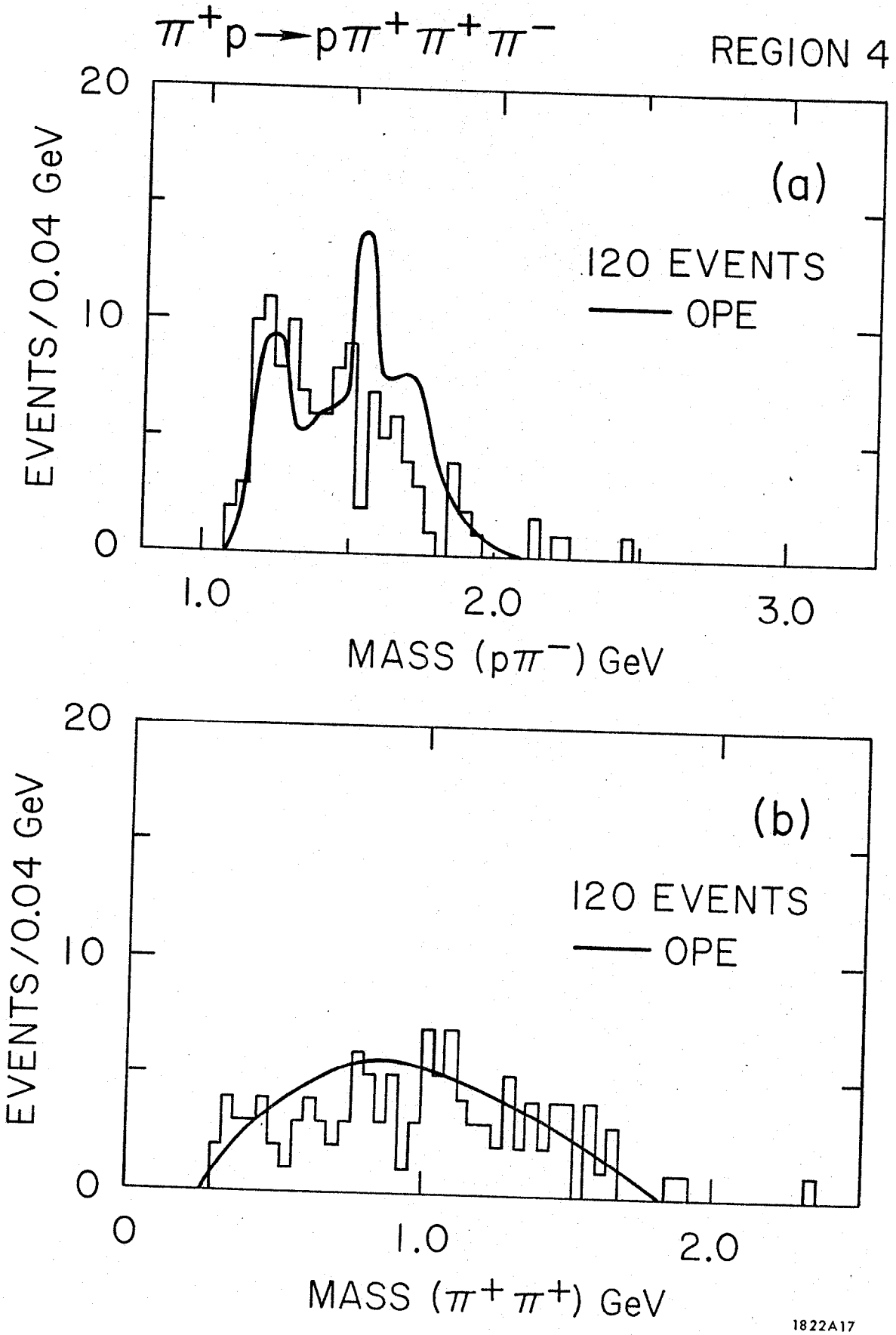
$\pi^+ p \rightarrow p\pi^+\pi^+\pi^-$
REGION 4
(a)
120 EVENTS
OPE
EVENTS/0.04 GeV
MASS ($p\pi^-$) GeV
(b)
120 EVENTS
OPE
EVENTS/0.04 GeV
MASS ($\pi^+\pi^+$) GeV
1822A17

Fig. 42

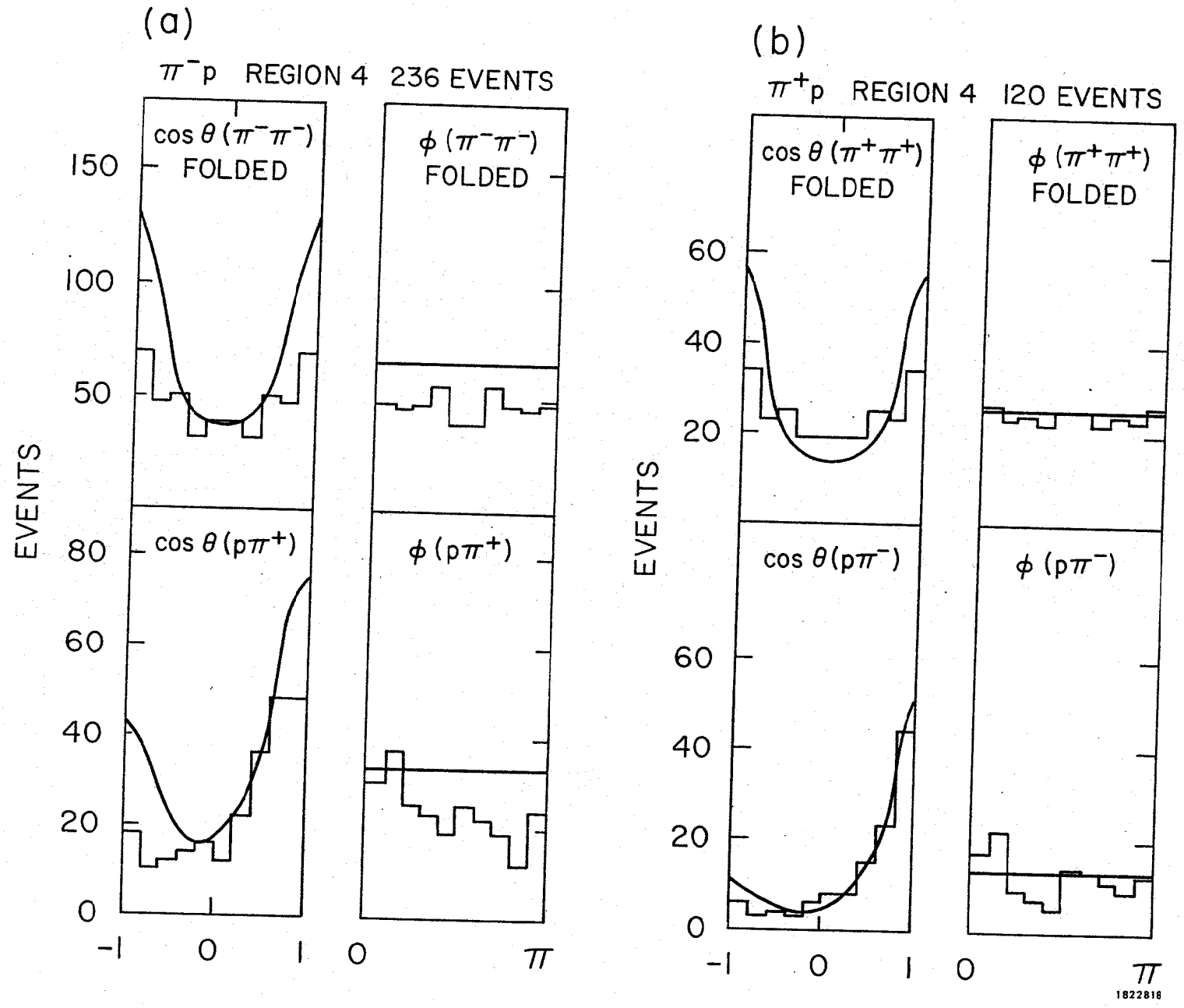
(a)
π^-p REGION 4 236 EVENTS
$\cos\theta(\pi^-\pi^-)$ FOLDED
$\phi(\pi^-\pi^-)$ FOLDED
$\cos\theta(p\pi^+)$
$\phi(p\pi^+)$
EVENTS
150
100
50
80
60
40
20
0
-1
0
1
0
π
(b)
π^+p REGION 4 120 EVENTS
$\cos\theta(\pi^+\pi^+)$ FOLDED
$\phi(\pi^+\pi^+)$ FOLDED
$\cos\theta(p\pi^-)$
$\phi(p\pi^-)$
EVENTS
60
40
20
60
40
20
0
-1
0
1
0
π
1822818

Fig. 43